



Andreas Süß, BSc

**Validation of flank contact patterns predicted by multi-body dynamics simulation of cylindrical gears undergoing spatial angular misalignments**

**MASTERARBEIT**

zur Erlangung des akademischen Grades

Diplom-Ingenieur

Masterstudium Wirtschaftsingenieurwesen-Maschinenbau

eingereicht an der

**Technischen Universität Graz**

Betreuer

Dr.techn. Michael Bader

Institut für Maschinenelemente und Entwicklungsmethodik

## **STATUTORY DECLARATION**

I declare that I have authored this thesis independently, that I have not used other than the declared sources/resources, and that I have explicitly marked all material, which has been quoted either literally or by content from the used sources.

---

Date

---

Signature

## **EIDESSTAATLICHE ERKLÄRUNG**

Ich erkläre an Eides statt, dass ich die vorliegende Arbeit selbstständig verfasst, andere als die angegebenen Quellen/Hilfsmittel nicht benutzt, und die den benutzten Quellen wörtlich und inhaltlich entnommenen Stellen als solche kenntlich gemacht habe. Das in TUGRAZonline hochgeladene Textdokument ist mit der vorliegenden Masterarbeit identisch.

---

Datum

---

Unterschrift

## **Danksagung**

An dieser Stelle möchte ich mich bei Herrn Prof. Dr.techn. Hick für die Ermöglichung der Diplomarbeit sowie bei Herrn Prof. Dr.techn. Bader für die hervorragende Betreuung bedanken.

Mein besonderer Dank ergeht an Dipl.-Ing. Martin Sopouch, der mir die Diplomarbeit anvertraut und mich durchgehend mit seinem umfassenden Fachwissen unterstützt hat. Er nahm sich auch für detailliertere sowie ausführlichere Fragen Zeit.

Meiner Familie möchte ich für die finanzielle sowie mentale Unterstützung danken. Meiner Freundin danke ich für die Unterstützung während der gesamten Studienzeit.

Des Weiteren möchte ich meinem Studienkollegen Daniel Kriegl für die Möglichkeit des gemeinsamen Lernens für diverse Prüfungen während der Studienzeit danken. Sarah Zettl war sowohl beim gemeinsamen Lernen als auch bei organisatorischen Dingen eine große Stütze, wofür ich ihr recht herzlich danke.

## **Kurzfassung**

Ziel dieser Arbeit ist die Evaluierung des Kontakttragbildes von Stirnzahnrädern, welches numerisch mit dem Mehrkörperdynamik-Programm AVL EXCITE simuliert wird. Die Gültigkeit des aktuell implementierten Kontaktmodells, sowie die Ansätze zur Erfassung der relevanten Verformungen im Zahnkontakt, am Zahn (Biegung) und dem Radkörper sind mittels Vergleich zum Stand der Technik abzusichern.

Die Validierung wird quantitativ durchgeführt. Die Beurteilung der berechneten Tragbilder und der Breitenlastverteilung erfolgt anhand etablierter Kontaktanalyse-Programme. Basierend auf den Ergebnissen dieser Evaluierung werden Verbesserungsvorschläge hinsichtlich des Kontaktmodells und der Deformationsansätze erarbeitet.

## **Abstract**

The aim of this work is the evaluation of the contact pattern of cylindrical gears, which is numerically simulated using the multi-body dynamics software AVL EXCITE. The validity of the currently implemented contact model, as well as the approaches for resolving the relevant deformations in the tooth contact, of the tooth (bending) and the wheel body are to be ensured by comparison with the state of the art.

The validation is accomplished quantitatively. The assessment of the calculated gear contact patterns and the face load distribution is performed by using established tooth contact analysis tools. Based on the results of this evaluation, suggestions for potential improvements of the contact model and the deformation approaches are proposed.

.

# Contents

<b>1. Introduction .....</b>	<b>1</b>
<b>2. Multi-body dynamics software AVL EXCITE Power Unit .....</b>	<b>4</b>
2.1 Bodies and Joints .....	4
2.2 Cylindrical gear mesh joints in EXCITE.....	5
<b>3. The Advanced Cylindrical Gear Joint.....</b>	<b>6</b>
3.1 Joint capabilities and restrictions .....	8
3.2 Discretization.....	9
3.3 Detection of contact .....	10
3.4 Constitution of the deformation field .....	12
3.5 Theoretical pressure distribution at the tooth contact .....	13
3.6 Contact Force Calculation.....	14
3.6.1 Flank contact penetration.....	14
3.6.2 Bending of the Teeth .....	16
3.6.3 Deformation of the wheel body.....	17
<b>4. Current status of established contact simulation tools.....</b>	<b>18</b>
4.1 LVR.....	19
4.2 RIKOR.....	20
4.3 STIRAK.....	21
4.4 Romax.....	21
<b>5. KISSsoft .....</b>	<b>21</b>
5.1 Cylindrical Gears .....	22
5.1.1 Contact analysis .....	23
5.1.2 Meshing stiffness .....	23
5.1.3 Discretization .....	24
5.2 Consideration of dynamic effects in KISSsoft.....	25
5.3 Empirical factors .....	25
5.3.1 Slice coupling factor.....	26

5.3.2	Border weakening factor .....	27
5.3.3	Stiffness correction factor .....	28
<b>6.</b>	<b><i>Gear mesh misalignments and possibilities of their compensation.....</i></b>	<b>30</b>
<b>6.1</b>	<b>Flank surface deviations.....</b>	<b>33</b>
<b>6.2</b>	<b>Run-out error.....</b>	<b>34</b>
<b>6.3</b>	<b>Pitch deviation.....</b>	<b>34</b>
<b>6.4</b>	<b>Total radial composite deviation .....</b>	<b>34</b>
<b>6.5</b>	<b>Parallel misalignment .....</b>	<b>35</b>
<b>6.6</b>	<b>Skew misalignment.....</b>	<b>36</b>
<b>6.7</b>	<b>Slope misalignment .....</b>	<b>38</b>
<b>6.8</b>	<b>Compensation of Gear Mesh Misalignments.....</b>	<b>39</b>
6.8.1	Profile modifications.....	40
6.8.2	Lead corrections.....	43
<b>7.</b>	<b><i>Qualitative Validation .....</i></b>	<b>45</b>
<b>7.1</b>	<b>Simplified EXCITE model.....</b>	<b>47</b>
7.1.1	Gear data of the simplified EXCITE model .....	49
7.1.2	Global coordinate system .....	51
<b>7.2</b>	<b>KISSsoft model.....</b>	<b>51</b>
<b>7.3</b>	<b>Compared quantities and expected result values.....</b>	<b>52</b>
<b>7.4</b>	<b>Influence of the inertia tensor of the body.....</b>	<b>56</b>
<b>7.5</b>	<b>Description of the Investigated models.....</b>	<b>57</b>
<b>7.6</b>	<b>Results .....</b>	<b>59</b>
7.6.1	Model A.....	59
7.6.2	Model B.....	61
7.6.3	Model C.....	63
7.6.4	Model D.....	65
7.6.5	Model E .....	67
7.6.6	Model F .....	69
7.6.7	Model G .....	71
7.6.8	Model H.....	73
7.6.9	Model I .....	76

7.6.10	Model J .....	79
<b>7.7</b>	<b>Influence of the elastic mesh deformation on the path of contact and the contact ratio</b>	<b>81</b>
<b>7.8</b>	<b>Evaluation of the Petersen modified Hertz contact approach .....</b>	<b>86</b>
7.8.1	Simplified model .....	86
7.8.2	Model with a increases curvature of the involute .....	87
7.8.3	Model with a decreased curvature of the involute .....	89
<b>8.</b>	<b><i>Summary and outlook</i></b> .....	<b>90</b>
<b>8.1</b>	<b>Geometrical verification</b> .....	<b>91</b>
8.1.1	Geometrical verification of the slice equivalent deformation by mean of CAD software .	92
8.1.2	Geometrical verification of the slice contact points .....	95
<b>8.2</b>	<b>Development of an algorithm to correct the position of the contact points with respect to slope misalignment</b> .....	<b>96</b>
8.2.1	Validation of the modified ACYG code.....	98
<b>8.3</b>	<b>Proposal of possible enhancements of the ACYG joint</b> .....	<b>106</b>
8.3.1	Modifying the existent ACYG source code.....	106
8.3.2	The use of empirical factors.....	107
8.3.3	Alternative ways to compute the meshing stiffness.....	108
8.3.4	Automated modification of the micro geometry.....	111
<b>8.4</b>	<b>Conclusion</b> .....	<b>112</b>
<b>9.</b>	<b><i>LIST OF FIGURES</i></b> .....	<b>114</b>
<b>10.</b>	<b><i>LIST OF EQUATIONS</i></b> .....	<b>118</b>
<b>11.</b>	<b><i>LIST OF REFERENCES</i></b> .....	<b>119</b>

## 1. Introduction

Design and optimization of the load distribution in gear meshes have become an integral part of the gearbox development process in the automotive as well as in the industrial field of applications. In particular, angular misalignments of the mating gears wheels may give rise to durability, noise and vibration concerns. Hence, a reliable predictive method for the simulation of gear contact patterns is of paramount importance.

Nowadays in the early design stage simulative tooth contact analysis (TCA) is conducted to ensure a gear contact pattern with a well balanced load distribution over the width of the gear. TCA tools, which typically operate on a quasi-static solution-level, require shaft deflections and angular misalignments of the mating gears as input. In the early design stage these inputs are usually based on estimations or experience from similar designs or are obtained from static-system calculations where the shaft system including the bearing/support situation is resolved in a simply way.

Recently multi-body dynamic (MBD) simulation is also applied in close conjunction with tooth contact analysis. Many of the specific and generic MDB-tools utilize a gear contact approach, which is directly coupled with the time integration loop. The advantage of this approach is that dynamic effects of the shaft/bearing/housing system can be resolved in very high detail and resulting angular misalignments of the gear wheels can serve as motion-input for the gear contact model. Moreover, the consideration of flexible structures enables the computation of structure born noise behaviour and by that, the assessment of the acoustic behaviour of the gear meshes.

It is clear that tooth contact approaches utilized by MBD-Tools cannot operate on the same level of fidelity as this is the case with specialized, static TCA-tools. In order to obtain industrial-compatible simulation times gear contact models coupled to MBD are forced to apply certain simplifications. However, despite the obvious differences an acceptable agreement regarding the resolution of angular misalignments with respect to the contact pattern is necessary.

In the past, investigation of miscellaneous models have led to the suspicion that the simulation of cylindrical gears in the multi-body dynamics software AVL EXCITE is overcompensating spatial angular misalignments. This results in an unrealistic force distribution over the contact pattern. This contact pattern is used by gear manufactures and used to predict the behaviour of the gearing. Especially, noise and transmission errors, which become increasingly important, are affected by a non-uniform force distribution on the contact pattern. For this reason this master thesis shall evaluate the prediction of flank contact patterns computed by the multi-body dynamics simulation tool AVL EXCITE Power Unit [1] while undergoing spatial angular misalignments. This evaluation is based on a comparison with the contact analysis software KISSsoft. It is chosen because it is distinguished in the industry, well experimentally validated and moreover applied approaches are well documented.

This master thesis is divided into the following chapters:

In chapter two, an introduction into the multi-body dynamics software AVL EXCITE Power Unit and an insight into the available possibilities to simulate a gear mesh are given.

Chapter three shows in detail the possibilities and limitations of the evaluated gear contact model. Furthermore, the used deformation approaches brought closer.

Chapter four deals with tooth contact simulation tools available and established in the market and distinguishes the implemented possibilities and restrictions.

The contact simulation tool KISSsoft [2] is discussed in chapter five. The chapter addresses the contact analysis, the contact stiffness approaches and the discretization method implemented in KISSsoft. Further, the consideration of dynamic effects and available empirical factors are outlined.

Gear misalignments and their impact on the contact pattern are investigated in chapter six. The possibilities of their compensation are examined.

In chapter seven the qualitative evaluation between EXCITE Power Unit and KISSsoft is made. Further, the used model is introduced.

Based on the results of chapter seven, in chapter eight a geometrical verification of significant quantities is done by comparison with CAD. Furthermore, an algorithm is deduced on the basis of possible angular deviations which is implemented in the current flank contact evaluation code.

## **2. Multi-body dynamics software AVL EXCITE Power Unit**

The software AVL EXCITE enables the simulation of rigid and flexible multi-body dynamics of power trains. It consists of the following simulation tools: EXCITE Power Unit, EXCITE Acoustics, EXCITE Piston and Rings, EXCITE Timing Drive and EXCITE Designer.

The tool EXCITE Power Unit (in the following abbreviated with EXCITE) is capable of design, analysis and optimization of combustion engines, transmissions and power trains. It offers a multi level approach to provide an adjustable modeling depth to fit the application target. The simulation concept of EXCITE is to divide the non-linear mechanical system into subsystems with linear elastic behaviour (called bodies, e.g. the engine block). Therefore, the non-linearities only occur in the connections between the subsystems (called joints, e.g. the contact in gear meshes or the oil film in the slider bearings). To manage these non-linearities, the calculation is performed in time domain.

Typical applications are dynamics of the crank train and engine components, vibration and acoustics (structure borne noise) of entire power units, detailed 3D piston dynamics or detailed bearing analysis. Recently the field of applications has been successfully extended towards automotive and industrial transmission and driveline systems. (See [3])

### **2.1 Bodies and Joints**

Within EXCITE the type of the bodies can be defined as rigid or flexible. Irrespective of the type, physical properties, such as the mass or the inertial tensor can be assigned. If the type is rigid, deformations of the body and thus also the motions of the points (nodes) relative to each other are disabled. Flexible bodies, which represent the gear wheel or the entire transmission shaft, use reduced structure matrices of FE models [4]. The data transfer from the different FE-Solvers to EXCITE is conducted through interfaces. The force-coupling between bodies and hence the simulation of physical effects is realized with connections called joints. Depending on the type of the joint, a multiple or single node coupling to bodies is possible. (See[3])

## 2.2 Cylindrical gear mesh joints in EXCITE

In EXCITE gear meshes can be represented by different levels of model fidelity: Standard gear joint (abbr. GEAR), generic gear joint (abbr. GGEA), and advanced cylindrical Gear Joint (abbr. ACYG). The GEAR and GGEA joints use an engagement line model (figure 1) and either constant or precalculated variable meshing stiffness and damping. The radial and axial movement of the connected nodes is considered but angular deflections about the tilting axis are not taken into consideration.

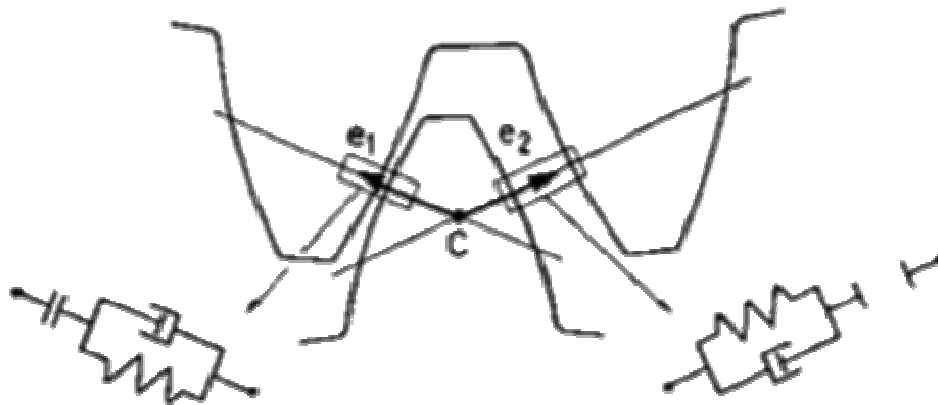


Figure 1: Engagement line model (GEAR/GGEA) (source:[5], chapter 4.16.2.4.)

In addition to the characteristics of the GEAR joint, the GGEA joint supports an epicyclic motion, which enables the computation of planetary gear sets. Furthermore, it accounts for load-dependent contact stiffness. But just like the GEAR joint, the GGEA joint does not support any detailed gear mesh contact based on real flank geometry.

Since the focus on noise and vibrations of the gear box has increased and the currently implemented joints could not reflect these effects, it was necessary to develop a more detailed gear contact representation: the ACYG joint. This joint is based on the tooth law, on real contact surfaces and on the flexibility of the teeth. Since the ACYG joint is the most advanced joint in EXCITE for cylindrical gears, it is used to carry out the evaluation in this thesis. (See [5], chapter 4.16.)

### 3. The Advanced Cylindrical Gear Joint

The basic requirement of a tooth contact model is the linking between the load-deformation-relation of the engagement with the contact line deviations arising from gear mesh misalignments. (see [6], page 644)

The advanced cylindrical gear joint provides a detailed modeling level for cylindrical gears with nominal parallel axis. The cylindrical gears are represented by two bodies, which are connected by the joint. The body connected with the first anchor is referred to as 'Pinion' while the second one is referred to as 'Gear'. Typically the gear wheel with the lower number of teeth is assigned as the pinion but in general there is no restriction which gear wheel is connected as 'Pinion' or 'Gear'. The figure 2 shows the two bodies and the ACYG-joint as they are graphically represented in EXCITE's Block Model Editor.



Figure 2: 2D representation of the ACYG joint and the connected bodies in EXCITE (source [5], chapter 4.17.1)

By reason that the nodes of the bodies can move during the simulation, a local joint coordinate system (JCS) is introduced. Moreover, the whole contact resolution and force calculation is based on the joint coordinate system. The axes of the coordinate system are arranged as shown in

figure 3.

The origin matches with the reference node at the 'Pinion', which is an averaged node of all connected nodes at the pinion. The first axis ( $=X_{JCS}$ ) is pointing from the origin to the reference node of the gear wheel. The third axis ( $=Z_{JCS}$ ) is the rotation axis of the pinion and derived from the average axial position of the 'Pinion'-connected nodes. The second axis ( $=Y_{JCS}$ ) is set by assuming a right handed coordinate system. As a result, the gear base system follows the movement of the connected nodes and ensures that the X-axis of the coordinate system goes through the center of the gears. (See [5], chapter 4.17.1)

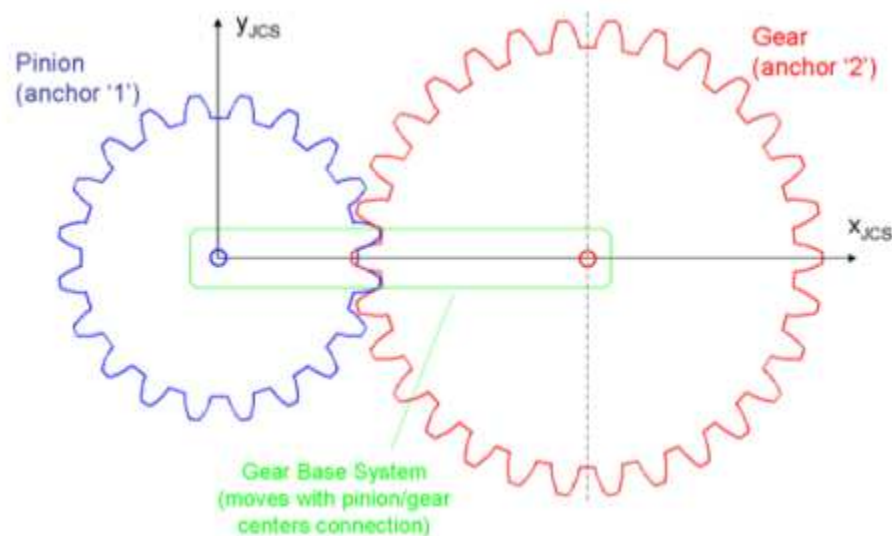


Figure 3: The joint coordinate system of the ACYG joint (source: [5], chapter 4.17.1)

### **3.1 Joint capabilities and restrictions**

The ACYG joint delivers a full contact model embedded in the multi-body dynamics time integration loop while it incorporates detailed flank surface shapes and strenuous multi flank pair contact.

In the following the characteristics of the ACYG joint are enumerated (see [5]):

- Shape modifications and corrections of the flank surfaces are supported.
- Run-out, pitch and profile errors are considered.
- Spatial angular misalignments of the axis are supported.
- The friction and damping calculation is modeled by analytical Elasto-Hydrodynamic-Lubrication (EHL).
- The contact pressure and the root bending stress according ISO 6336 can be calculated.

Since the ACYG joint is tailored for performance the following restrictions have to be considered (see [5]):

- The contact model is restricted to flank interactions taking place in the gear mesh's plane of action.
- Tooth deflections (bending and tilting) as well as flank contact are realized through analytical approaches.

### 3.2 Discretization

To resolve the contact over the gear face width a discretization into a series of slices is used. The higher the number of slices, the higher the resolution, but at the same time the calculation time increases. Each slice has its own internal node placed at the mid of the slice, through which it is linked to its corresponding connection node. The user's input number of slices per connection node multiplied by the number of connection nodes of the joint equals the total number of slices. (As shown in figure 4.) The slice width and position is computed depending on the number and position of the connected nodes, while the width of the slices belonging to one connection node is always constant.

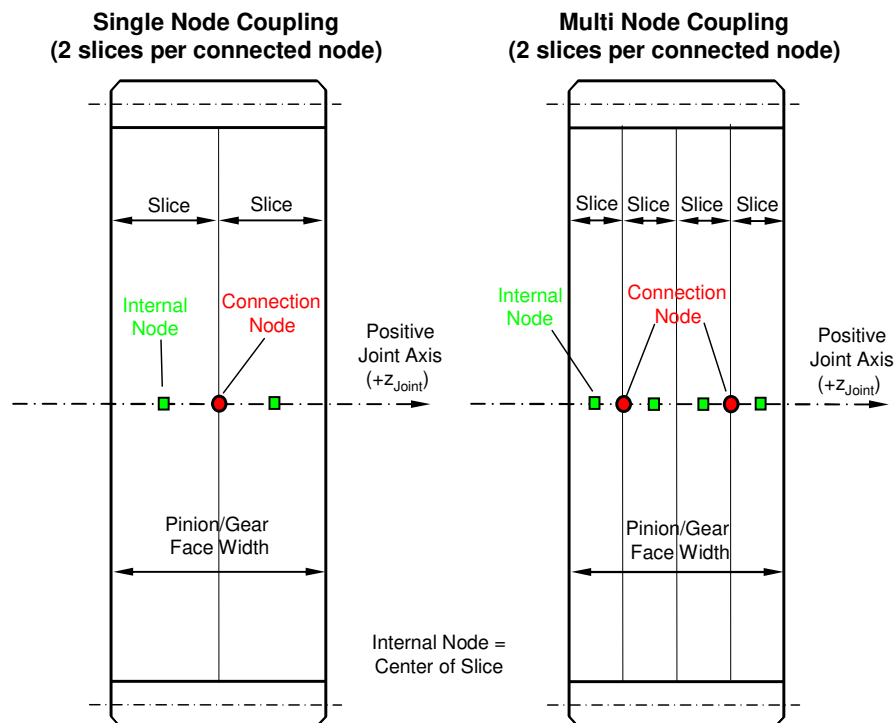


Figure 4: The discretization into slices of the ACYG joint (source:[3], chapter 2.2.5.3.)

The motion information of the internal nodes (position and velocities) is derived from the connection nodes by interpolation. Afterwards the computation of the contact as well as of the forces is performed for the internal nodes only. These forces and moments are then recalculated by means of a distribution algorithm throughout the connection nodes.

Since the slices are not coupled with their adjacent slices, there is no direct mutual support effect between them. That means that less loaded slices won't support higher loaded slices. However, they are coupled over the connection nodes of the bodies representing pinion/gear and therefore the relative displacement of the connection nodes affects the forces and moments of the slices. But this effect is limited to the number of connection nodes and flexible bodies have to be used to enable a relative movement between the nodes. (See [5])

### 3.3 Detection of contact

For the ideally shaped involute the contact occurs only in the plane of action. This is not the case for modified tooth shapes, for example. In order to improve the performance, the contact is firstly evaluated based on the assumption of pure involute flank geometry and their intersection with the plane of action. Secondly, when the nominal contact points and flank surface overlap have been determined, modifications and corrections are accumulated to the ideal penetration distance.

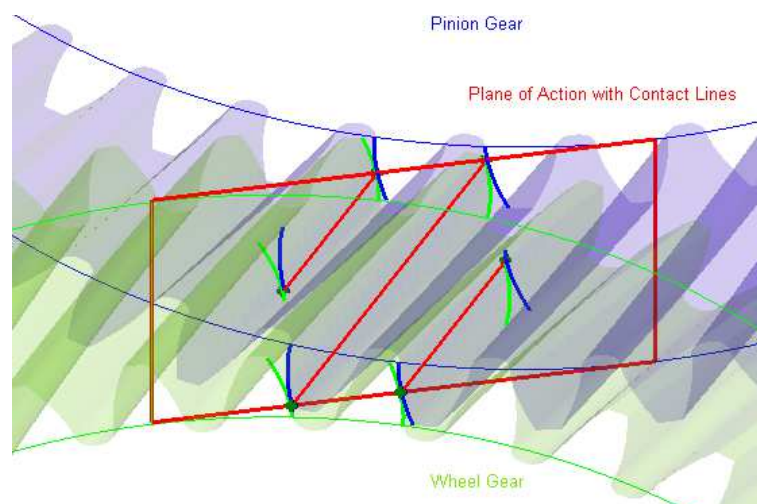


Figure 5: Contact lines in the plane of action of a helical gear (source: [3], chapter 2.2.5.4.2.)

After the intersection points of the flanks with the plane of action are detected, the start and endpoint of the contact lines for all teeth in contact can be obtained as shown by figure 5. The plane of action, the contact lines and later the contact points are expressed as parameter  $t_1$  (width direction) and  $t_2$  (involute/height direction), as shown in figure 6. The contact line for spur and helical gears follow a straight line for ideal involute shaped flanks and parallel gear axis.

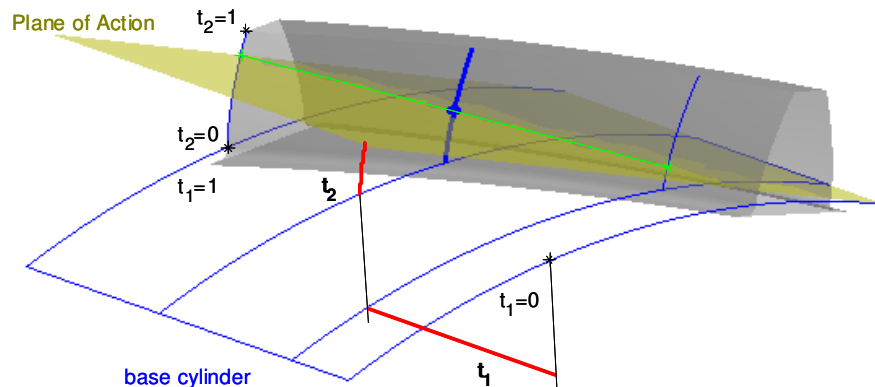


Figure 6: Internal description of the contact points via parameter  $t_1$  and  $t_2$  (sourc:[7])

Generally, the detection and the determination of the contact lines are conducted based on the entire flank surface but not based on the discretization into slices, which is a major advantage with regard to computational effort. Further, the contact computation presupposes ideal conditions such as parallel axis, which means that, for example, misalignments are not reflected by the contact lines but treated afterwards. (source: [3], chapter 2.2.5.4.2.)

### 3.4 Constitution of the deformation field

For the constitution of the deformation field, the discretization into slices is now applied. For each slice the penetration area, which is the value of displacement multiplied by the slice width, is determined based on the determined contact lines. For a slice  $i$  with the width  $b_i$ , the penetration area is computed as outlined in the equation 1.

$$A_{Penetration,i} = (d_{Pinion,mod,i} + d_{Gear,mod,i} - s_{PoA}) \cdot b_i$$

Equation 1: Penetration area of the slice  $i$  (source: [3], chapter 2.2.5.4.3.)

$s_{PoA}$  denotes the distance between the tangent points of the contact line on the base cylinders of pinion and gear, measured in the mid-section of the slice  $i$ . Parallel and angular misalignments are considered by this quantity.  $d_{Pinion,mod,i}$  and  $d_{Gear,mod,i}$  are measured between the tangent point of the base cylinder and the contact point on the corresponding flank surface. The last two quantities consider modifications and corrections of the flank surface. All three quantities are calculated by averaging three calculated deformation values, which are positioned at the beginning, in the middle and at the end of each slice.

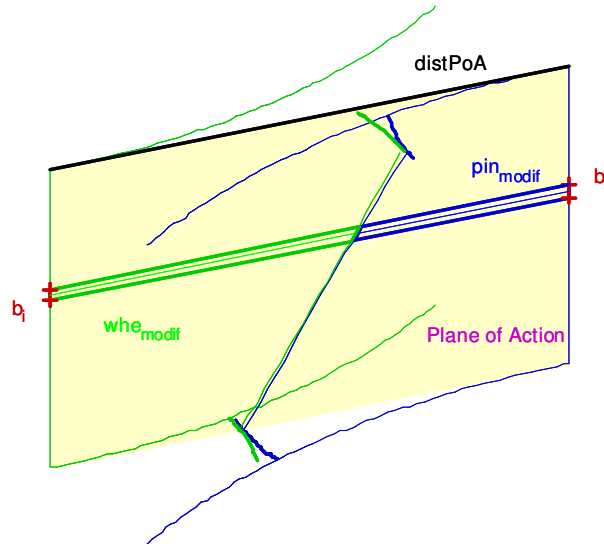


Figure 7: Determination of the penetration area for a slice  $i$  (source: [3], chapter 2.2.5.4.3.)

After the calculation of the penetration area is done for each slice and each flank pair in contact, the deformation field is constituted. Figure 8 visualizes the deformation field of a gear mesh. (source: [3], chapter 2.2.5.4.3.)

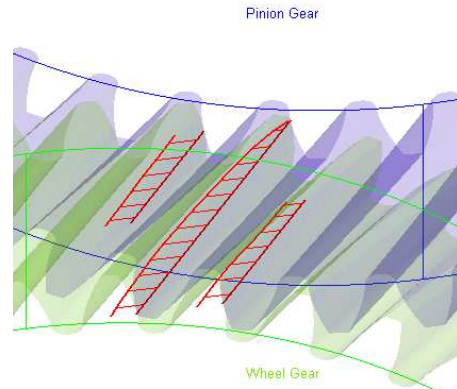


Figure 8: Deformation field (source: [3], chapter 2.2.5.4.3.)

### 3.5 Theoretical pressure distribution at the tooth contact

In comparison with a slider bearing, the tooth contact offers less favourable conditions to establish a lubrication film. However, studies have pointed out that the contact, based on the adhesive strength of the lubrication, can be described by the elasto-hydrodynamic lubrication-theory (EHL). The figure 9 shows the contact pressure of a roller contact based on the hydrodynamic, the elasto-hydrodynamic and the Hertzian theory. While the lubrication gap is constant in the hydrodynamic theory, it is shortened at the end of the contact in EHL theory. In the ACYG joint the EHL theory can be used to compute the damping and the Hertzian pressure to compute the contact stiffness. (See [6], page 695)

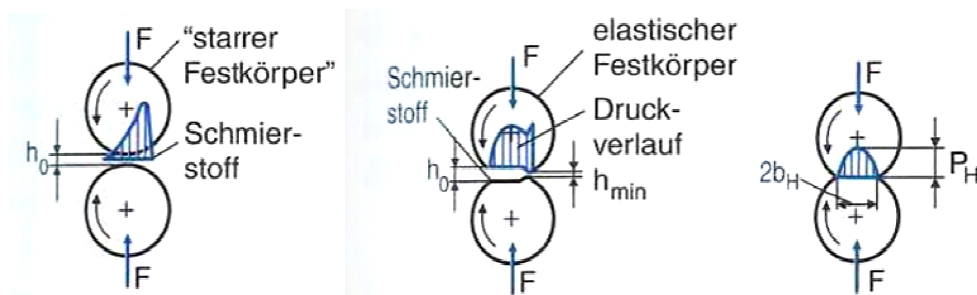


Figure 9: Contact pressure distribution of a roller contact based on hydrodynamic, elasto-hydrodynamic and Hertzian theory (source: [6])

### 3.6 Contact Force Calculation

The elastic meshing forces in the normal direction of the flanks in contact and subsequently the moments are computed by a simple penetration-force relationship for each slice node separately. In the ACYG joint, the total penetration, respectively the deformation of the gear mesh consists of three shares: The flank contact penetration  $\delta_c$  (aka Hertzian flattening), bending of the tooth  $\delta_b$  and tilting of the tooth  $\delta_t$  within the wheel body. After each penetration/deformation is computed for all flank pairs the total penetration is summed up as follows (see[7]):

$$penetration = \delta_c + \delta_{tPin} + \delta_{tWhe} + \delta_{bPin} + \delta_{bWhe}$$

*Equation 2: Total penetration (source:[7])*

#### 3.6.1 Flank contact penetration

The flank contact penetration, which is resulting from the contact of the flank surfaces, can be approached in two different ways. Either it can be assumed on the basis of the contact stiffness, which is defined by the user (e.g. 10E8 N/m) or computed using the Hertzian theory modified by Petersen [8]. Additionally to the Hertz approach which is based on the assumption of infinite half-spaces, the Petersen modified Hertz' theory takes into account the finite space which is given by the thickness of the teeth. The penetration is evaluated in dependence of the normal force, the slice width, the contact length, the Young's modulus, the Poisson's ratio and the distance between the contact point and the tooth axis, as outlined in equation 3.

$$penetration = \delta_c = \frac{F_c}{\pi \cdot b} \left( \left| (1 - \nu) \ln \left( \frac{b_c^2}{4t_{pin}^2} \right) + \nu \right| + \left| (1 - \nu) \ln \left( \frac{b_c^2}{4t_{whe}^2} \right) + \nu \right| \right) \frac{1 + \nu}{E}$$

*Equation 3: Flank contact penetration by Petersen modified Hertz theory (source:[7])*

The figure 10 shows the corresponding sketch, where  $r_b$  represents the base circle radius of the gear wheels,  $\rho$  the curvature of the teeth in the contact point and  $\delta_c$  the flank contact penetration.

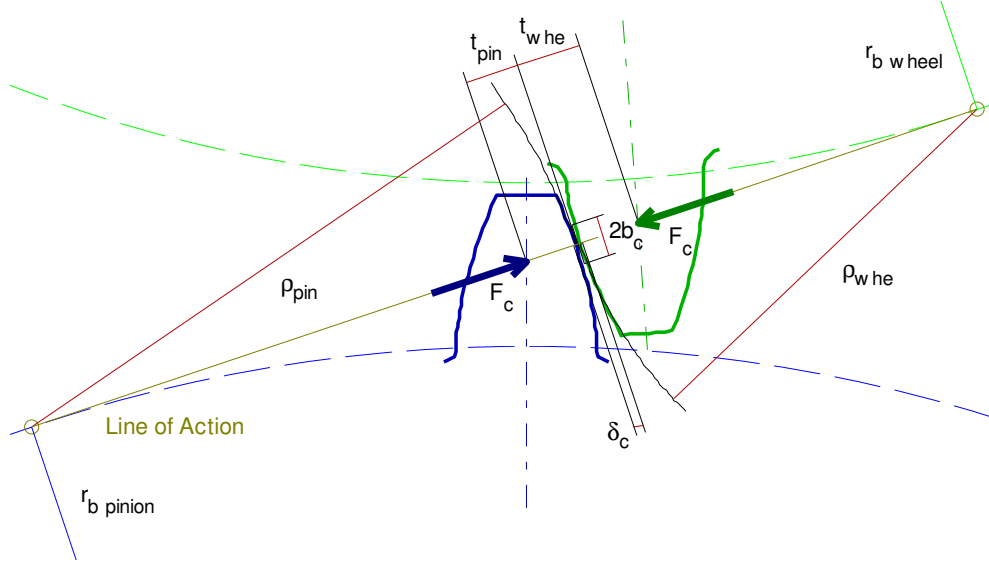


Figure 10: Petersen modified Hertz Penetration (source: [7])

With the total distance in the plane of action, the contact length  $b_c$  can be evaluated from the ideal geometry

$$b_c^2 = \rho_{pin}^2 - \left( \frac{distPoA^2 + \rho_{pin}^2 - \rho_{whe}^2}{2 \cdot distPoA} \right)^2$$

Equation 4: Contact length of Hertz contact computed via ideal geometry (source:[7])

Additionally it is defined through the roller contact equation according to Hertz.

$$b_c = \sqrt{\frac{8 F_c \rho_{pin} \cdot \rho_{whe} (1 - \nu)}{\pi b (\rho_{pin} + \rho_{whe}) E}}$$

Equation 5: Contact length of Hertz contact (source:[7])

To solve these implicit equations, an iterative method that delivers a solution for each slice is used. Moreover, the shift of the contact point position due to the deformation influences contact force calculation itself. (See [7])

### 3.6.2 Bending of the Teeth

The ACYG joint provides two options to compute the bending of the teeth: Switched 'Off', which means that no deformation share from tooth bending is considered, or computed according to the Weber/Banaschek approach [9]. To calculate the bending of the teeth, they are considered as Euler-Bernoulli cantilever beams which are supported in the gear body and bended by the normal force at the contact point. The deformation is calculated in dependence of the normal force  $F$ , the slice width  $b$ , the pressure angle  $\alpha_{press}$ , the Young's modulus  $E$ , the Poisson's ratio  $\nu$  and the infinite element, shown in equation 6 and the corresponding figure 11.

$$\delta_b = \frac{F}{b} \cos^2(\alpha_{press}) \frac{1 - \nu^2}{E} \left[ 12 \int_0^{y_F} \frac{(y_F - y)^2}{(2x)^3} dy + \left( \frac{2.4}{1 - \nu} + \tan^2(\alpha_{press}) \right) \int_0^{y_F} \frac{dy}{2x} \right]$$

Equation 6: Bending of the tooth according to Weber/Banaschek (source:[7])

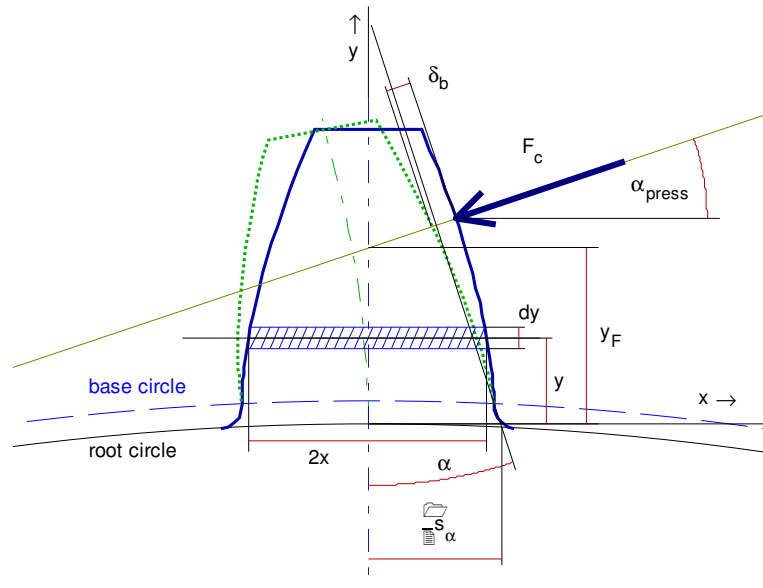


Figure 11: Tooth bending according to Weber/Banaschek (source:[7])

The bending of the tooth is a function of the integral of the tooth width over the height. To enable any modification of the flank surface these integral would have to be solved numerical, which would be an unacceptable impact on the performance. Therefore a quadratic approximation of the flank surface respectively the involute is used. Since the root curve would have a major influence on the quadratic approximation, it is skipped in the approximation and the quadratic curve starts at the base circle diameter. (See [7])

### 3.6.3 Deformation of the wheel body

The structural flexibility of the wheel body leads to body induced tooth deflections or more specifically deformation caused by the tilting of the tooth within the wheel body. In addition to that, it includes radial as well as tangential deflections of the tooth with respect to the supporting wheel body. On the whole, four options are supported to be considered in the software. The deformation of the wheel body can be totally disregarded, or computed by the approach according to Weber/Banaschek. Additionally, it can be computed by an approach proposed by Sainsot/Velex [10]. Due to the Sainsot/Velex approach, the tooth is assumed as a rigid body and the gear body as a circular, thick-walled ring based on the theory of Muskhelishvili. The last options to compute the stiffness of the wheel body is via EXCITE flexible body which considers a full flexible body by using circumferential retained nodes placed close to the root area of each individual tooth. In case that the deformation is computed according to the approach of Weber/Banaschek, the gear body is regarded as a flexible half-space while the tooth is assumed to be rigid. The computation is carried out as outlined in the equation 7 and the figure 12 (see[7]):

$$\delta_t = \frac{F_c}{b} \cos^2(\alpha_{press}) \frac{1 - \nu^2}{E} \left[ \frac{18 y_F^2}{\pi s_\alpha^2} + \frac{2 - 4\nu y_F}{1 - \nu s_\alpha} + \frac{4.8}{\pi} \left( 1 + \frac{1 - \nu}{2.4} \tan^2(\alpha_{press}) \right) \right]$$

Equation 7: Tooth tilting according to Weber/Banaschek (source:[7])

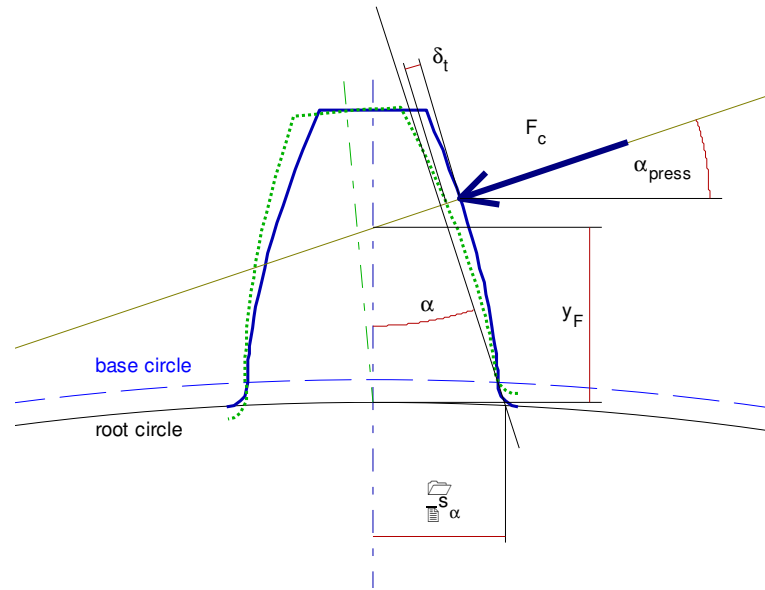


Figure 12: Tooth tilting according to Weber/Banaschek (source:[7])

#### 4. Current status of established contact simulation tools

In order to investigate gear vibrations, scuffing, micropitting (aka grey straining) and strength, capabilities of a gear mesh in its design phase, the use of contact analysis software is required and meanwhile became state of the art. In addition to that, such software is used to optimise the load distribution and consequently the gear stress by a modification of the micro geometry of the tooth flanks.

Most commercial software packages use FEM methods, analytical methods or a mix of both to resolve the contact and to account for elastic deflections of the involved structures. FEM methods are very time consuming but deliver very accurate results. However, FEM-based methods often suffer under discretization issues and require special care to rule them out reliably. In contrast, analytical methods are based on stiffness formulas which provide results nearly instantly, while the accuracy of the results is very limited. However, the tooth contact analysis is not yet standardized and so each software is validated through measurements, FEM calculations or field experiences.

In the following the most commonly used software tools are described. Owing to the fact that KISSsoft is used for the evaluation in this master thesis, this software is discussed in the chapter 5 in more detail. (See [11])

#### **4.1 LVR**

LVR (abbreviation for Last-Verteilungs-Rechnung) originates to the Technical University of Dresden and was developed for an application in the early phase of a product life cycle to reduce iteration steps during the design of the gear box. Beside the pressure and load contact temperature computation, it also enables the computation of root stress for the outer gears. Generally, LVR uses analytical methods to compute the contact. On the other hand, deformations of the housing are for example computed by using FEM methods, which are then applied to the gear mesh. [12]

The same stiffness, respectively deformation model as in ECXITE or KISSsoft (namely those according to Weber/Banaschek) is used. LVR applies a slicing in the normal cut of the gears. Single pitch deviations, tooth width variations and center distance deviations are also processed. Furthermore, LVR enables the computation of planetary gear sets and considers the elastic deformation of the gear body, the elastic tilting difference of roller bearings, the torsion deformation of the planet carrier, the tilting of the planet caused by the sliding of the bearings, effective helix angle modification, elastic deformation of tooth flank, elastic deformation difference of planet carrier bearing and the deformation of the housing. (See [13])

## 4.2 RIKOR

The software RIKOR, which is developed under the patronage of the Forschungsvereinigung Antriebstechnik (FVA), enables comprehensive deformation analysis of gear boxes, including the gears, shafts and bearings. The stiffness model of RIKOR, as shown in figure 13, uses a discretization into slices, which considers the transverse deformations and the twist of the shaft but no tooth bending or tilting in the mutual computation. Therefore, effects resulting from mutual support, like buttressing, are not taken into account. The computation of the housing is based on FEM, where a FEM-mesh can be imported. The load distribution is calculated analytically but considers the meshing stiffness computed by FEM [14]. Resonance frequencies and modes of the gear box can be obtained on the basis of calculated stiffness values resulting from the geometry and the mass[15]. (See [11])

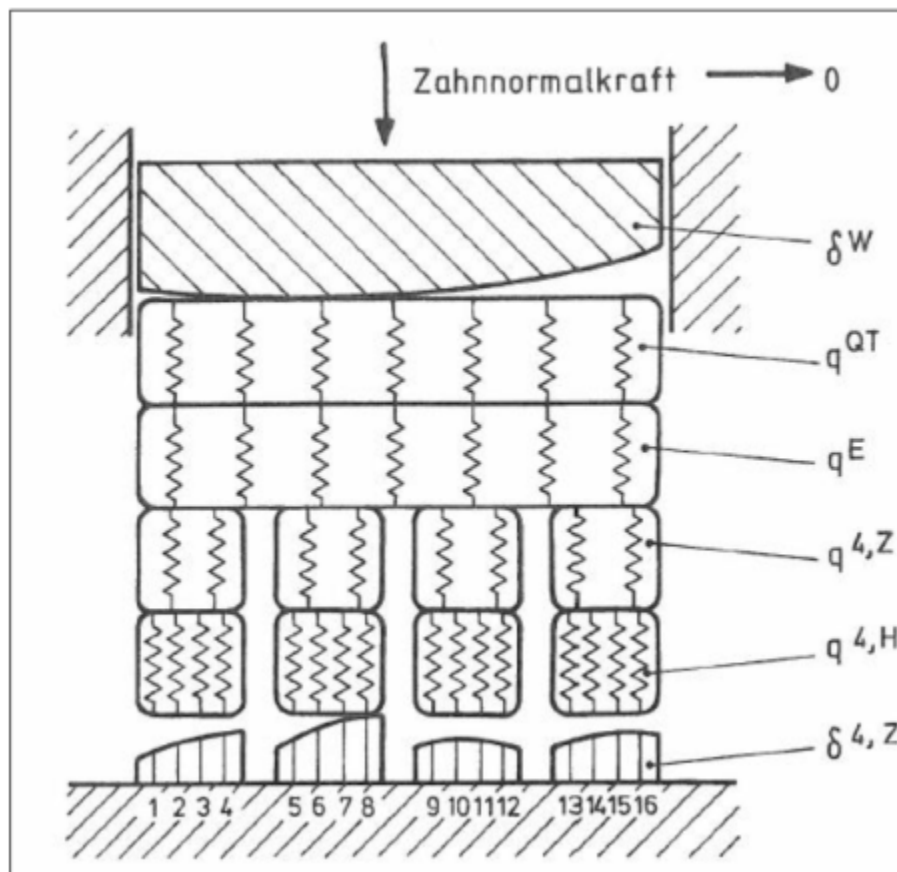


Figure 13: Stiffness model in RIKOR for four flank pairs and four slices (source: [11])

### **4.3 STIRAK**

STIRAK which originates to the RWTH Aachen computes the necessary quantities like gear data, topology of the flank surface, wheel body deformation or load initiation via a numerical simulation. The entire contact geometry and stiffness computation is based on a finite element method. As a consequence, the meshing stiffness is computed depending on the exact tooth shape and tooth root rounding. Since the computation of the Hertzian stiffness would require a very fine grid, which would increase the simulation time significantly, only the stiffness of the structural model is processed by using FE. In addition, if the calculation is done for one macro geometry, the characterization of the stiffness behaviour is used for further calculations. Basing on this characterization, the topology of the flank surface and load can be changed and computed without having to run the finite element method solver again. (See[15])

### **4.4 Romax**

Romax uses a finite element numerical analysis tool to compute gear bending strength and takes distortions of the rim form into account. It can also handle thin rim gears and high loaded gears. Moreover, a root stress analysis is supported and lubricant additives can be considered during the simulation. The micro geometry can be determined by an automated optimization tool or by user input. (See [16])

## **5. KISSsoft**

The software KISSsoft from KISSsoft AG is a tool for sizing, optimizing and recalculating designs of machine components, like gears, shafts and bearings, screws, springs, joining elements and belts. The cylindrical gear calculation in KISSsoft includes single gears, planetary gear sets and wheel chain gear sets. Further it can be integrated in CAD programs. This function is later used in this thesis to compare the gear geometry with EXCITE.

In this thesis KISSsoft has been chosen as a validation reference for the contact pattern results obtained by EXCITE. Motivation for selecting KISSsoft is that it is used throughout AVL as a standard tool for gear design and moreover is widespread and highly accepted throughout the industry. (See [17])

## **5.1 Cylindrical Gears**

In case of single cylindrical gears, the software has been designed to enable the calculation of the geometry of individual gears. In addition to the standard tooth contact analysis, the cylindrical gear calculation provides additional evaluation options (see [17], page 262):

- For cylindrical gears KISSsoft can calculate the life time using the Palmgren-Miner rule and the reliability following the Weibull-distribution.
- A strength calculation (e.g. AGMA) of the gears with respect to a certain load spectrum is also implemented.
- Scuffing capacity as well as the internal and the flash temperature can be computed.
- The pre and final-machining, which influences the shape of gears can be defined by the user. Furthermore, the tooth form input window offers advanced options for a precise definition of the cutting tool.
- Profile and tooth trace modifications are supported.
- Safety against tooth flank fracture in accordance with Dr. R. Annast
- The gear contact mesh can be computed in more detail with a contact analysis.

### 5.1.1 *Contact analysis*

In addition to pure static calculations, KISSsoft offers an advanced contact analysis where the load is considered while calculating the path of contact. The meshing stiffness can be computed apart from a constant value, according to Weber/Banaschek or the standard ISO 6336-1. It also enables a computation of the transmission error (TE) of the gear mesh. The contact analysis offers the possibility of representing a more detailed solution of the gear mesh contact.

Furthermore, dynamic effects due to dynamic factors, like an alternating moment, can be applied. Gear mesh misalignments can be derived from these dynamic factors or by the deformation of the shafts. With the computed force distribution over the gear width a more precise face load factor  $K_{H\beta}$  can be calculated. Finally, single pitch deviation, friction, manufacturing allowances and an iterative wear calculation are also provided. (See [17], page 411)

### 5.1.2 *Meshing stiffness*

The contact analysis provides three options regarding processing the meshing stiffness. The first option is to calculate the meshing stiffness according to the formulae in the standard (ISO 6336, DIN 3990, etc.) using empiric formulae. Computing the meshing stiffness according to Petersen[8], which is based on Weber/Banaschek [9], is the second option. Just as implemented in EXCITE it takes tooth bending, tooth tilting, as well as Hertzian pressure into account. The last option is to set the contact stiffness by a constant value.

### 5.1.3 Discretization

Where EXCITE uses a discretization of slices in width direction for spur and helical gears, KISSsoft applies a discretization in the direction of the normal cut of the teeth as shown in the figure 14. The figure shows a helical gear with the helix angle  $\beta_y$ , the gear width  $b$  and the slice width  $b_s$ . The spring stiffness  $C_{RK+B}$  represents the combined stiffness of tilting and bending of the tooth, where  $C_C$  represents the coupling stiffness and  $C_H$  the Hertzian contact stiffness. The coupling stiffness enables a mutual support between the slices. The amount of support can be adjusted with the slice coupling factor, as outlined in chapter 5.3.1. (See [17], page 416)

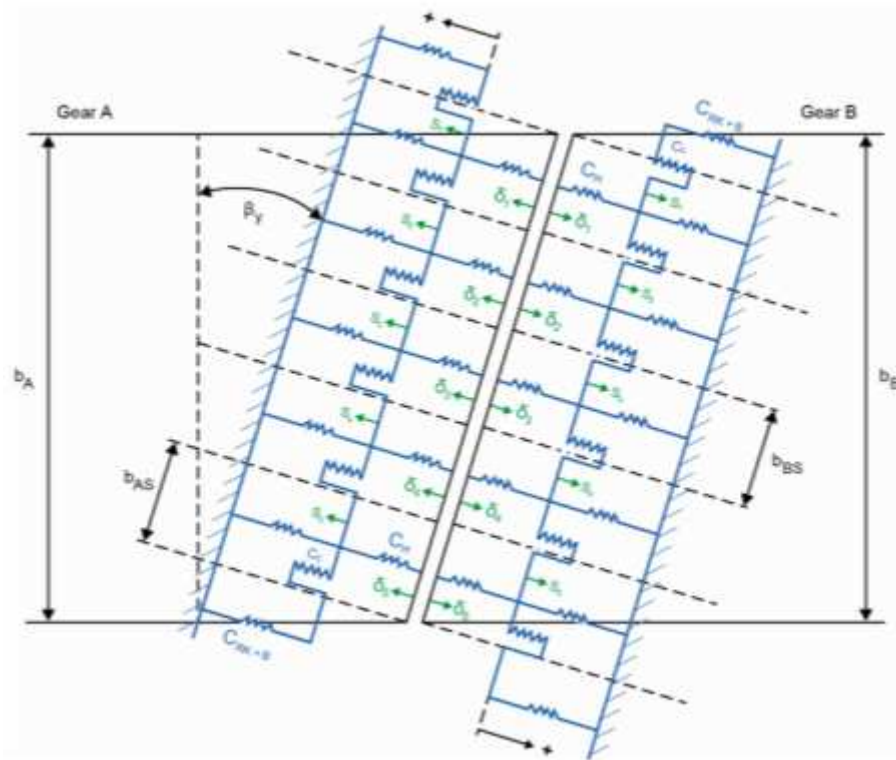


Figure 14: Discretization of the common gear width into slices in KISSsoft (source: [17], page 416)

## 5.2 Consideration of dynamic effects in KISSsoft

Kisssoft is neither a multi-body dynamics simulation like EXCITE nor a finite element software, which means that dynamic effects cannot be computed. However, KISSsoft provides several options to apply empirical factors to represent effects like resonance or an alternating load. (See [17], page 313)

- Transverse coefficient

The transverse coefficient  $K_{H\alpha}$  incorporates irregular contact characteristics across a number of teeth. Depending on the predefined accuracy grade, the transverse coefficient rises with the contact ratio. It is computed in accordance with the activated calculation method.

- Dynamic factor

Increased forces induced by natural frequencies as resonances in the tooth mesh are taken into account by the dynamic factor. It is computed according the selected calculation method or can be inputted by the user, if it is available from measurements for example.

- Alternating bending factor

To consider swinging loads on the tooth root caused by alternating bending loads, especially for the strength calculation, the alternating bending factor  $Y_M$  is applied. The alternating bending factor depends on the selected calculation method.

## 5.3 Empirical factors

The contact analysis in KISSsoft offers the possibility to present extended effects of the contact calculation, like buttressing, by empirical factors. The default values were verified by KISSsoft via a comparison with the results of the most frequently used programs in the German language area [11]. (See [17], page 313-316)

### 5.3.1 Slice coupling factor

The slice coupling factors represent the possibility to adjust the linking of adjacent slices. A higher factor means a higher support of higher loaded slices by adjacent less loaded slices. The contact stiffness of one slice thus is a function of the stiffness from Hertzian pressure  $C_H$ , the root stiffness as defined by Weber/Banaschek  $C_{Pet}$  and the slice coupling stiffness  $C_C$  as pictured in the figure 15.

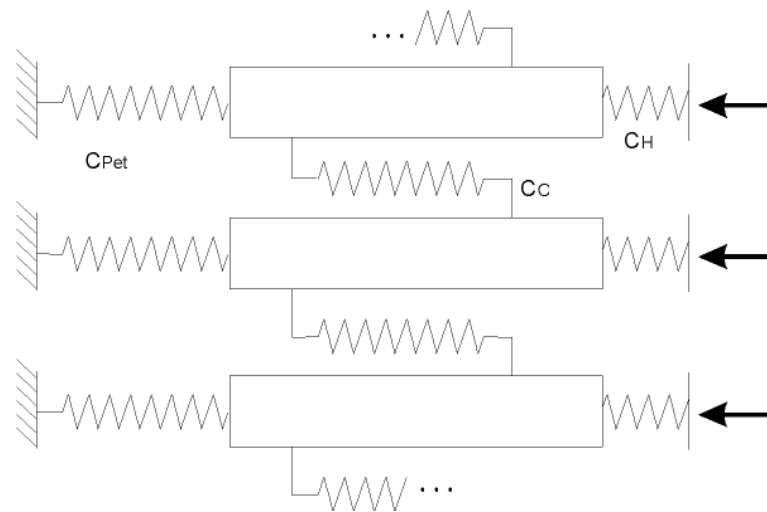


Figure 15: Coupling of the slices in KISSsoft (source: [17])

The coupling stiffness  $C_C$  is computed as outlined in equation 8, in which  $A_{sec}$  is the total number of slices and  $C_{Pet}$  the stiffness of the tooth.

$$C_C = 0.04(A_{sec})^2 \cdot C_{Pet}$$

Equation 8: Coupling stiffness as implemented in KISSsoft (source: [17])

The default value of the slice coupling factor is set to 0.04 which is confirmed by comparative calculations with FEM. The slice coupling leads to increased forces especially at the beginning and end of the contact. This is in particular the case with helical gears, where neighbouring slices do not hold any load, at the edge of the contact pattern as shown in figure 16. (See [11])

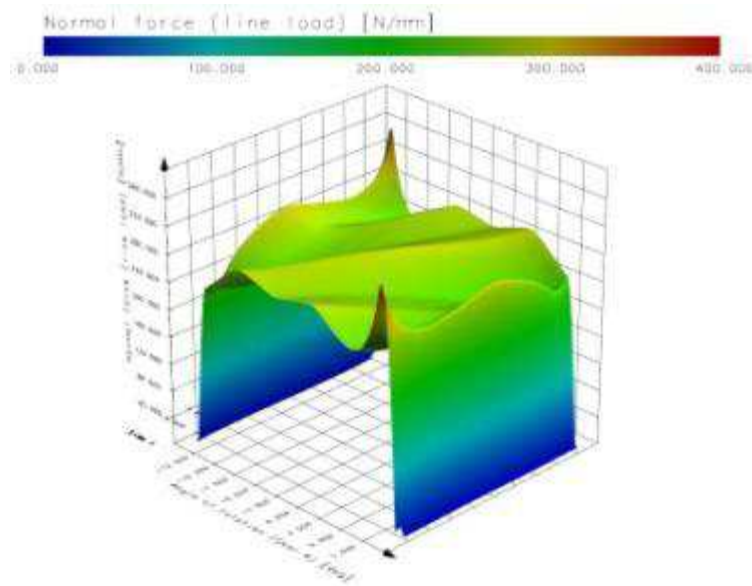


Figure 16: Contact pattern of a helical gear mesh with applied slice coupling

### 5.3.2 Border weakening factor

KISSsoft applies the empirical border weakening factor to depict the buttressing effect of helical gears. This means that the reduced tooth thickness with respect to the normal cut at the edges of the gear mesh lowers the stiffness of the tooth. The equation 9 shows the computation of the reduced tooth stiffness while the tooth thickness  $s_n$  and the reduced tooth thickness  $s_{red}$  are represented in figure 17.

$$C_{Pet\_border} = C_{Pet} \left( \frac{s_{red}}{s_n} \right)^{0.5}$$

Equation 9: Border weakening factor as implemented in KISSsoft (source: [17])

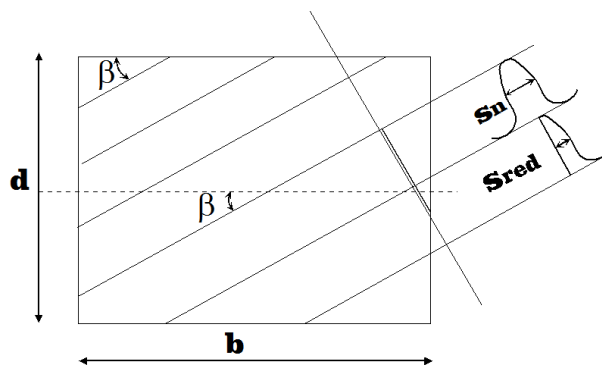


Figure 17: Reduced tooth thickness of a helical gear (source: [17])

As result of this calculation, the gear mesh shows reduced forces at the edges as shown in figure 18. The default value 0.5 was evaluated in comparative analyses with FEM and LVR. (See [17])

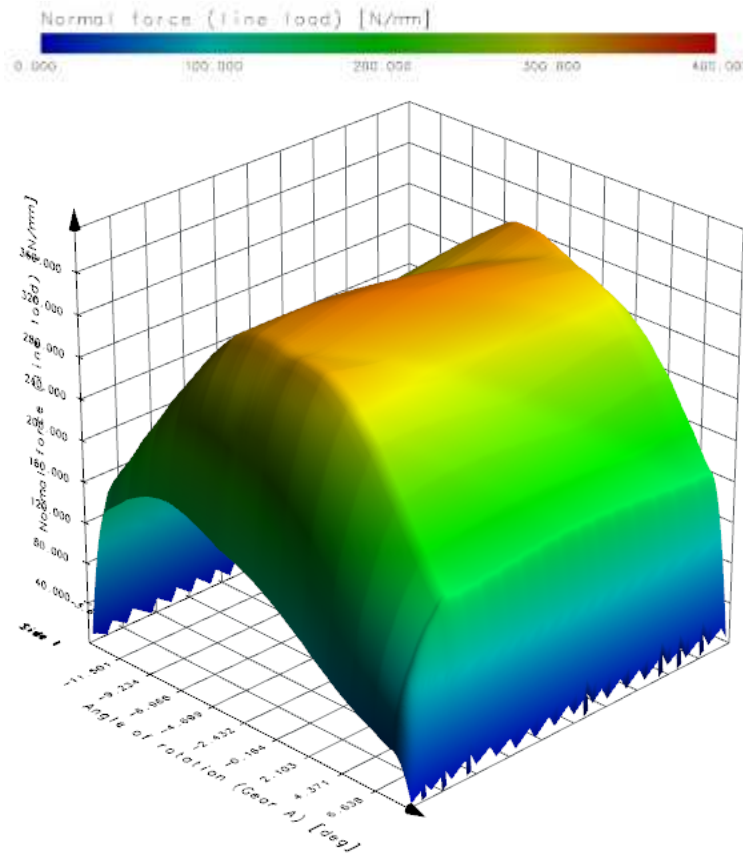


Figure 18: Contact pattern of a helical gear mesh with applied slice coupling

### 5.3.3 Stiffness correction factor

The computed Hertzian contact stiffness strongly depends on the curvature of the mating surfaces. Large variations in the curvature during the contact lead to local high values in Hertzian pressure. That means that subsequent calculations like micropitting may deliver incorrect results. As a consequence the following algorithm according to Winter/Podlesnik [18] is applied.

The correction of the contact stiffness respectively the smoothing of the curvature is only applied if the curvature is greater than 1.01 times the normal module. For each diameter, two adjacent diameters (one with 0.3 times the normal module smaller and one with the same amount bigger) are computed. If the curvature of the smaller diameter is greater than the current one, then the smaller is used as correction curvature for further calculation, otherwise the other one. The new curvature relies on the formula

$$\rho_{yNew} = SmmothFactor \cdot DiaFactor \cdot \rho_{Corr} + (1 - SmoothFactor \cdot DiaFactor) \cdot \rho_{yold},$$

Equation 10: Smoothed curvature according to Winter/Podlesnik (source: [17])

with the *DiaFactor* as outlined in figure 19.

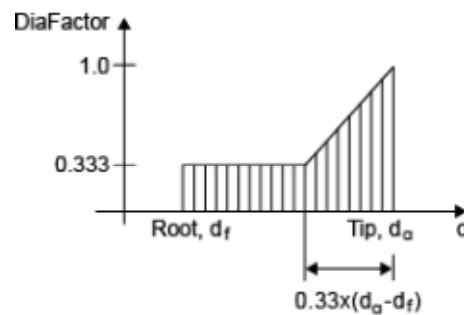


Figure 19: *DiaFactor* depended on the current diameter (source: [17])

The standard stiffness correction factor is 0.8, where zero means no smoothing and one means full smoothing. (See[17])

## 6. Gear mesh misalignments and possibilities of their compensation

The face load distribution is widely affected by gear mesh misalignments. These misalignments are primarily caused by elastic deformation during operations such as deformations of the bearings, the shafts, the wheel bodies and the housing of the transmission, as shown in figure 20. Other reasons are errors in the manufacturing process like errors of the bore holes, toothing errors or the clearance of the bearings. Errors in the assembly result in gear mesh misalignments too. (See[19], page 270)

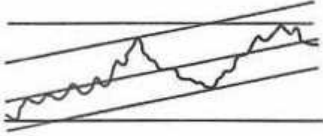
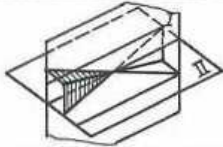
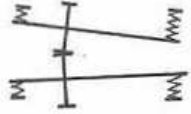
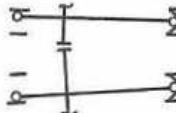
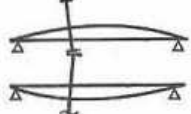
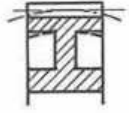
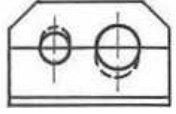
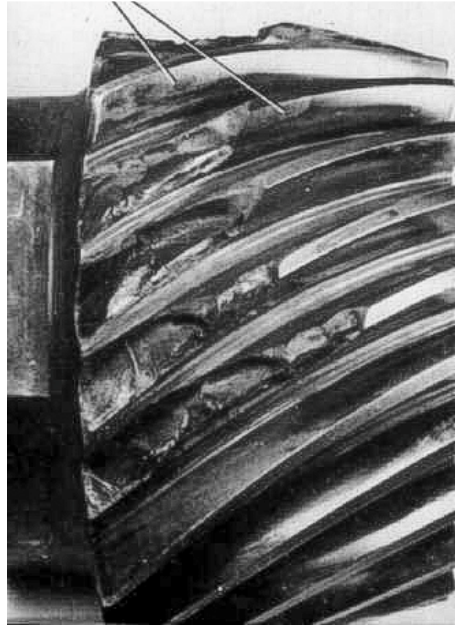
	Toothing errors
	Borehole errors
	Bearing deformation
	Bearing clearance
	Shaft deformation (bending, torsion)
	Wheel body deformation
	Housing deformation

Figure 20: Various possible errors which affect mesh mesh misalignments (source: [19])

As a result of gear mesh misalignments, the distribution of the face load deviates from the predicted distribution and leads to an increase of contact and bending stress. Furthermore, the rise of contact stresses is accompanied by the rise of gear whine noises. Figure 21 shows a tooth fracture at one end of a gear wheel which was caused by angular misalignments.



*Figure 21: Gear fracture as result of angular misalignments (source [20])*

Gear mesh misalignments can be divided into parallel and angular misalignments. Both types can be measured based on the plane of action or based on a specific coordinate system, which is more common in the industry. In this thesis the misalignments are measured based on the joint coordinate system.

In the following, the individual errors and their impact on the so called engagement field plot are explained. The engagement field plot is a popular graphical representation of the evolution of the gear contact pattern during roll-off. For comparison, the engagement field plot of a gear mesh without any misalignment, as shown in figure 22, is used. The plot shows a 2D representation of the normal force per unit length depending on the gear width and the roll distance of the pinion. The roll distance is the unwound length of the base circle radius within the transition of one tooth. The plot shows that the normal force is constant over the gear width, which means that it is an spur gear and further, there are no angular misalignments or well compensated by a modified micro geometry. The change of the force between 180 N/mm and 270N/mm is induced by the change of the number flanks pairs in contact. The number of flank pairs can be obtained by counting the areas of the similar forces. In this case, it changes between two and three. Nevertheless, the appearance of clearly separated areas does not always occur, especially if the micro geometry is modified. Further, it can be seen due to the equivalent normal force of over the roll distance for three flank pairs in contact, that the meshing stiffness is set to an constant value. (See [21] and [22])

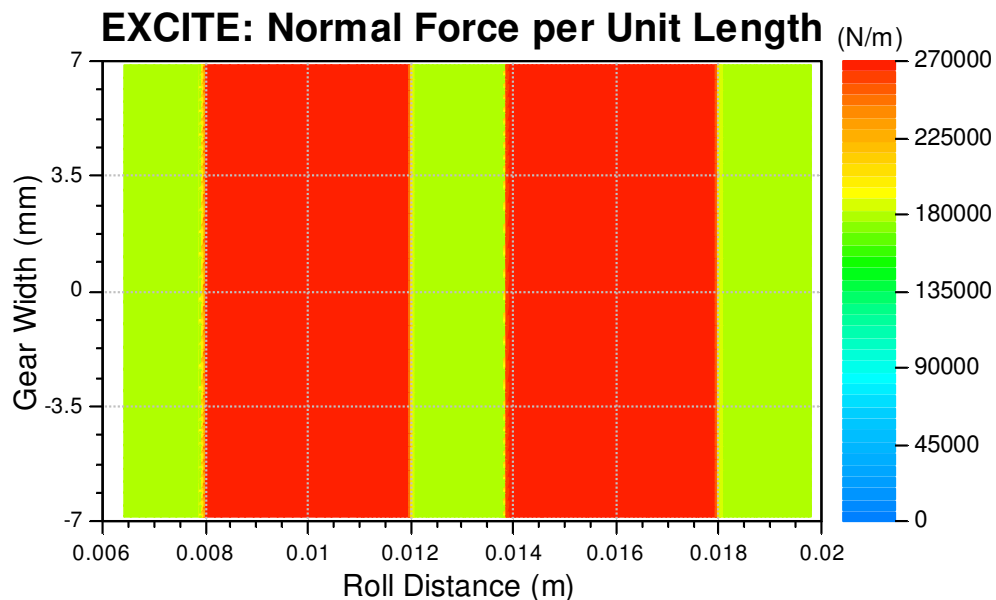


Figure 22: Engagement field plot of a gear mesh without any misalignments

## 6.1 Flank surface deviations

The flank surface deviations consider all differences between the real and the ideal flank surface. They are classified into two groups: profile deviations in the face cut (figure 23) and deviations of the flank lines (figure 24). Both types are subdivided into angular deviations, form deviation and total deviations. (see [6], page 500)

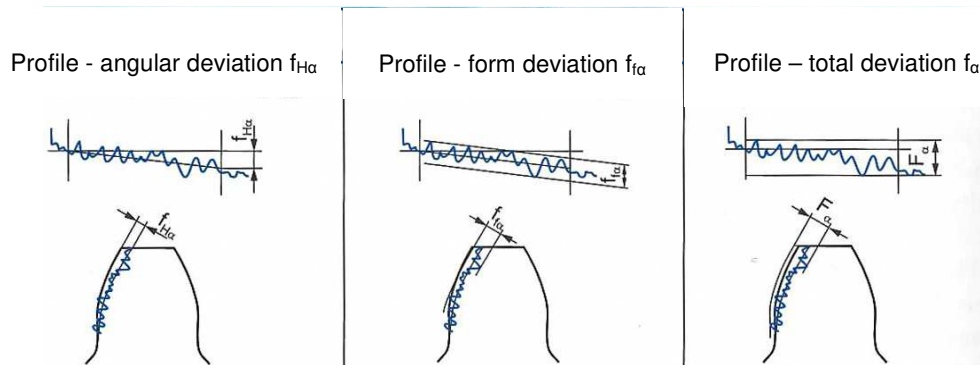


Figure 23: Profile deviations in the face cut (source: [6])

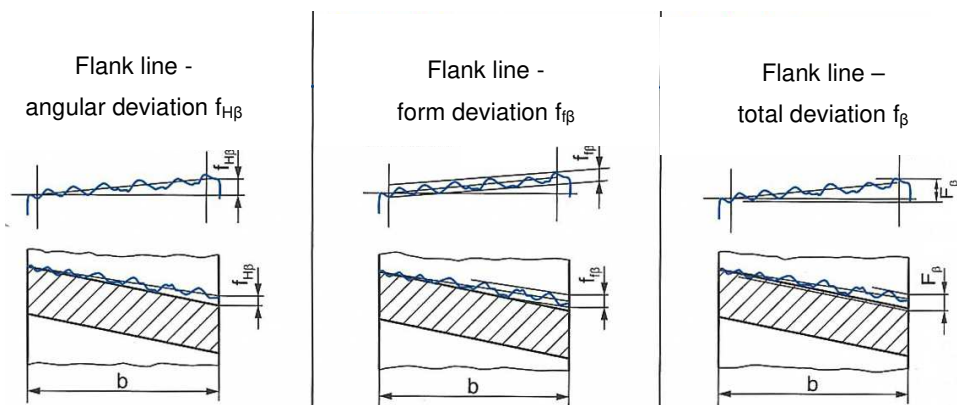


Figure 24: Flank line deviations (source: [6])

## 6.2 Run-out error

The run-out error is the greatest radial difference in the position of a conical measuring body placed in two adjacent tooth gaps as shown in figure 25. (See [6], page 506)

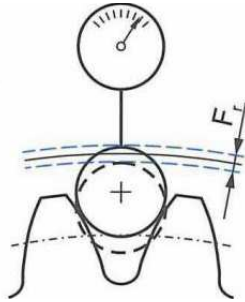


Figure 25: Run out error (source: [6])

## 6.3 Pitch deviation

The pitch deviation  $f_p$  is the difference of the real and ideal pitch  $p_t$  of the gear measured on the pitch circle diameter. It can be measured over one (figure 26) or several pitches. (See [6], page 503)

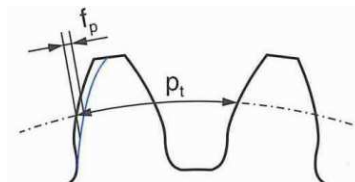


Figure 26: Single pitch deviation (source: [6])

## 6.4 Total radial composite deviation

The total radial composite deviation means the variation of the center distance when the gear is rotated one revolution with a master gear. (See [6], page 507)

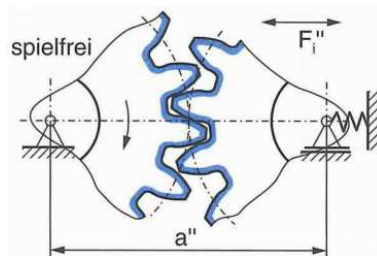


Figure 27: Total radial composite deviation (source: [6])

## 6.5 Parallel misalignment

Parallel misalignment, whether along the plane of action or orthogonal to it, results in a change of the center distance. Due to the geometrical characteristics of the involute a change of the center distance only affects the profile contact ratio. Besides from errors in the manufacturing, parallel misalignment is triggered by the bending of the shafts through radial forces of the gear mesh.

In EXCITE, there is no separate result for parallel misalignment but it can be deduced from the movements of the connected nodes. Figure 28 shows the impact of an increase of the nominal center distance, which corresponds to a parallel misalignment, on the engagement field plot of a spur gear mesh. In this gear mesh, the number of flank pairs in contact changes between two and three. The higher nominal center distance results in a lower contact ratio. This means that the contact ratio of two occupies a greater share of the engagement length, respectively of the roll distance.

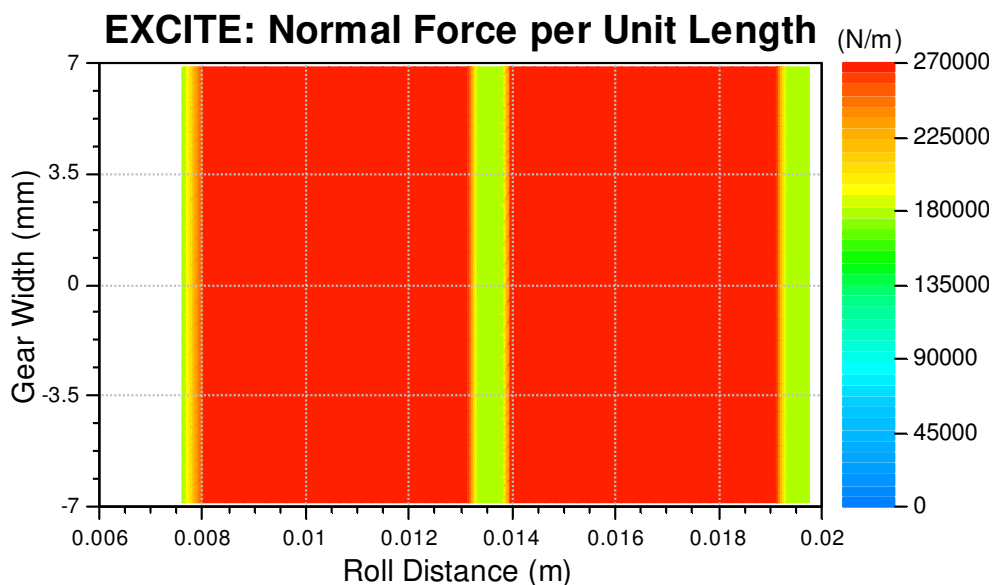


Figure 28: Engagement field plot of a gear mesh with a parallel misalignment

## 6.6 Skew misalignment

Angular misalignments, as skew and slope, changes the contact pattern resulting in a non-uniform distribution. Angular misalignment due to tilting about the first joint axes (which equals to the gear center connection), as shown in figure 29, is also called “skew”. Besides from errors in the manufacturing, it is primarily triggered by the bending of the shafts through radial forces of the gear mesh.

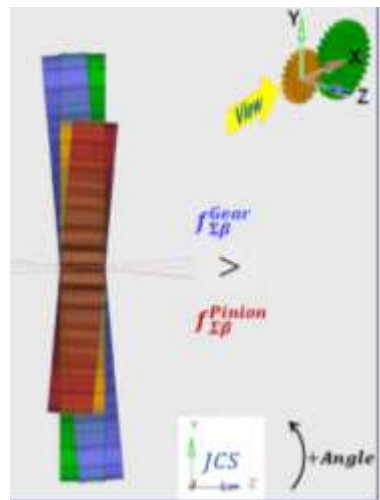


Figure 29: Definition of skew misalignment (source: [7])

In EXCITE, angular misalignments are assumed to be a linear regression of the internal nodes as shown in figure 30. The motion of the internal nodes is derived via an interpolation/extrapolation from the connected nodes of the joint. After the linear trendline is determined, the skew (or slope) misalignment is computed by the inclination of the trendline together with the effective gear width ( $b_{eff}$ ), using the Z-axis of the joint coordinate system as reference.

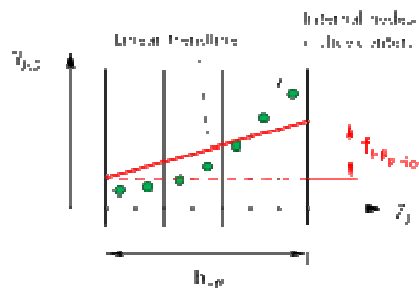


Figure 30: Determination of skew misalignment (source: [7])

Since the pinion and gear wheel have their own individual angular misalignment, the total amount is computed as outlined in the equation 11.

$$Skew = f_{\Sigma\beta}^{Gear} - f_{\Sigma\beta}^{Pinion}$$

Equation 11: Total skew amount determined from pinion and gear

The figure 31 shows the influence of a skew misalignment on the engagement field plot which results in higher contact forces on one end of the active gear width. (See [7])

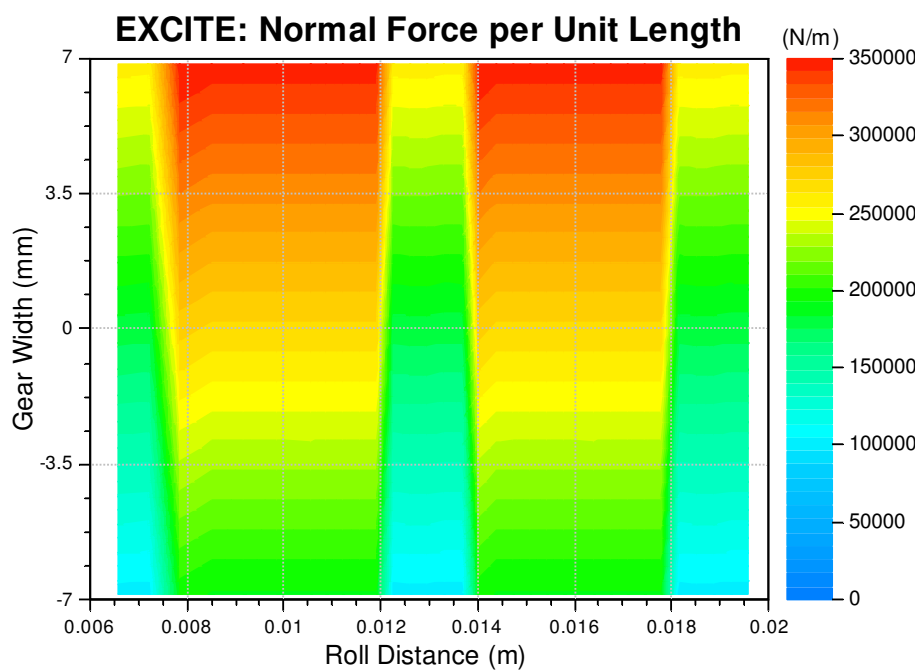


Figure 31: Engagement field plot of a gear mesh affected by skew misalignments

## 6.7 Slope misalignment

Angular misalignment due tilting about the second joint axes is also called “slope”, as illustrated in figure 32. It corresponds to the situation that on one end plane the tooth is pushed into its opposing tooth gap, while on the other end plane the tooth is drawn apart.

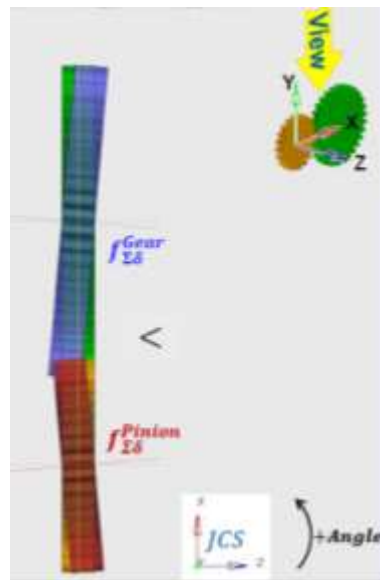


Figure 32: Definition of slope misalignment (source: [7])

Beside from errors in the manufacturing, it is primary triggered by the bending of the shafts through tangential forces of the gear mesh.

The computation of the amount of slope misalignment follows the same procedure as outlined for skew misalignments but in XZ plane, as shown in figure 33.

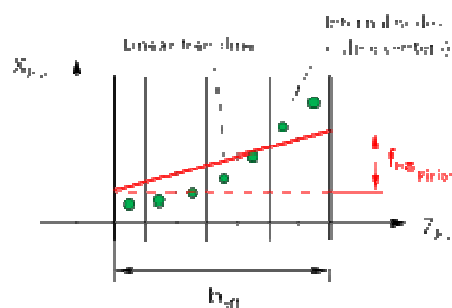


Figure 33: Determination of slope misalignment (source: [7])

The total amount of the slope misalignment is calculated by

$$Slope = f_{\Sigma\delta}^{Gear} - f_{\Sigma\delta}^{Pinion}.$$

*Equation 12: Total slope amount determined from pinion and gear*

Slope misalignment leads to higher loads at one side of the gear width, as shown in the following figure. (See [7])

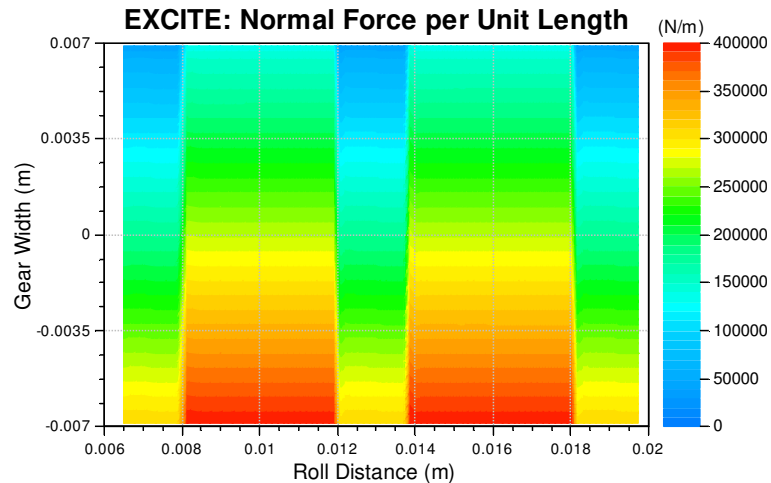


*Figure 34: Engagement field plot of a gear mesh affected by slope misalignments*

## 6.8 Compensation of Gear Mesh Misalignments

In order to ensure a uniform face load distribution during operation, the misalignments have to be compensated. This is achieved by modifications of the micro geometry of the teeth, as shown in figure 35. The most common modifications in the practise are: the correction of the pressure or helix angle (a), the pressure angle correction (b), the end relief (c), the barrelling (d), the twist (e), the crowning (f), the barrelling (g) and the diagonal tip/root relieve (h). In the following, the supported modifications in the ACYG joint are outlined. All these modifications are defined independently for pinion and gear and can be superimposed. Owing to the fact that a modification of the involute influences the mating process and the resulting meshing forces, modifications of the micro geometry have to be applied carefully to avoid an increase of impacts. Possible modifications can be classified into two groups: profile modifications and lead corrections. (See [5], chapter 4.17.5.4.)

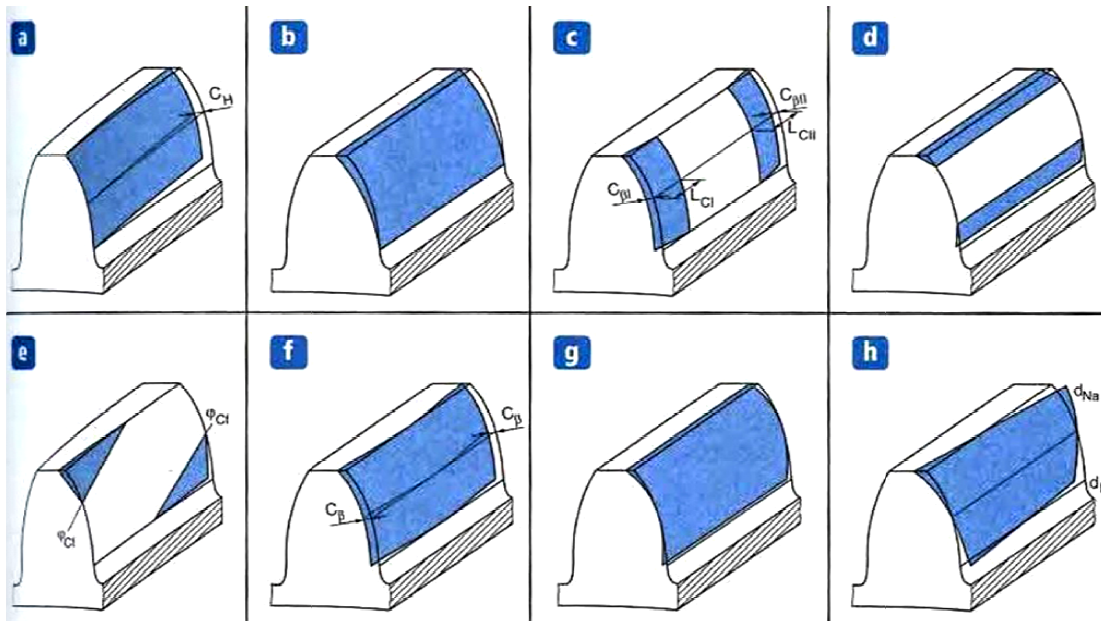


Figure 35: Possible modifications of the flank surface (source [6])

### 6.8.1 Profile modifications

Profile modifications indicate small geometrical corrections of the flank surface in the height direction of the involute. The aim is to reduce impacts during the mating process which are induced by elastic deflections of the teeth and the wheel body of the gear, manufacturing defects or by errors during the assembly, as shown by figure 36. In the following the most relevant profile modifications are outlined as they are implemented in EXCITE. (See [5], chapter 4.17.5.4.1.)

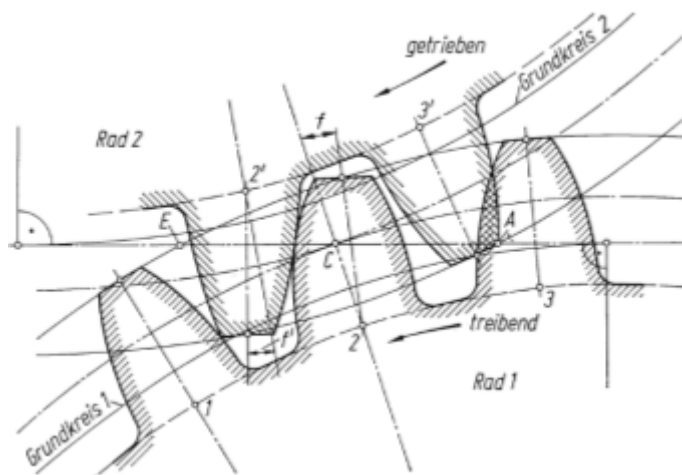


Figure 36: Pre- and disengagement impact (source: [23], page 98)

- Tip relief correction

Tip relief  $C_{\alpha a}$  as shown in figure 37 enables the removal of material in the tip region of the tooth, from diameter  $d_{Ca}$  up to the active tip diameter  $d_{Na}$ . It can be applied as a linear or a circular function.

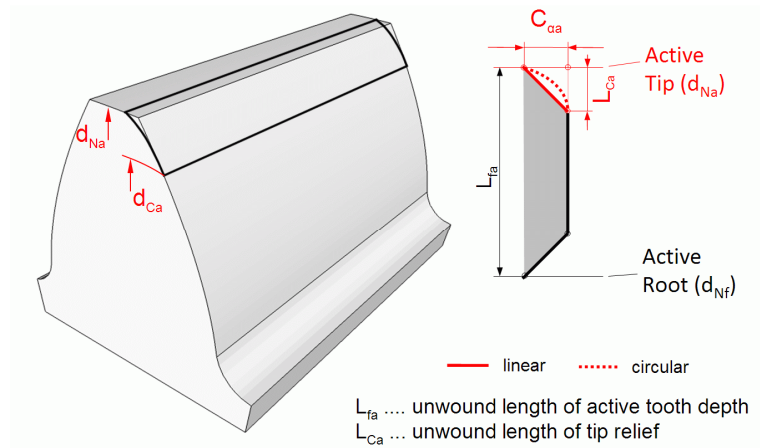


Figure 37: Tip relief (source: [5], chapter 4.17.5.4.1.)

- Root relief correction

The root relief correction  $C_{\alpha f}$  as shown in the figure 38 implies the removal of material between the active root diameter  $d_{Nr}$  to diameter  $d_{Cf}$ . Just as the tip relief correction the function can be linear or circular.

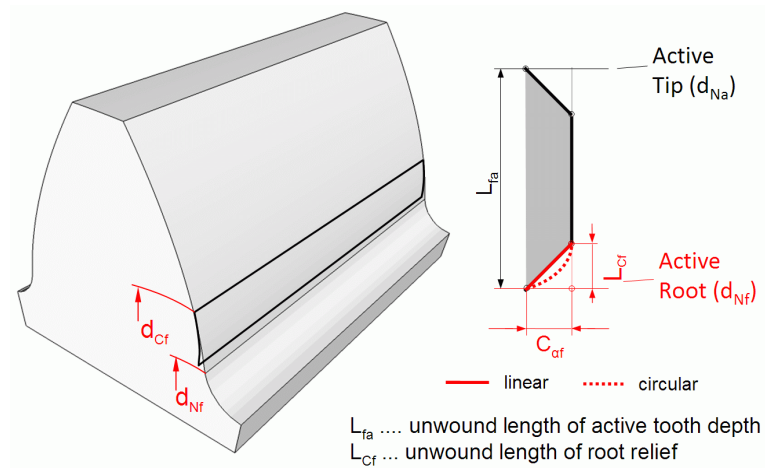


Figure 38: Root relief (source: [5], chapter 4.17.5.4.1.)

- Crowning (Barrelling)

Crowning  $C_\alpha$  denotes a barrel shaped removal of material which covers the area from the active root  $d_{Nf}$  and the active tip diameter  $d_{Na}$ , where it remains zero at the middle of the active involute length.

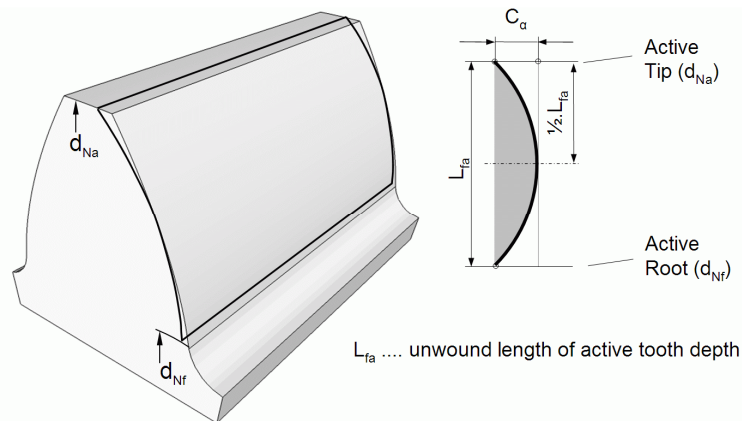


Figure 39: Crowning (Barrelling) (source: [5], chapter 4.17.5.4.1.)

- Pressure angle correction

The pressure angle correction  $C_{H\alpha}$  enables the removal of material just as the linear tip relief but with the range over the entire active involute. The shape of the material removal over the involute, follows a linear relationship as shown in figure 40.

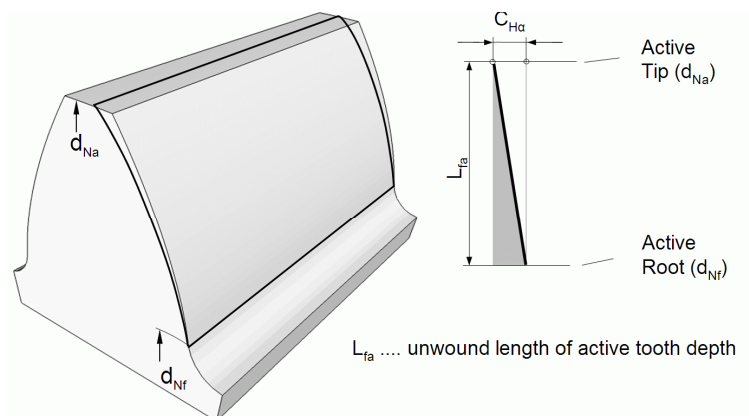


Figure 40: Pressure angle correction (source: [5], chapter 4.17.5.4.1.)

## 6.8.2 Lead corrections

Lead corrections are geometrical corrections of the flank surface which are applied in width (=lead) direction to avoid edge loading effects of the mating gears. Applied lead corrections result in a more centered zone of contact and therefore the gear mesh is less sensitive to angular misalignments. (See [5], chapter 4.17.5.4.2.)

- End relief correction

The end relief correction  $C_{\beta i}$  as shown in figure 41 implies the material removal at both end planes of the gear. The function is linear with respect to the gear width coordinate. The correction can be defined individually for both sides of the gear width.

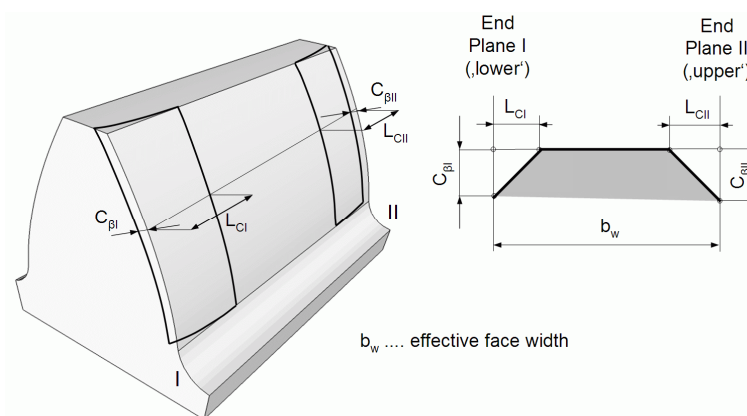


Figure 41: End relief (source: [5], chapter 4.17.5.4.2.)

- Crowning

Crowning  $C_\beta$  enables a barrel shaped removal of material similar to the barrelling correction but in width direction. Typically, it is applied to counteract random errors arising in lead directions.

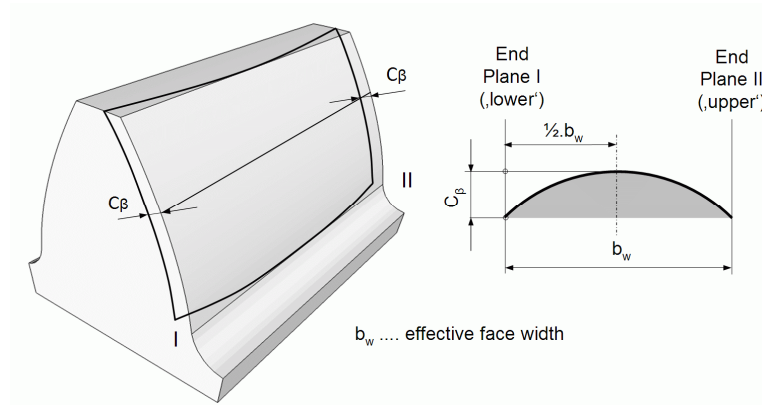


Figure 42: Crowning (source: [5], chapter 4.17.5.4.2.)

- Helix angle correction

The helix angle correction  $C_{H\beta}$  denotes a removal of material similar to the end relief but it ranges across the entire effective width of the gear. In contrast to the crowning, which meant to be addressing random lead errors, the helix angle correction is used to compensate for systematic/predictable lead errors such as deflections resulting from shaft bending.

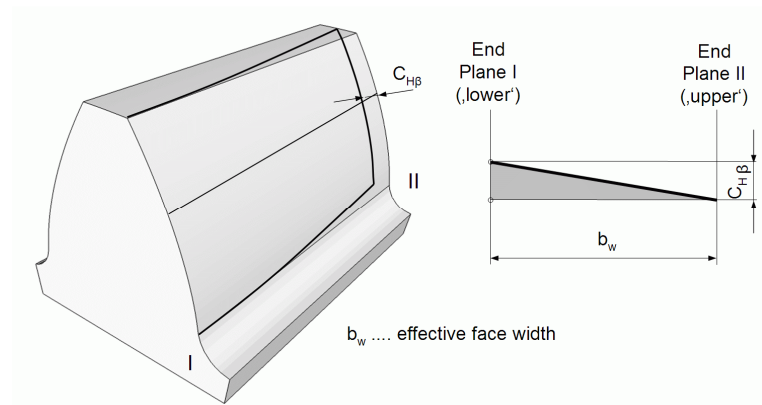


Figure 43: Helix angle correction (source: [5], chapter 4.17.5.4.2.)

## 7. Qualitative Validation

As basis of qualitative validation a model used in conjunction of an engineering project at AVL development is utilized. The aim of the project was to enhance the NVH behaviour of the transmission by applying adequate lead corrections.

The used model represents a manual six gear transmission following a classical two shaft design.

Figure 44 shows the 3D view of the model in EXCITE. The flexible bodies of the model are the input shaft (green), the counter shaft (turquoise), the six gear wheels (blue), the idler shaft (yellow) and the differential (red). The idler shaft is used to realize a reverse gear. Additional rigid bodies are the test bed, the housing and the disc, which represents the clutch disk. The input torque acts on the disc while the brake torque acts on the body "shaft1", which is connected to the differential. On each of the other gear body a drag torque acts to simulate the friction of the mechanical elements.

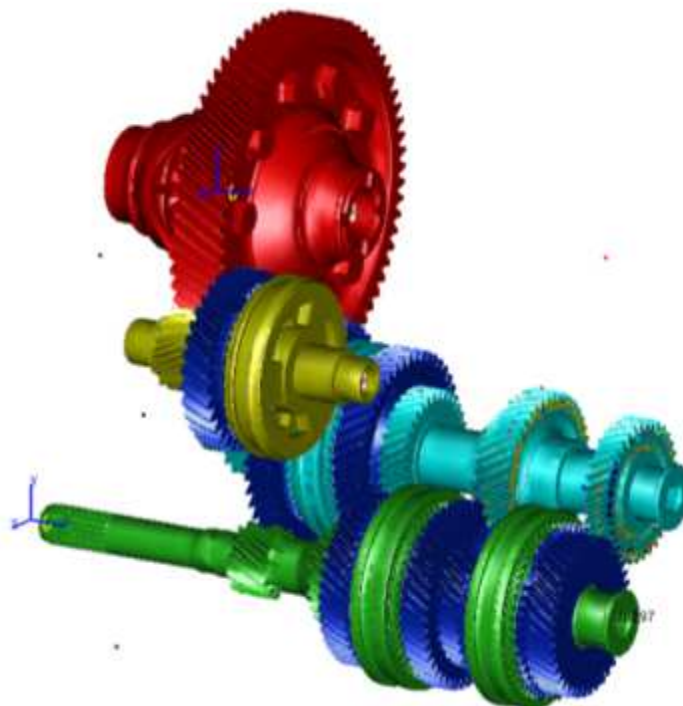


Figure 44: 3D representation of the reference model in EXCITE

Figure 45 shows the 2D view (aka Block Model Editor) of the model in EXCITE. The gear wheels are connected to the input shaft respectively to the counter shaft via a revolute joint (provides radial stiffness/damping), a rotational coupling joint (provides angular stiffness/damping) and an axial thrust bearing joint (provides axial stiffness/damping). The input and counter shaft are connected with the housing via deep groove ball bearing joints (abbr. DGBB) joints. The idler shaft is supported by tapered roller bearing joints (abbr. TRB). The cylindrical gear wheel mesh is realized with detailed gear contact representations (ACYG joints).

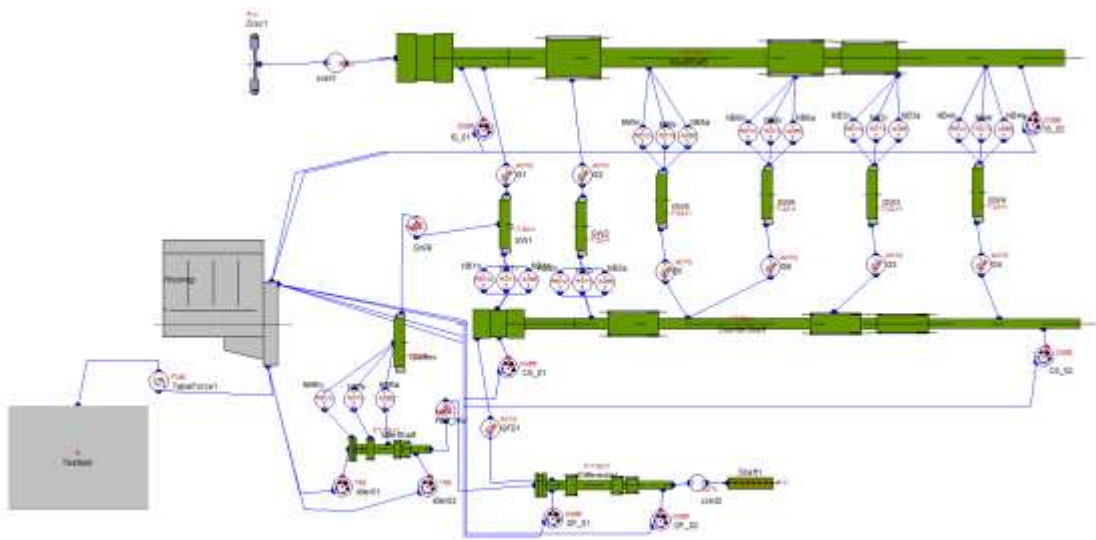


Figure 45: 2D view of the reference model in EXCITE

Micro geometry crowning, barrelling, tip relief and a correction of the helix angle were used, as given by the customer. Contrary to the predictions obtained with a specific tooth contact analysis tool in the early design phase, the results of the EXCITE-simulation showed a significant non uniform meshing force distribution of the contact pattern. Based on this state helix angle corrections necessary to achieve an acceptable face load distribution were obtained by EXCITE. The table 1 shows the helix angle correction values as given by the customer and those resulting from EXCITE.

Gear	1	2	3	4	5	6	Final Drive
Helix angle correction (from Customer)	30	-25	30	-22	7	-17	25
Helix angle correction (from EXCITE)	80	90	-50	-140	-70	-85	25
Pinion (P)/Gear (G)	G	P	G	P	P	P	P

*Table 1: Recommended helix angle correction from EXCITE and Customer (source: [7])*

The helix angle correction, as derived from EXCITE, was significantly higher than the initial values from the customer. Based on this observation doubts has been raised with regard to the correctness of the resolution of angular misalignments in EXCITE. This was one of the main drivers conduct a study or thesis in order to evaluate and assess the result of the ACYG joint with respect to angular misalignments.

## **7.1 Simplified EXCITE model**

In order to investigate the ACYG-joint with respect to angular misalignments, a simplified model has to be derived.

The background of this simplification is actually twofold: Firstly the EXCITE model shall be configured in a way that operational characteristics is as close as possible the quasi-static case, since this the main limitation of the tooth contact analysis tool (KISSsoft) used as a verification reference. Secondly, the focus on a single gear mesh is highly appreciated in terms of computational effort and handling of KISSsoft-models which typically represent only one stage within one model.

In order to select a representative gear stage of the transmission, the absolute angular displacements of the nodes of the countershaft connected to the ACYG-joints are compared. The fourth gear shows the highest angular displacement of the connected nodes and consequently, the highest angular misalignment (figure 46). That is why this specific gear is chosen for the validation.

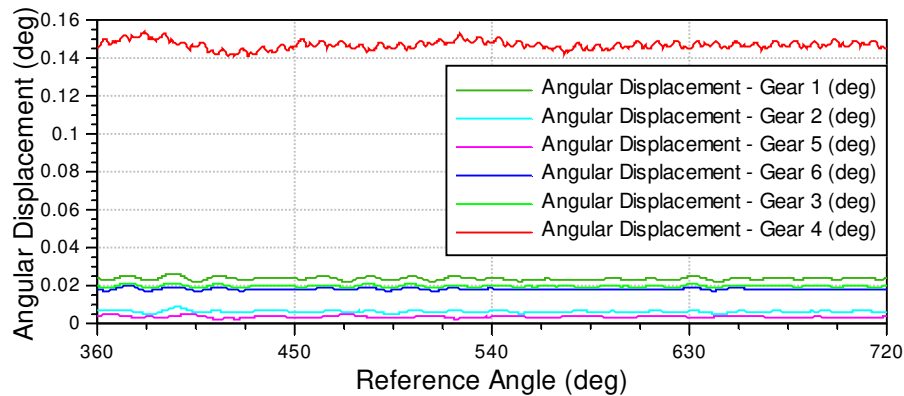


Figure 46: Angular displacement of each gear

To get a simplified model, all other gears and their connected joints are erased. Also the reverse gear including the idler shaft and their joints are deleted. The brake torque which is acting on the body “Shaft1” is moved to the counter shaft by scaling it according to the transmission ratio of the differential. So the shaft, the differential and their joints also can be detached. The input torque which acts on the disk is removed and a constant rotational speed is set for the fourth gear “GW4”. As result the disc and the input shaft are suspended.

To avoid the influence of elastic deformations of the bodies on the joint, the type of the countershaft and the fourth gear “GW4” are set to rigid. By reason that the joints of GW4, which hold it in place, are erased, its translatoric degrees of freedom have to be locked accordingly. The same procedure is applied to the countershaft except the angular degree of freedom about the first axis which agrees to the axis of main rotation. The angular misalignments, as they are computed with the reference model, are set as constant angular displacement to the rigid bodies in order to preserve the impact of the angular misalignment on the results of the ACYG joint. Figure 47 shows the model after the simplification as visualised in the 2D view in EXCITE.

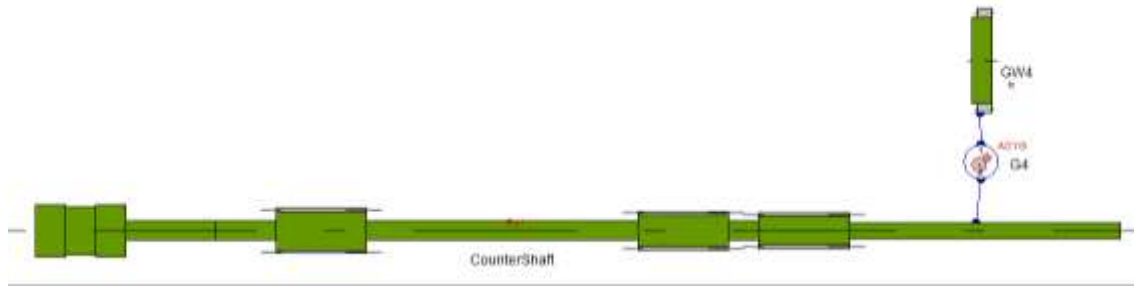


Figure 47: Simplified model

### 7.1.1 Gear data of the simplified EXCITE model

In the following figure the gear data of the fourth gear, as set in the simplified and in the reference model is visualized. The first value refers to the pinion and the second to the gear.

Check And Generate Profiles (for Zero Backlash Conditions)

Check Data

Generate Profiles

**Info**

```

Theoretical Pitch Circle (T.P.C) Diam. d_p = 83.4654304985 /73.0322516862
Base Circle Diameter ..... d_b = 77.828665029 /68.1000819004
Outside (Tip) Circle Diameter ..... d_a = 87.35 /77.6
Active Tip Diameter ..... d_Na = 86.95 /77.2
Root Circle Diameter ..... d_f = 75.5 /65.75
Active Root Diameter..... d_Nf = 78.881 /68.895
Operating Pitch Circle Diam. (O.P.C) d_w = 82.1333333333 /71.8666666667
Helix Direction ..... beta = rightHand /leftHand
Addendum Modification Coefficient ..... x = -0.4787 /-0.1949
Generating Add. Mod. Coefficient ..... x_E = -0.52354265626 /-0.23974265626
Radius of curvature at O.P.C ..... roh_C = 26.2408716366 /22.9607626821
Normal Module..... m_n = 1.75
Transverse Module ..... m_t = 2.08663576246
Transverse Pressure Angle ..... alpha_t = 21.177479665
Operating Normal Pressure Angle ..... alpha_wn = 15.7891990562
Helix Angle at Pitch Cylinder ..... beta = 33.0
Helix Angle at Base Cylinder ..... beta_b = 31.1970188477
Transverse Contact Ratio (nominal) ... eps_alpha = 2.26251610001
Overlap Ratio (nominal) ..... eps_beta = 1.39681842765
Total Contact Ratio (nominal) ..... eps_gamma = 3.65933452765
Zero center distance (for x_1=x_2=0) ..... a_d = 78.2488410924
Sum of profile shift for nom. center dist. x1+x2 = -0.673545811643
Sum of given profile shift ..... x1+x2 = -0.6736
Normal Backlash ..... j_n = 0.097
          
```

Figure 48: Gear data of the reference and the simplified model

The number of teeth is 40 for the pinion and 35 for the gear. Further an active gear width of 14.1mm, a Young's modulus of 210000 N/mm<sup>2</sup>, a Poisson ratio of 0.31, a constant contact damping of 1.2Ns/mm and a coulomb friction coefficient of 0.02 are used. Depending on the used model the contact stiffness is whether constant (3 · 10<sup>8</sup> N/m) or computed by using the Petersen modified Hertz theory. If tooth bending and tilting according to Weber/Banaschek is active or inactive depends on the individual investigation. Generally, no profile or lead modifications are used because they would distort the results. Three nodes are connected to the joint in order to render angular shaft's angular misalignments. For each node ten discretization slices are set, which results in 30 slices in total.

For the validation, besides a helical model, a spur model is used. The gear data of the spur model is listed in the figure 49.

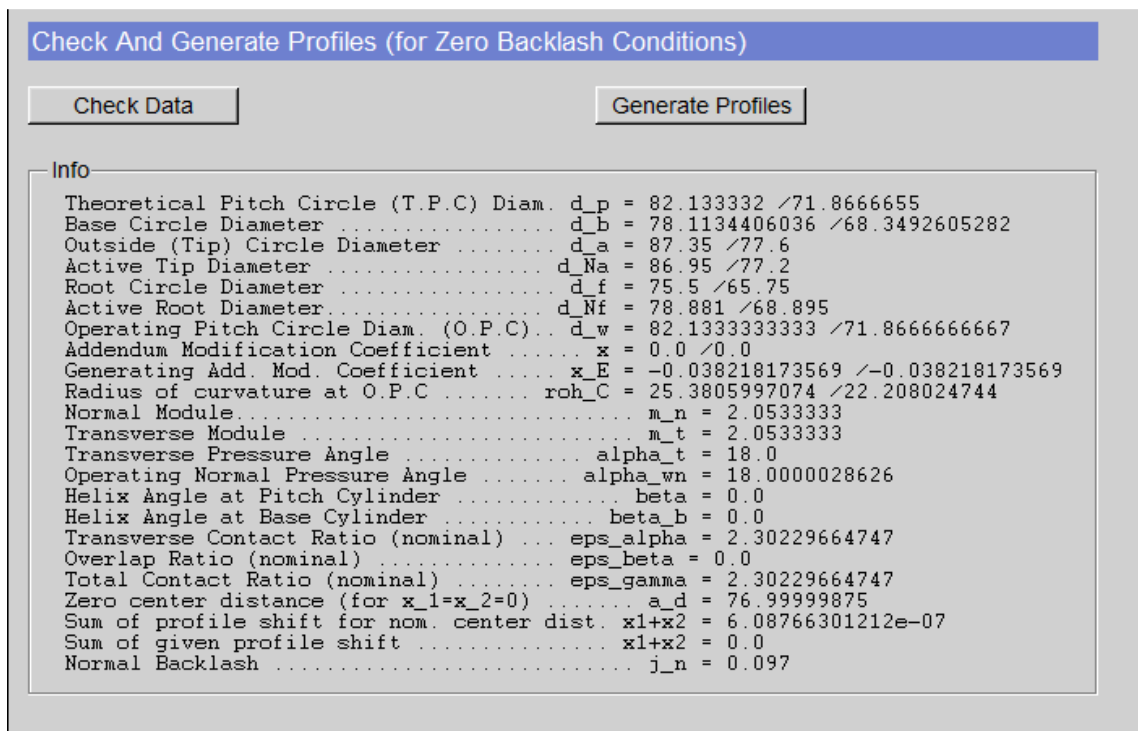


Figure 49: Spur gear data of reference and simplified model

### 7.1.2 Global coordinate system

The position and the orientation of bodies can be defined depending on the global coordinate system, another body or a user defined coordinate system. The simplified model uses the global coordinate system. The body “GW4”, which represents the pinion of the ACYG joint, is placed in the origin of the global coordinate system with X-axis as rotation axis as shown by figure 50. The gear, which is represented by the body countershaft, is located with an offset about the nominal center distance in the direction of the Y-axis. As result the joint coordinate system, as defined in chapter 3, is congruent with the global coordinate system.

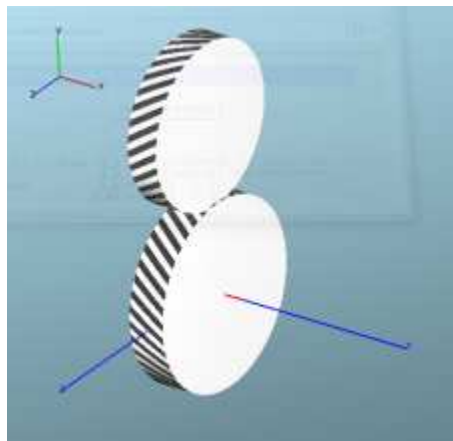


Figure 50: Positioning of the ACYG joint based on the global coordinate system

## 7.2 KISSsoft model

In KISSsoft the cylindrical gear module is used for the investigation. The gear as well as the material properties are defined as in EXCITE. Additionally the active root and tip diameter are compared with EXCITE to ensure that the tooth forms matches with respect of the profile length of the formed involute. With the contact analysis enabled, the axis alignment can be set. The number of slices is set to 30 either.

### 7.3 Compared quantities and expected result values

The comparison between the results of EXCITE and KISSsoft occurs on the basis of the meshing stiffness (figure 52), the mesh deformation (figure 53) and the normal force per unit length (figure 111) depending on the reference rotation angle of the pinion. The results in KISSsoft are calculated only for one pitch, while EXCITE provides results for as many revolutions of the reference body as defined by the user. Additionally, the engagement field plot (figure 112 and figure 113) is used to compare the results quantitatively. The meshing stiffness and the mesh deformation are total values of the gear mesh measured at the pitch point and in the direction of the plane of action (see figure 51).

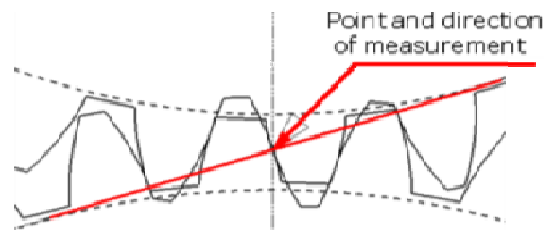


Figure 51: Point and direction of the measurement of meshing stiffness and deformation

The meshing stiffness, as shown in figure 52, depends on the active face width, the stiffness calculation method respectively the deformation method and the number of flank pairs in interaction. Meshing stiffness rises with the number of flank pairs in interaction. For spur models with a constant meshing stiffness and no angular misalignments the expected result can be computed by multiplying the constant meshing stiffness ( $3 \cdot 10^8 \text{ N/m}$ ) with the number of flank pairs in contact. The expected results are  $600 \text{ kN/mm}$  for two and  $900 \text{ kN/mm}$  for three flank pairs in action.

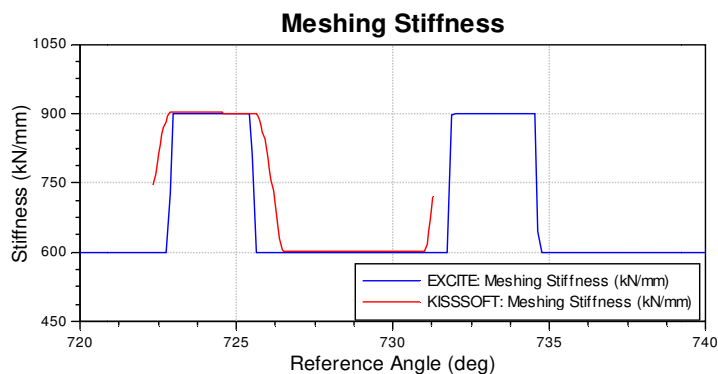


Figure 52: Result quantity: Meshing stiffness

The normal mesh deformation, as shown in figure 53, has the same dependencies as the meshing stiffness but reacts reciprocal on an increase of the number of flank pairs in action. To compute the expected value the total normal force of 7595 N is divided by the stiffness, which amounts to 12.66 micron for two and 8.438 micron for three flank pairs in contact. These values are only true for spur models without angular misalignments with the contact lines extended throughout the whole active gear width.

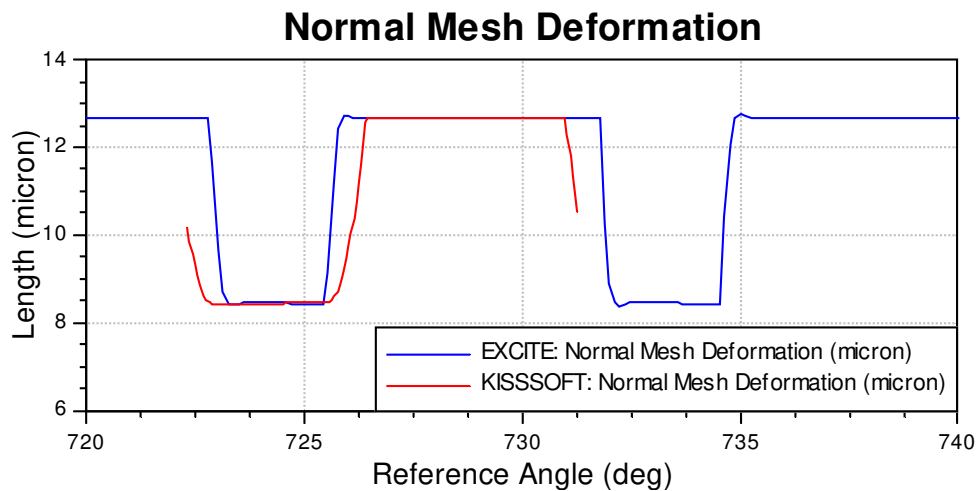


Figure 53: Result quantity: Normal mesh deformation

The quantity of the normal force per unit length (often also referred to “as load intensity” or “line load”) is computed from the results of the engagement field plot and therefore within the extend of one pitch. The expected value can be computed from the total normal force 7595 *N* of the spur gear mesh divided by the active face width of 14.1*mm* and the number of flank pairs in contact. Thus values of 269 *N/m* for two and 179 *N/m* for three flank pairs in action are expected. These values are valid for models with angular misalignment too. But since the quantity is averaged over all slices in direction of the gear width and the width of each slice along the gear width may vary, the result can differ from KISSsoft with respect to angular misalignment.

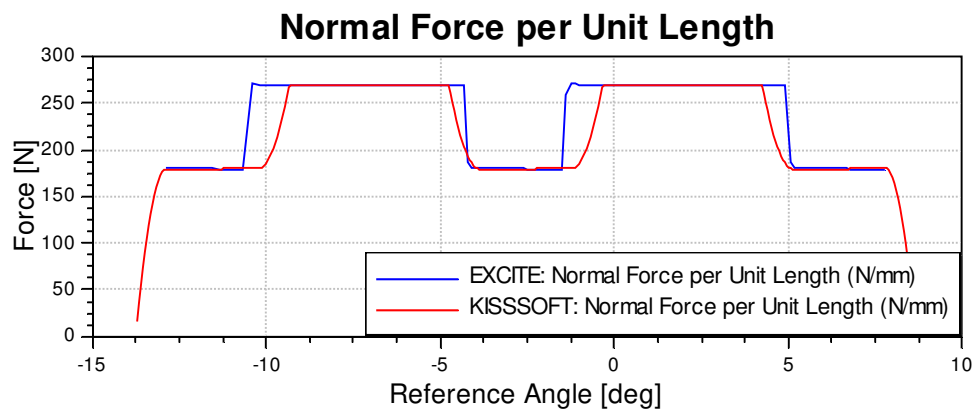


Figure 54: Result quantity: Normal force per unit length

The engagement field plot shows the normal force per unit length of one tooth for one pitch. The abscissa is the roll distance which corresponds to the engagement length of the tooth and the ordinate is the active gear width. Only a 2D representation (in the form of a fringe plot) is available in EXCITE (figure 56), while a 3D representation is available in KISSsoft (figure 55). Therefore, a view from the top is used to convert into a 2D result (figure 57).

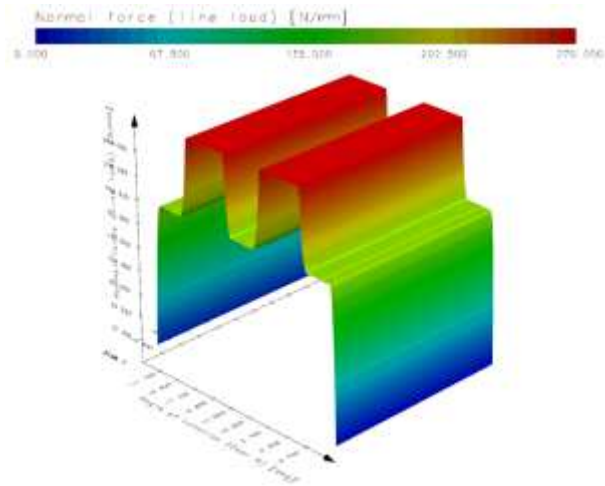


Figure 55: Result quantity: Engagement field plot (3D) in KISSsoft

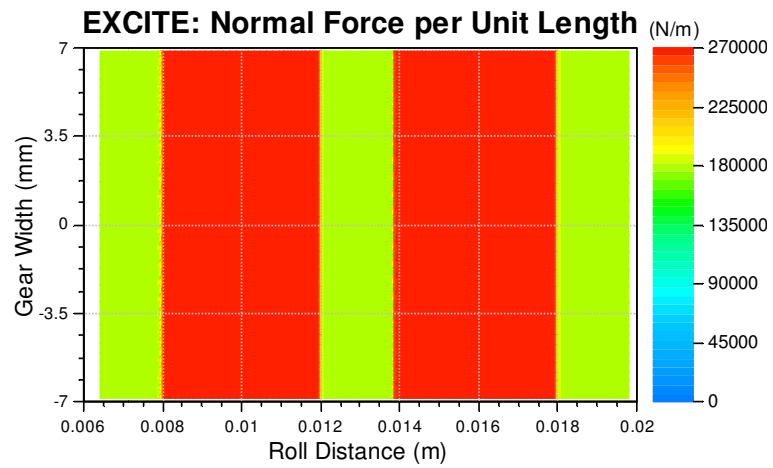


Figure 56: Result quantity: Engagement field plot (2D) in EXCITE

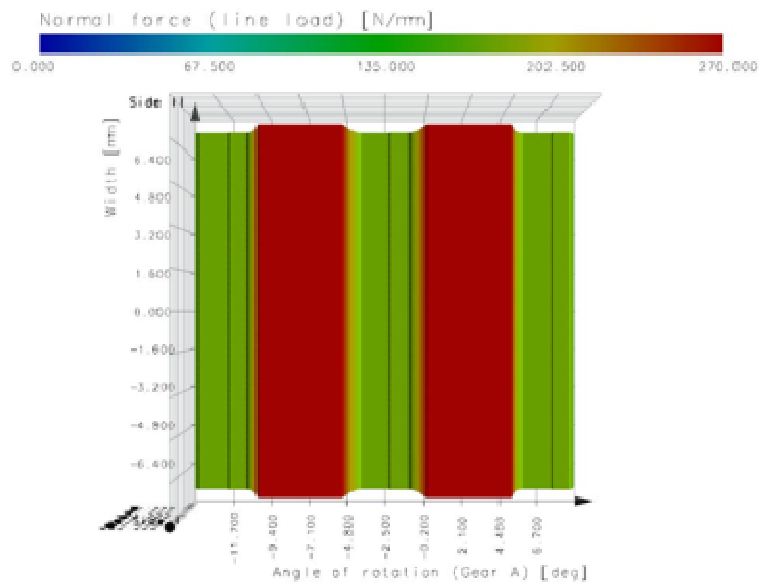


Figure 57: Result quantity: Engagement field plot (2D) in KISSsoft

## 7.4 Influence of the inertia tensor of the body

Since EXCITE is a multi-body dynamics software, it has to be ensured that these dynamics play a minor role on the results only. Therefore, two models with a high and a low inertia tensor are compared with KISSsoft. The figure 58 and figure 59 show the curves of the normal force per unit length of one flank pair as computed by EXCITE and KISSsoft depending on the reference angle. The reference angle is time equivalent and corresponds to the angular position of the body “GW4”. Due to the change of the number of flank pairs in contact, which changes here between two and three here, the normal force per unit length alters between 270 N/mm and 180 N/mm. The figures also show that a higher inertia tensor results in an inert reaction of the normal force during the change of the number of flank pairs in contact. With the lower inertia tensor, local peaks arise during the change of the number of flank pairs in contact. But these peaks remain within an acceptable magnitude. Therefore the inertia tensor of the countershaft is set from the initial value ( $2.88 \cdot 10^{-2} \text{ kgm}^2$ ), which is given by the reference model, to  $2.88 \cdot 10^{-6} \text{ kgm}^2$ .

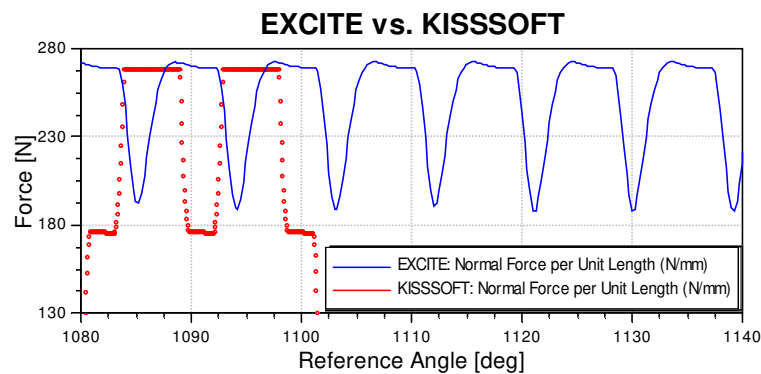


Figure 58: Normal force per unit length ( $I_{xx \text{ Countershaft}} = 2.88 \cdot 10^{-2} \text{ kgm}^2$ )

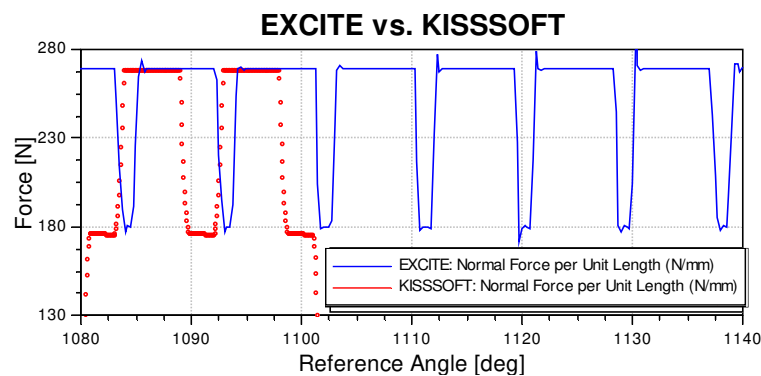


Figure 59: Normal force per unit length ( $I_{xx \text{ Countershaft}} = 2.88 \cdot 10^{-6} \text{ kgm}^2$ )

## 7.5 Description of the Investigated models

In the following the investigated models are listed and described:

- Model A

This model has spur gearing, a linear meshing stiffness and no angular misalignment. The results give an indication if the general computation of forces, stiffness and mesh deformation differs from KISSsoft.

- Model B

This model has spur gearing, a linear meshing stiffness and an applied skew misalignment. With this model the impact of the skew misalignment on the deformation and stiffness is compared to KISSsoft. The skew value of 7.92 micron is set by an angular displacement of the countershaft of 0.03224 degree about the second global axis.

- Model C

It has a spur gearing, a linear meshing stiffness and a skew misalignment of 50 micron. This model is equivalent with the last model but the amount of skew is raised to 50 micron.

- Model D

This model has a spur gearing, a linear meshing stiffness and an applied slope misalignment. Model D is used to evaluate the impact of slope misalignment on the contact pattern. The slope misalignment of 38.5 micron is achieved by an angular offset of the countershaft of 0.1567 degree about the third global axis.

- Model E

It has a spur gearing, a linear meshing stiffness and a combined slope and skew misalignment. This model superimposes the angular misalignments of the slope and skew models.

- Model F

Helical gearing, a linear meshing stiffness but no angular misalignments are applied to this model. The helical model is used to verify the assumptions about helical gearing in EXCITE.

- Model G

This model has helical gearing, a linear meshing stiffness and an applied slope misalignment. The same amount of slope misalignment as by the spur gearing model is applied to the helical model.

- Model H

Spur Gearing, the deformation is calculated according to Weber/Banaschek and no angular misalignments are the properties of this model. With this model the implemented approach according to Weber/Banaschek is compared with KISSsoft.

- Model I

This model has spur gearing, the deformation is computed according to Weber/Banaschek, no angular misalignment and root circle diameter equals the base circle diameter. Within this model, the gear data is modified in such a way that the root circle diameter matches the base circle diameter. The reason for that is that in EXCITE parts of the profile below the base circle diameter are not included in the deformation computation according to Weber/Banaschek. The same modification of the gear data is applied in KISSsoft.

- Model J

Additional to the last model, the torque, which is lasting on the countershaft, is set to 2 Nm to investigate the variation of the load on the computation of the deformation according to Weber/Banaschek.

## 7.6 Results

In the following, the results of the models are outlined.

### 7.6.1 Model A

The comparison between EXCITE and KISSsoft shows conformity of the meshing stiffness (figure 60), the normal mesh deformation (figure 61) and the normal force per unit length (figure 62) for two and three flank pairs in action. Nevertheless, during the change of the number of flanks in contact EXCITE differs from KISSsoft, which may result from the consideration of contacts out of the plane of action by KISSsoft. All results fit with the expected values for two and three flank pairs in action.

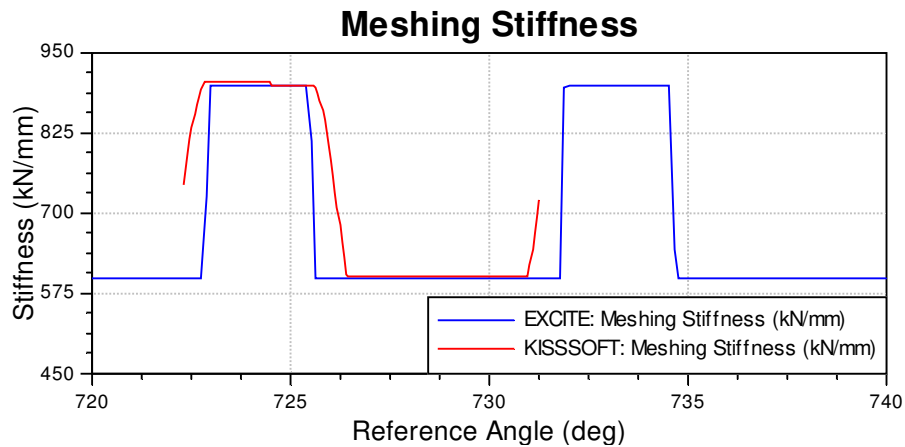


Figure 60: Model A - Meshing stiffness

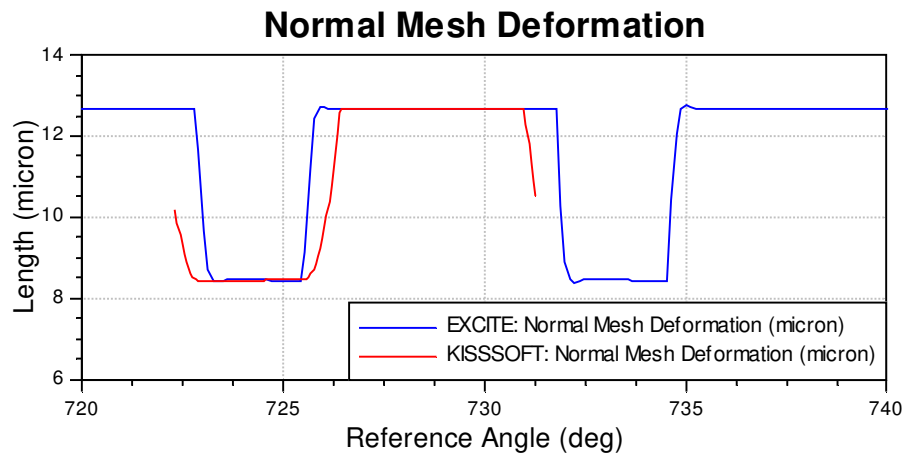


Figure 61: Model A - Normal mesh deformation

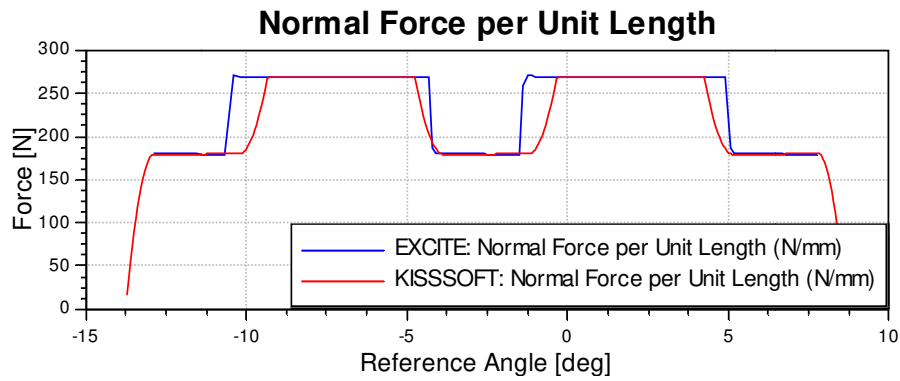


Figure 62: Model A - Normal force per unit length

The engagement field plots (figure 63 and figure 64) indicate that the results of normal force per unit length are quantitatively identical.

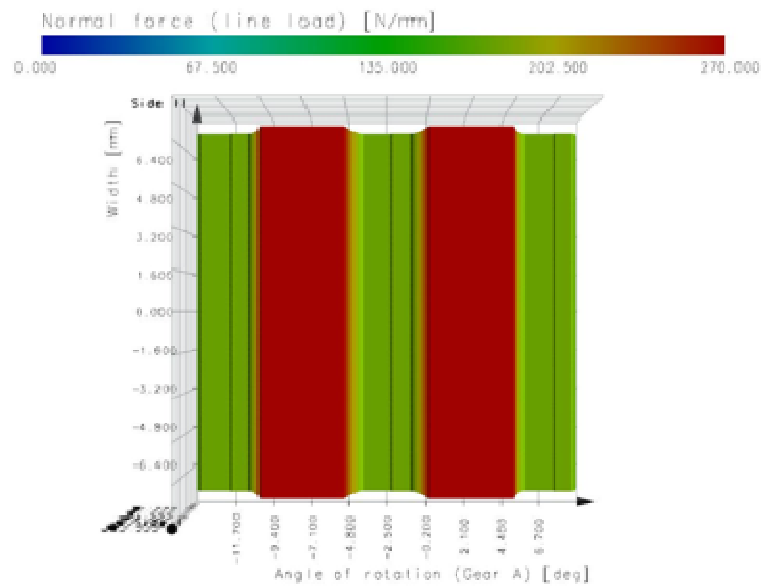


Figure 63: Model A - Engagement field plot from KISSsoft

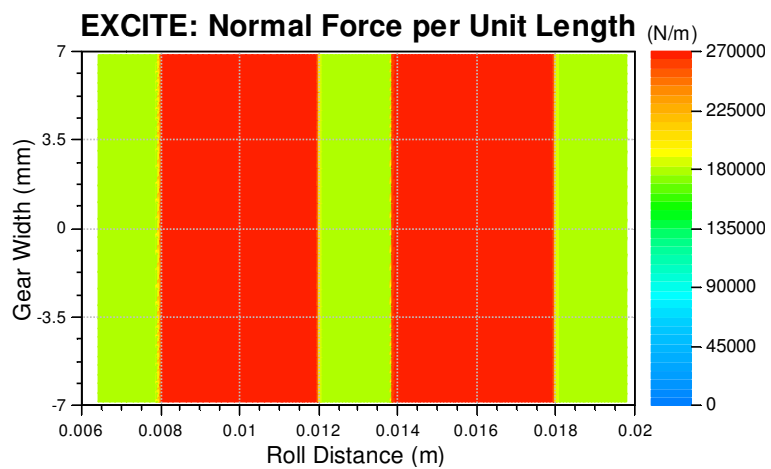


Figure 64: Model A - Engagement field plot from EXCITE

## 7.6.2 Model B

The results of EXCITE show, especially when it comes to the meshing stiffness (figure 65), local peaks after the change of the number of flanks in contact. These take place when the contact of the third tooth occurs during two time steps of the solver. It leads to an overlapping of the tooth surfaces in the next time step, which in turn leads to an increase in the calculated stiffness. Apart from this effect, the results of the meshing stiffness and the normal mesh deformation (figure 66) agree with a deviation of less than two percent. The normal force per unit length (figure 67) matches with the expected values.

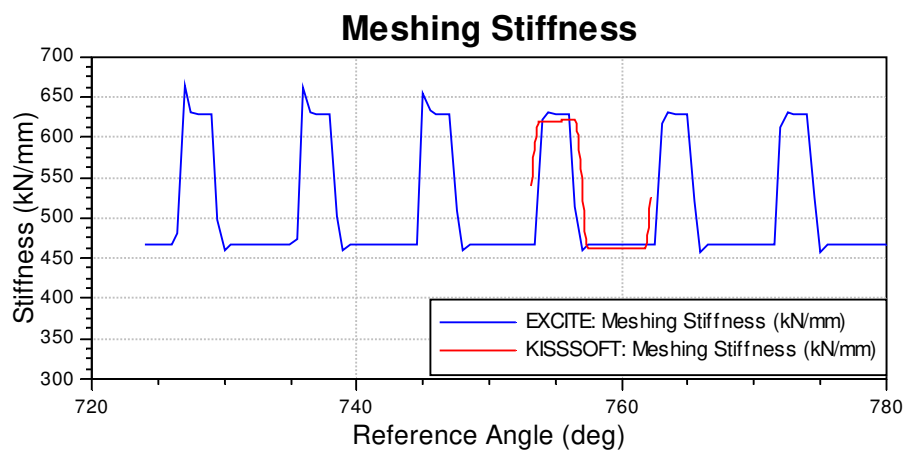


Figure 65: Model B - Meshing stiffness

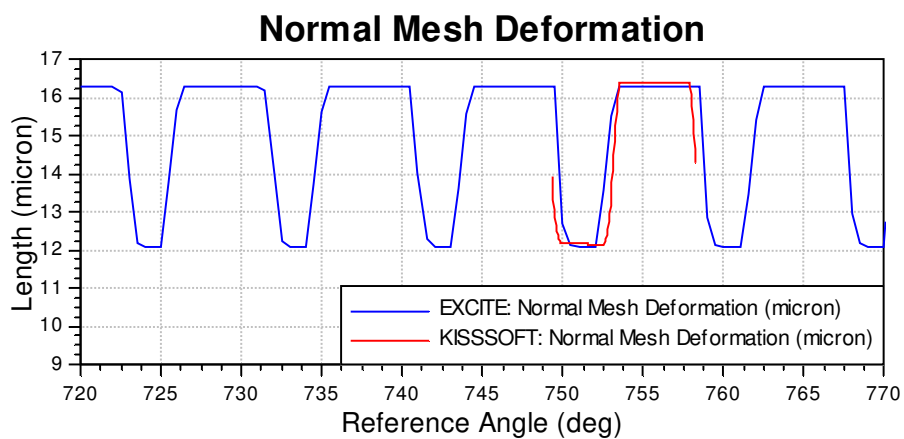


Figure 66: Model B - Normal mesh deformation

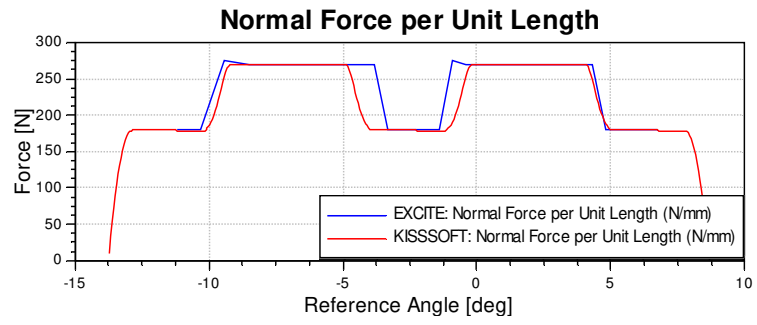


Figure 67: Model B - Normal force per unit length

The distribution of the normal force per unit length over the active width shows consistency (figure 68 and figure 69).

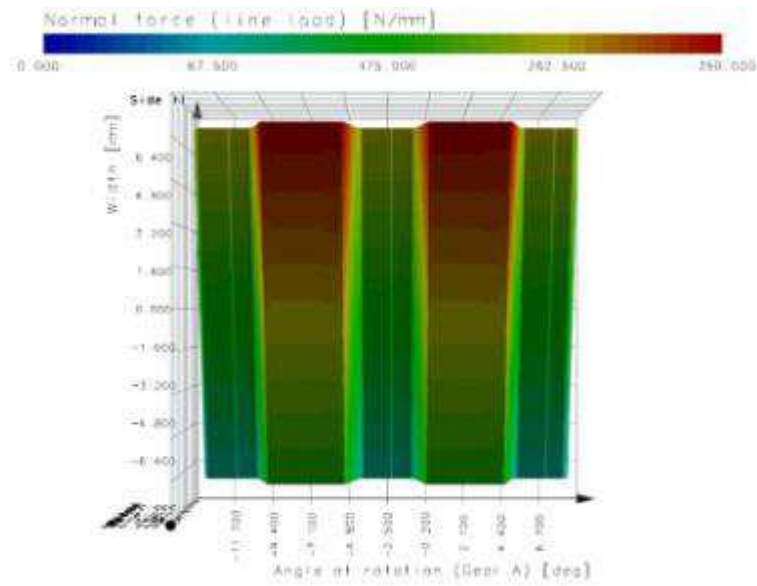


Figure 68: Model B - Engagement field plot from KISSsoft

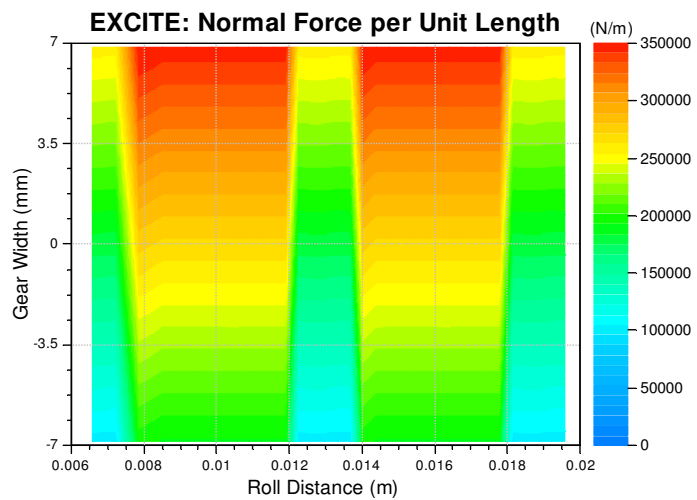


Figure 69: Model B - Engagement field plot from EXCITE

### 7.6.3 Model C

With the higher skew misalignment of 50 micron, the deviation of the meshing stiffness (figure 70) and the normal mesh deformation (figure 71) rises up to four percent which is still within acceptable range. Nevertheless, a slope misalignment of 50 micron with respect to the common gear width of 14.1 mm does typically not occur in a real gear mesh. The result for the normal force per unit length results (figure 72) differs between EXCITE and KISSsoft but with 270 N/m for two flank pairs in action it still reasonable fits to the expected value.

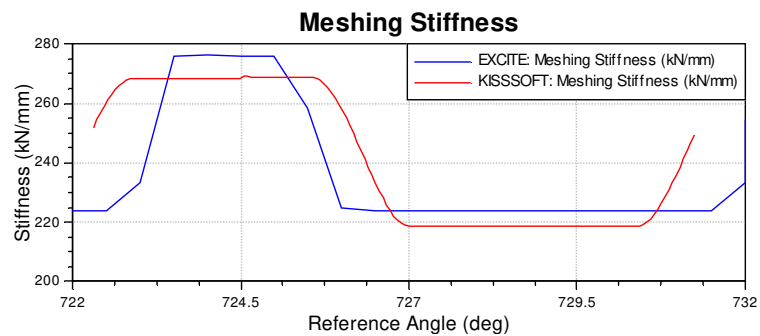


Figure 70: Model C - Meshing stiffness

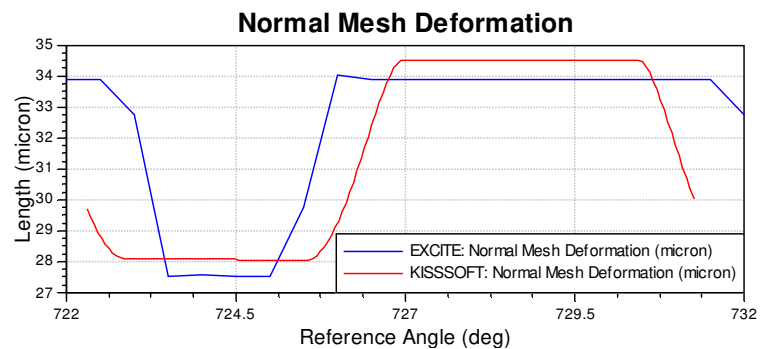


Figure 71: Model C - Normal mesh deformation

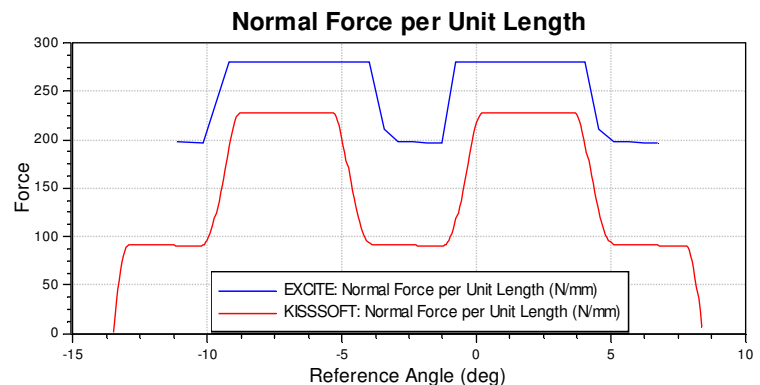


Figure 72: Model C - Normal force per unit length

The engagement field plots are optically consistent (figure 73 and figure 74). It can clearly be seen that only half of the gear width is in contact, which is a consequence of the exaggerated skew value.

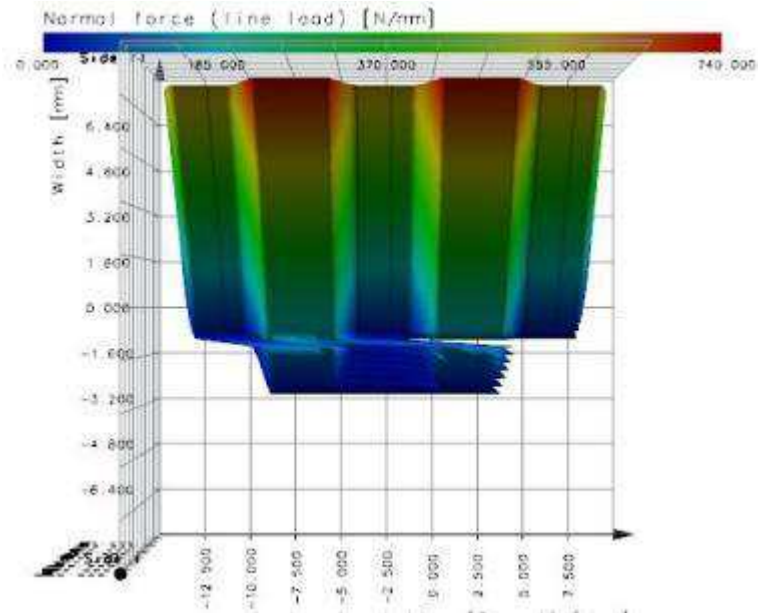


Figure 73: Model C - Engagement field plot from KISSsoft

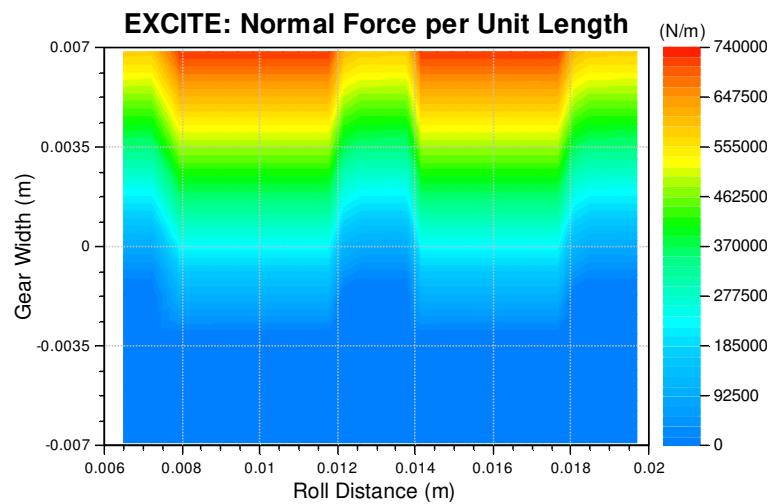


Figure 74: : Model C - Engagement field plot from EXCITE

### 7.6.4 Model D

The meshing stiffness result in EXCITE is one-third of the result in KISSsoft and the normal mesh deformation (figure 76) is three times higher. The normal force per unit length in KISSsoft meets the expected value (figure 77). The force calculated in EXCITE is continuously higher.

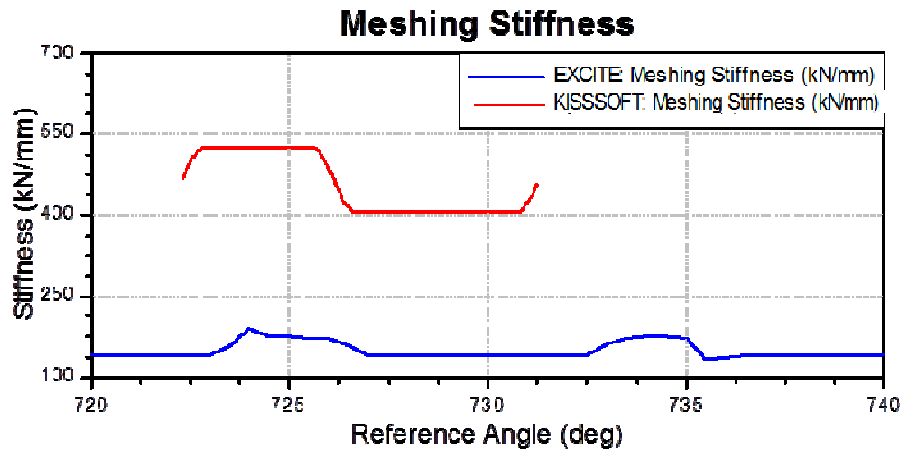


Figure 75: Model D - Meshing stiffness

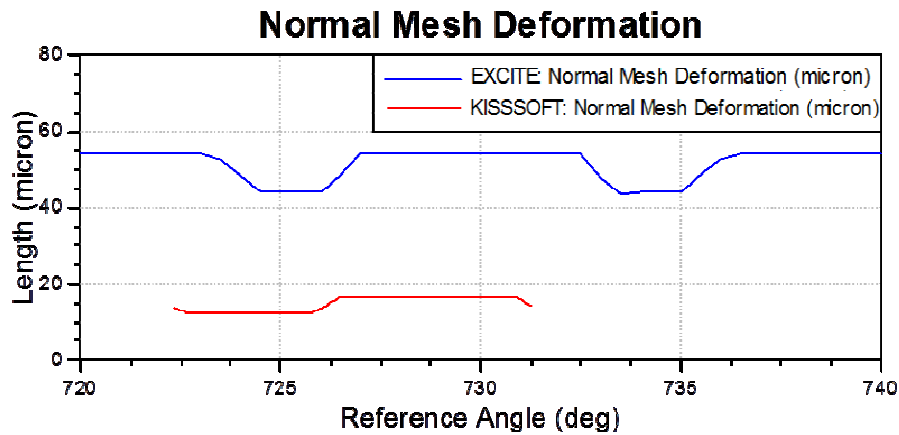


Figure 76: Model D - Normal mesh deformation

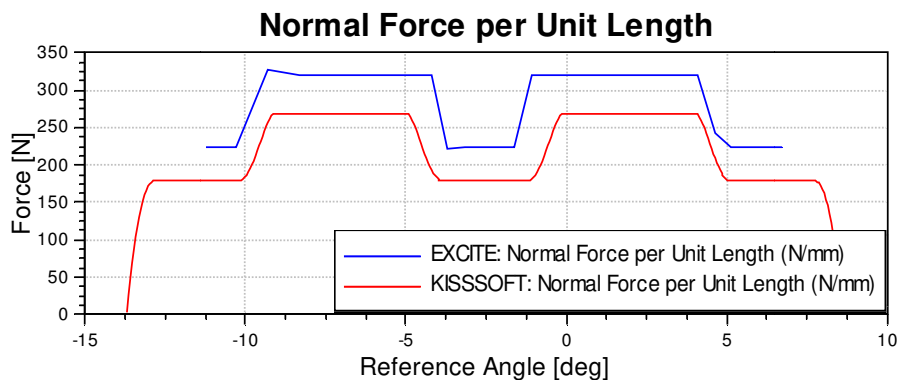


Figure 77: Model D - Normal force per unit length

The engagement field plot results differ significantly (figure 78 and figure 79). Where the supporting gear width is about 6 mm in EXCITE, it is the whole gear width in KISSsoft.

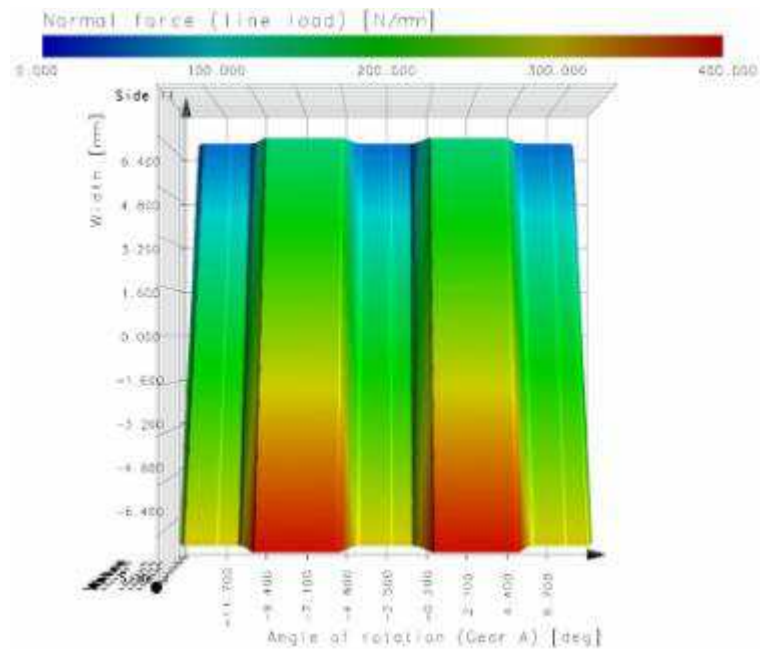


Figure 78: Model D - Engagement field plot from KISSsoft

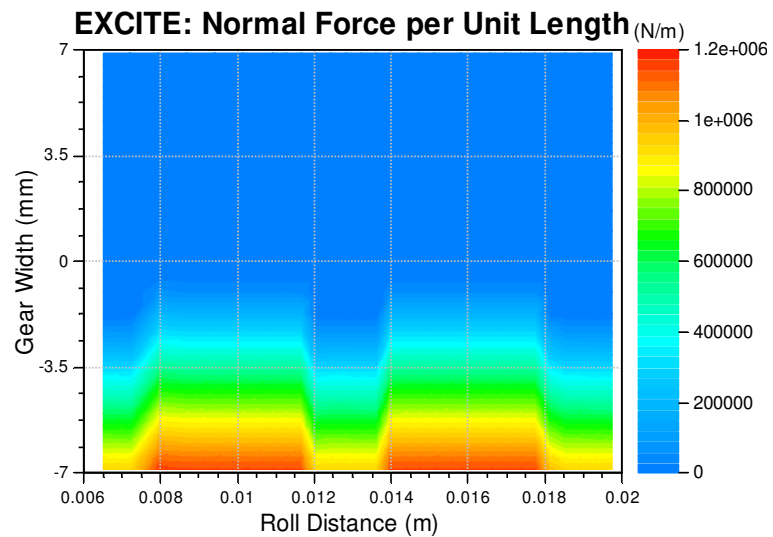


Figure 79: Model D - Engagement field plot from EXCITE

It can be concluded that this model, which manily represents slope type angular misalignments, shows significant differences with respect to the calculation reference.

### 7.6.5 Model E

The superimposing of skew and slope misalignments show the expected continuous divergence between KISSsoft and EXCITE for all compared results (figure 80 - figure 82).

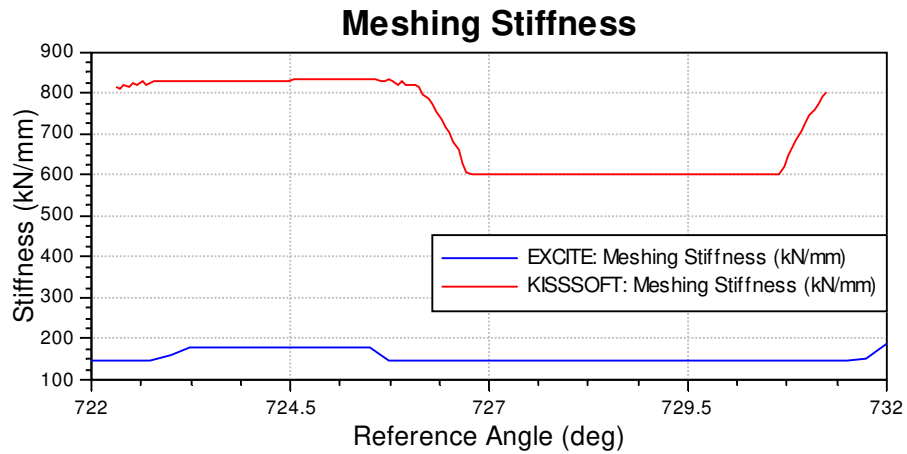


Figure 80: Model E - Meshing stiffness

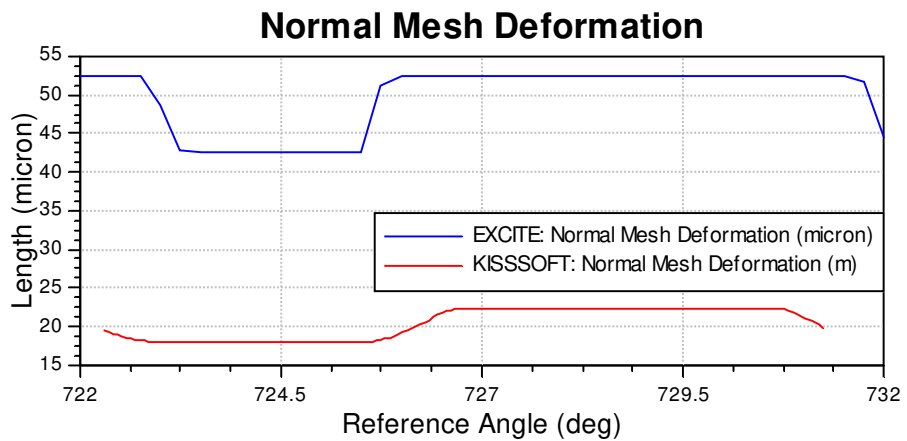


Figure 81: Model E - Normal mesh deformation

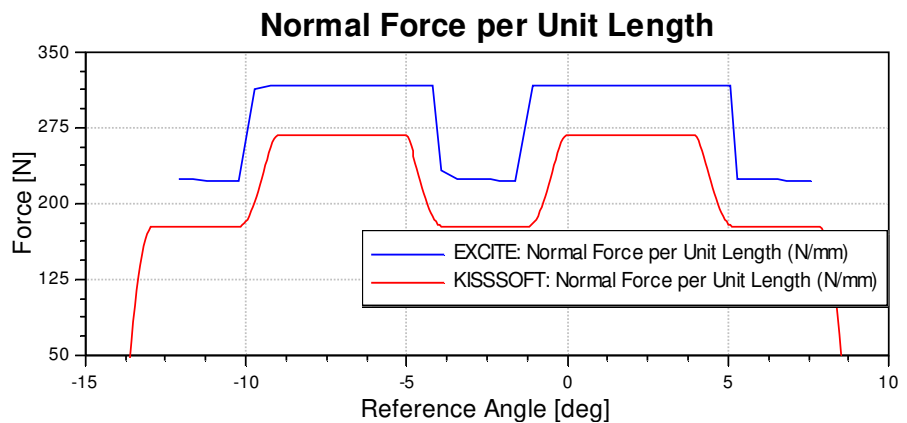


Figure 82: Model E - Normal force per unit length

The comparison of the figure 83 and figure 84 shows the difference between EXCITE and KISSsoft. The supporting gear width is 6mm in EXCITE and the whole gear width in KISSsoft .

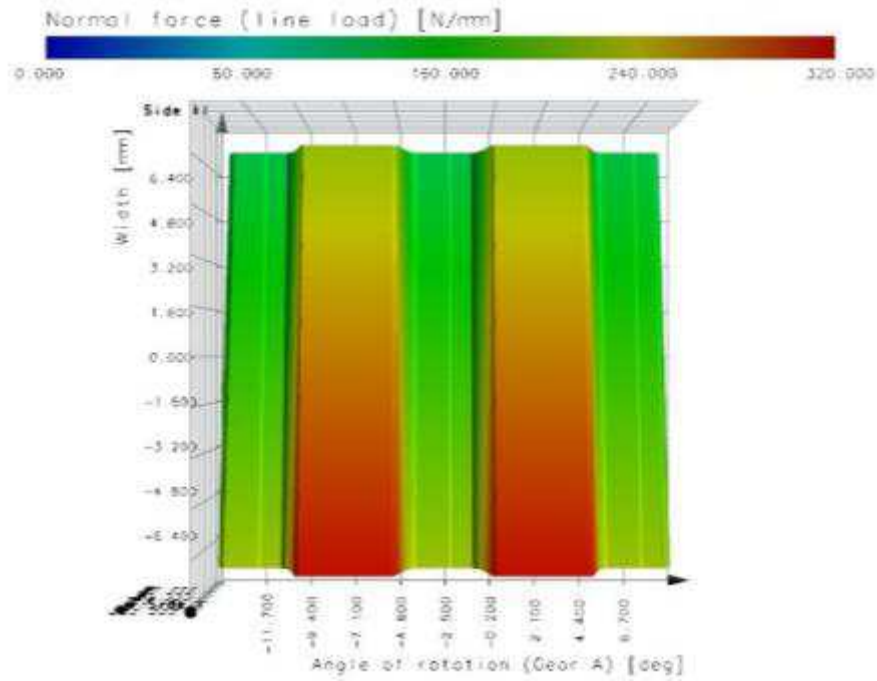


Figure 83: Model E - Engagement field plot from KISSsoft

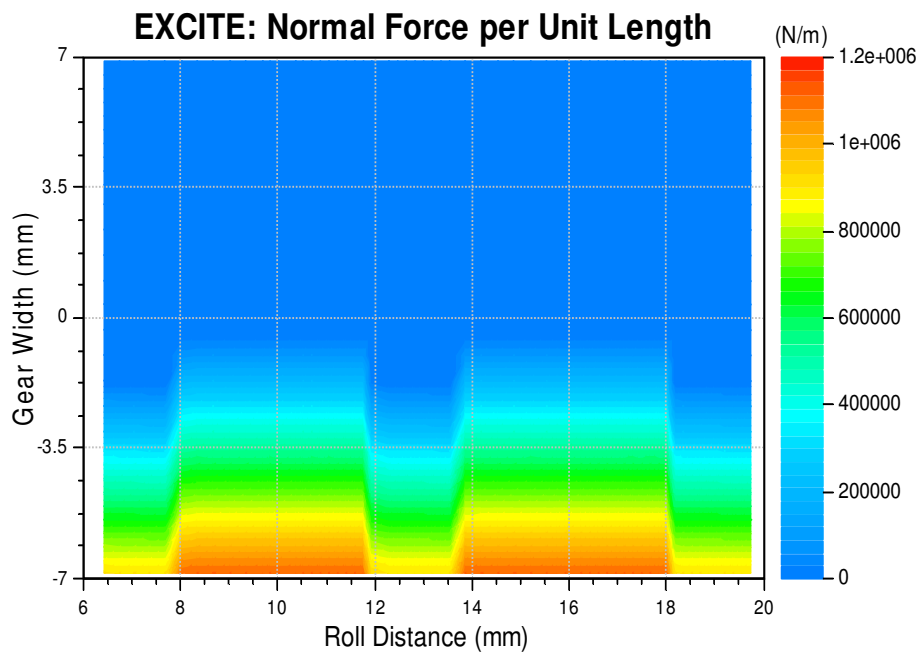


Figure 84: Model E - Engagement field plot from EXCITE

### 7.6.6 Model F

The meshing stiffness (figure 85) and normal mesh deformation (figure 86) results in EXCITE differ from those in KISSsoft. Since the meshing stiffness and the normal mesh deformation in EXCITE are given for the equivalent spur gear they have to be recalculated. Nevertheless, EXCITE deviates from KISSsoft within eight percent for the meshing stiffness and seven percent of the normal mesh deformation.

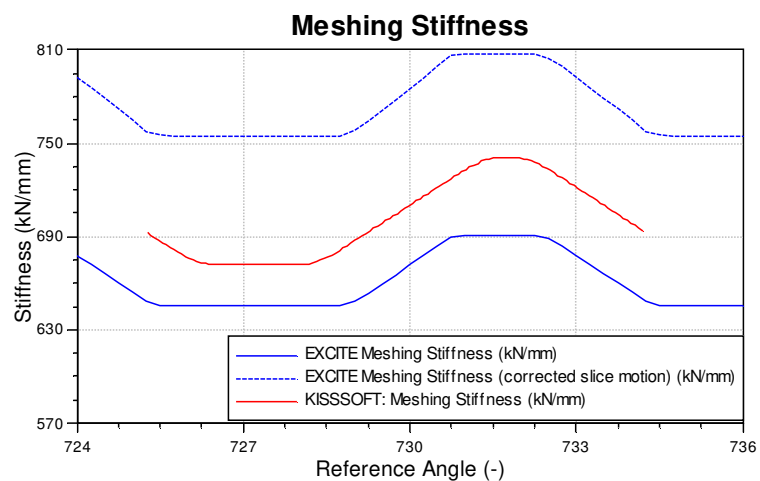


Figure 85: Model F - Meshing stiffness

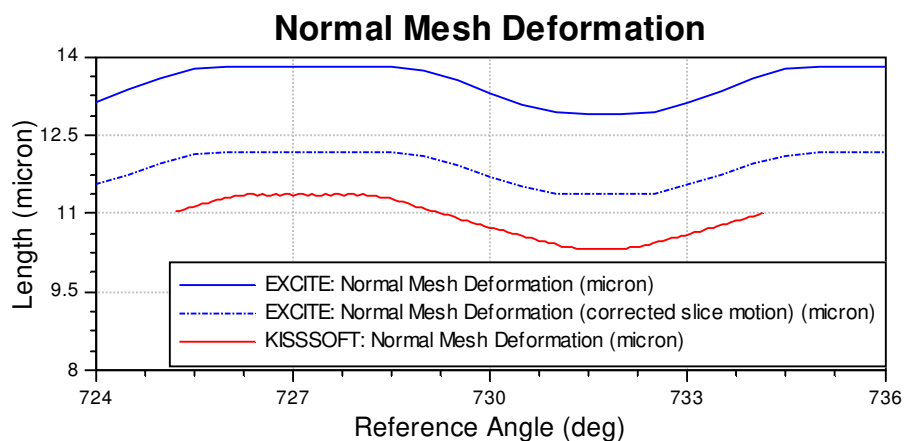


Figure 86: Model F - Normal mesh deformation

The normal force per unit length in KISSsoft is calculated in the direction of the normal cut, where the EXCITE result uses the face cut of the gear (figure 87). That is the reason why it delivers another result and cannot be used for the comparison.

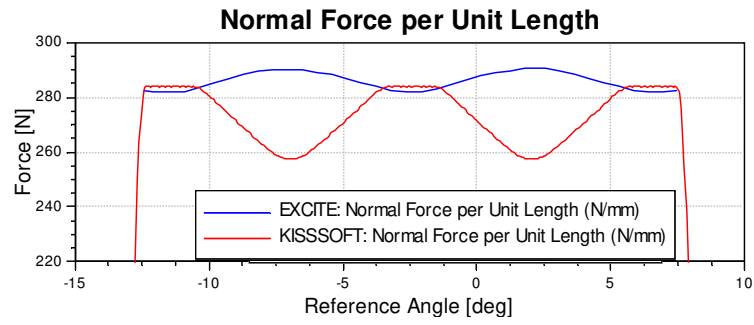


Figure 87: Model F - Normal force per unit length

Nevertheless, the engagement field plots agree with respect to the distribution, the maxima and minima of the normal force per unit length (figure 88 and figure 89).

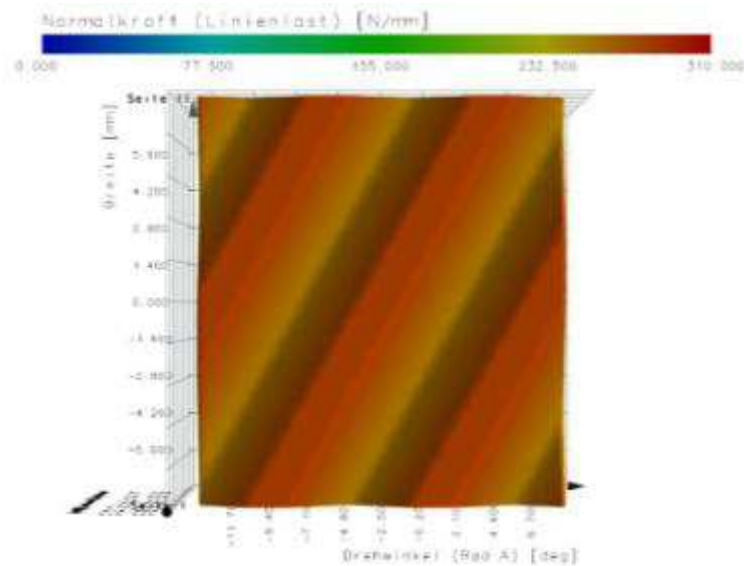


Figure 88: Model F - Engagement field plot from KISSsoft

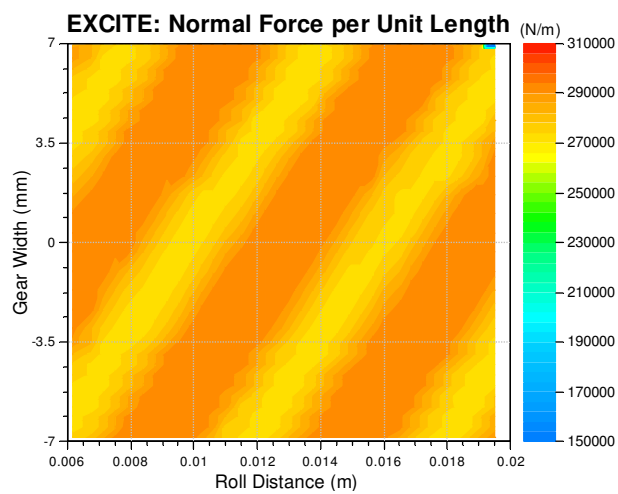


Figure 89: Model F - Engagement field plot from EXCITE

### 7.6.7 Model G

The applied slope misalignment on the helical model leads to similar deviation in the results as in the spur model with slope misalignment, as it can be seen in the meshing stiffness (figure 90) and the normal mesh deformation (figure 91). As already mentioned in model F, the normal force per unit length is not suitable for a comparison of helical models (figure 92).

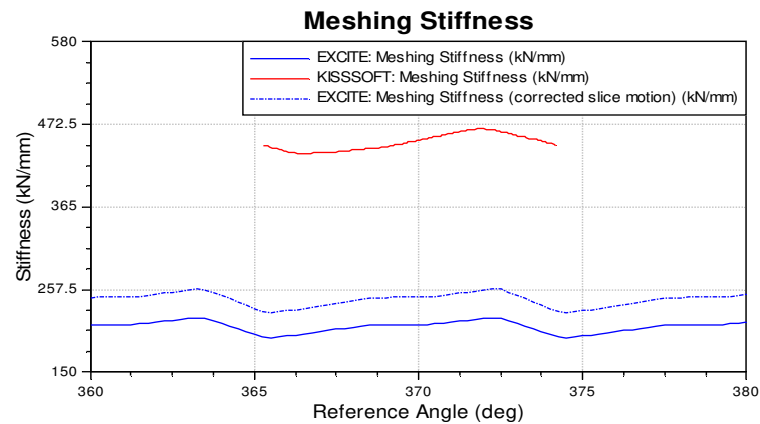


Figure 90: Model G - Meshing stiffness

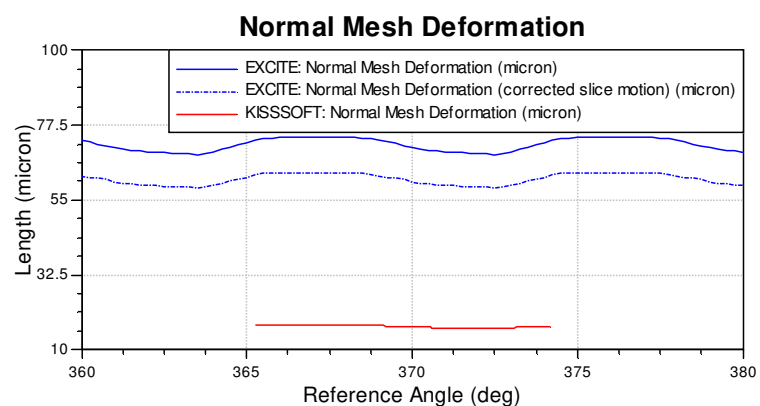


Figure 91: Model G - Normal mesh deformation

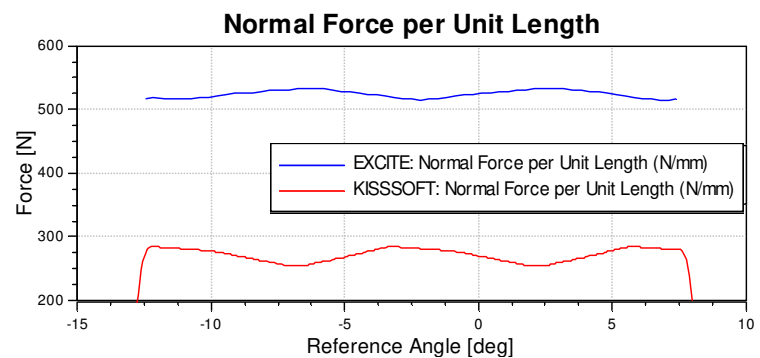


Figure 92: Model G - Normal force per unit length

Where the supporting gear width is in EXCITE 6 mm, it is in KISSsoft the whole 14.1 mm, as it is shown by figure 93 and figure 94.

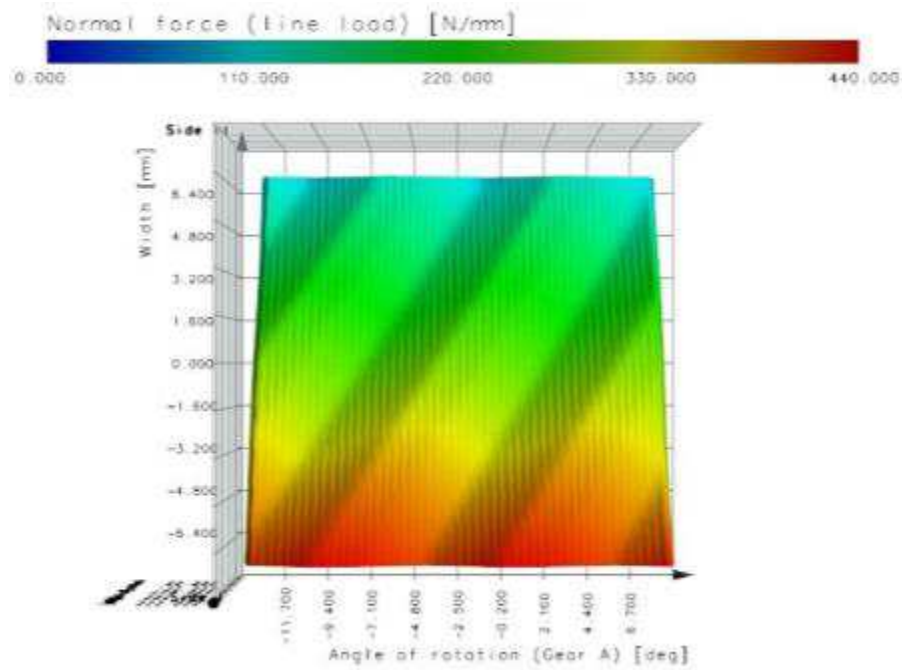


Figure 93: Model G - Engagement field plot from KISSsoft

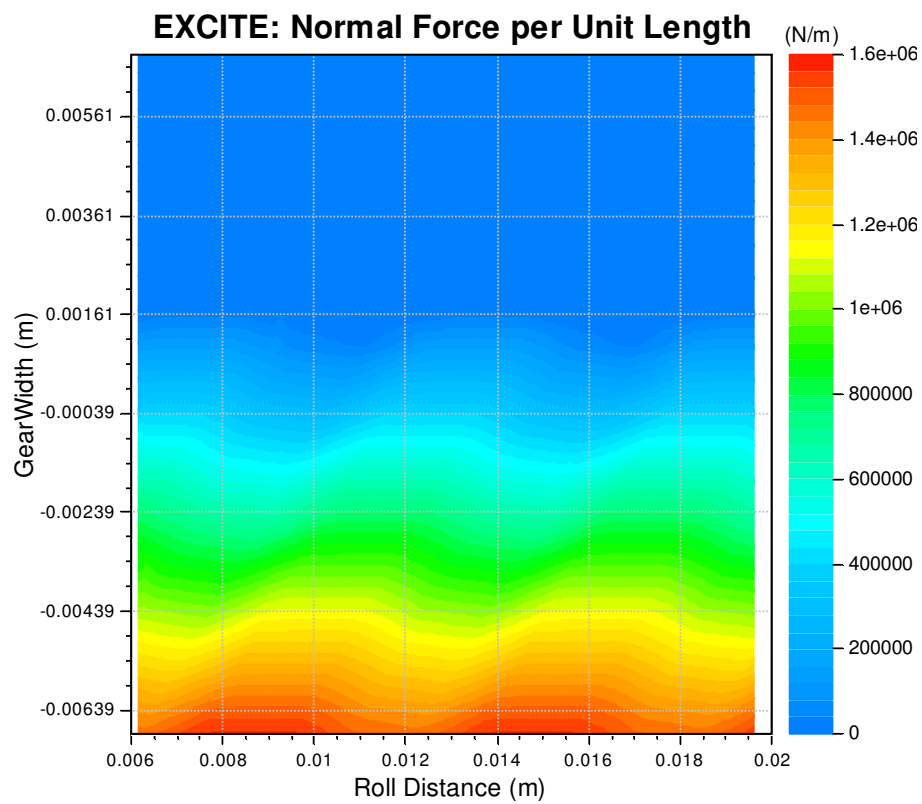


Figure 94: : Model G - Engagement field plot from EXCITE

### 7.6.8 Model H

The meshing stiffness (figure 95) in accordance with Weber/Banaschek in EXCITE is about seven percent smaller than the result calculated by KISSsoft while the normal mesh deformation (figure 96) is about 15 percent higher.

Following Weber/Banaschek's approach, the normal mesh deformation and respectively the meshing stiffness is depending on the bending arm of the tooth. This relation can be represented in a simplified form by a cantilever beam with a constant moment of area moment  $I$ . The deflection is depending on the bending arm  $l$  as outlined in equation 13.

$$w(l) = \frac{Fl^3}{3EI}$$

Equation 13: Deflection of a cantilever beam

Therefore, the normal mesh deformation of on tooth is increasing while the contact point on the flank surface is moving towards the tip diameter. At the same time, the contact point of the mating tooth is moving towards the root circle diameter. As result, the mating flank pair delivers the lowest normal mesh deformation and the highest meshing stiffness in the area of the operating pitch circle diameter and decreases towards the tip/root diameter, as it can be seen in figure 95 and figure 96.

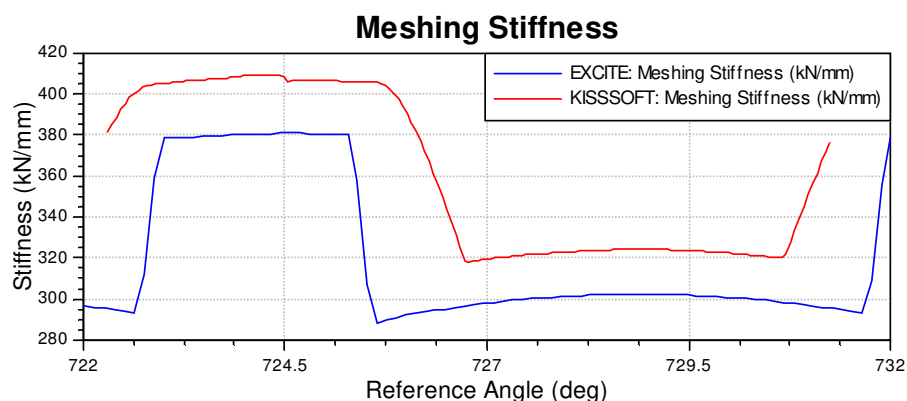


Figure 95: Model H - Meshing stiffness

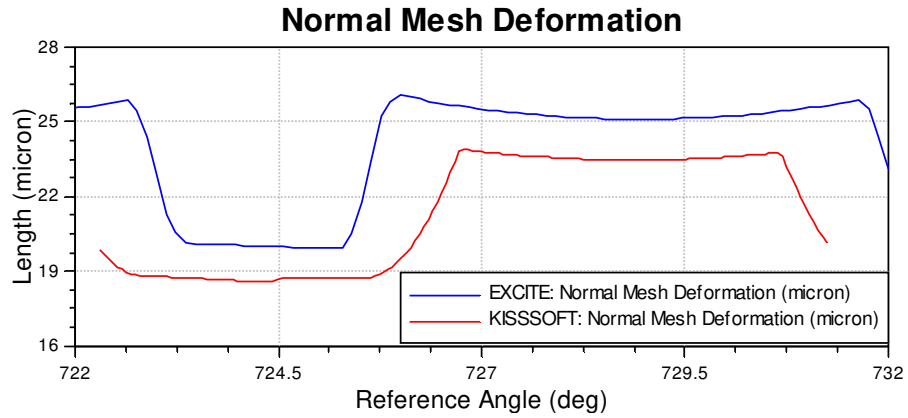


Figure 96: Model H - Normal mesh deformation

The normal force per unit length, aside the transition between the numbers of flank pairs in contact, are identical (figure 97).

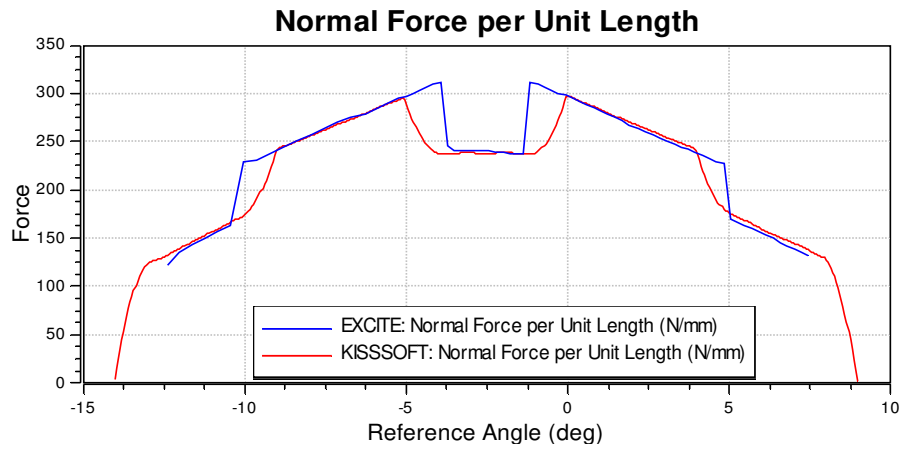


Figure 97: Model H - Normal force per unit length

The engagement field plot results are congruent (figure 98 and figure 99).

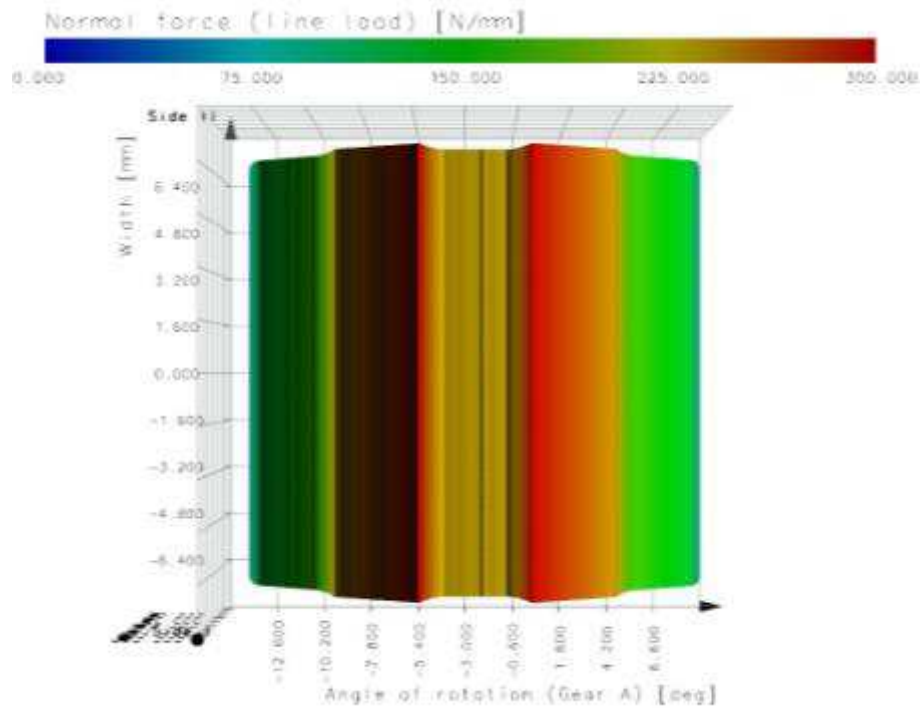


Figure 98: Model I - Engagement field plot from KISSsoft

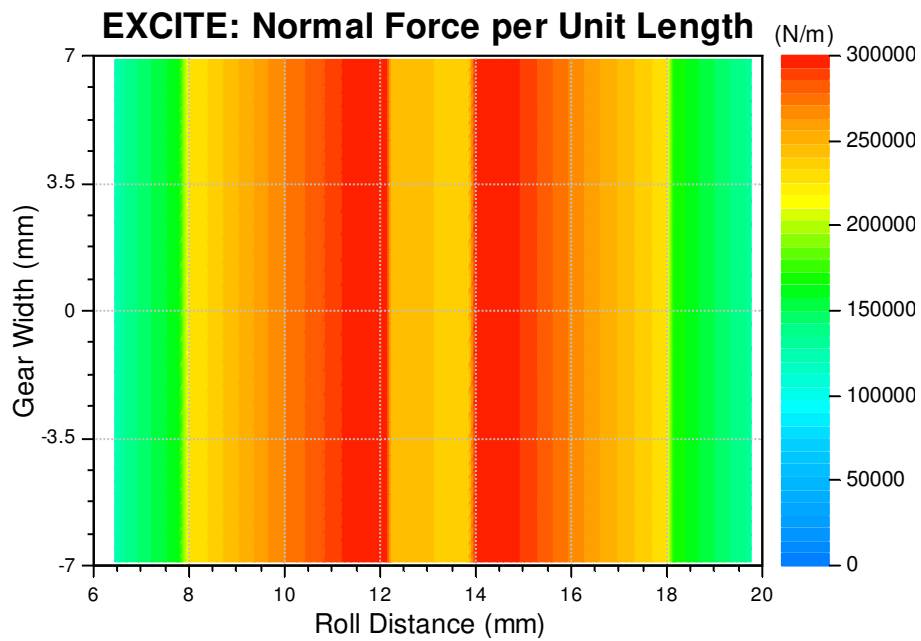
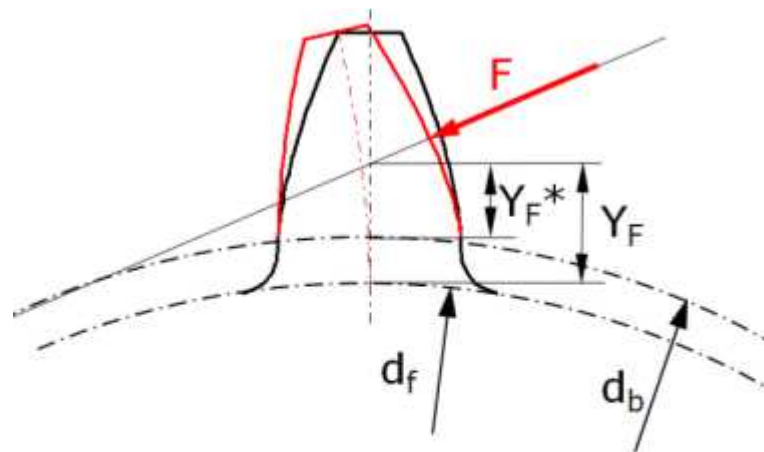


Figure 99: Model H - Engagement field plot from EXCITE

### 7.6.9 Model I

The cause for the deviations between KISSsoft and EXCITE in the previous model is the quadratic approximation of the flank surface in EXCITE with respect to the evaluation of tooth bending and tilting. Since in EXCITE the approximation starts at the base circle diameter instead of the root circle diameter, the beam length  $Y_F - Y_F^*$ , as shown in figure 100, is the amount of difference. The smaller beam length  $Y_F$  results in a higher tooth bending stiffness and finally into a higher meshing stiffness. To evaluate the impact of this error, the gear data of the previous model is modified such that the base circle diameter agrees to the root circle diameter.



$Y_F^*$  ... Beam length in EXCITE  
 $Y_F$  ... Beam length in KISSSOFT

Figure 100: Beam length in EXCITE and KISSsoft (source: [7])

As a result of this adjustment, the meshing stiffness (figure 101) and the normal mesh deformation (figure 102) in EXCITE nearly approaches the results from KISSsoft.

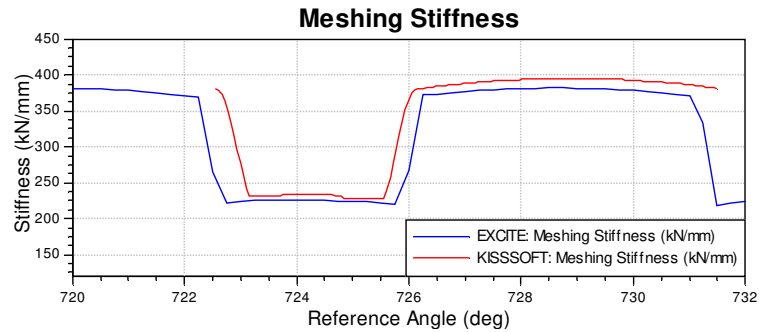


Figure 101: Model I - Meshing stiffness

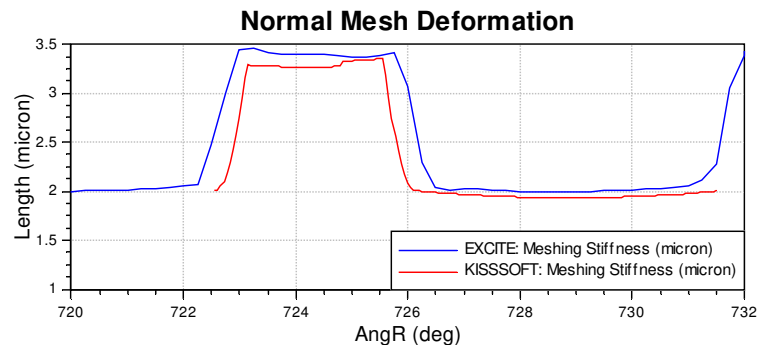


Figure 102: Model I - Normal mesh deformation

Due to the modification of the gear data the contact ratio  $\epsilon_\alpha$  is 1.609. This means that the number of flank pairs in contact changes between one and two, as it can be seen in the figure 103. The normal force per unit length fits just as in the last model.

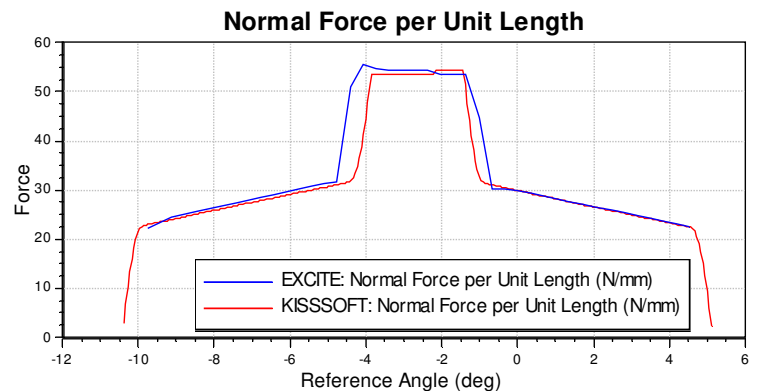


Figure 103: Model I - Normal force per unit length

The engagement field plots are congruent (figure 104 and figure 105).

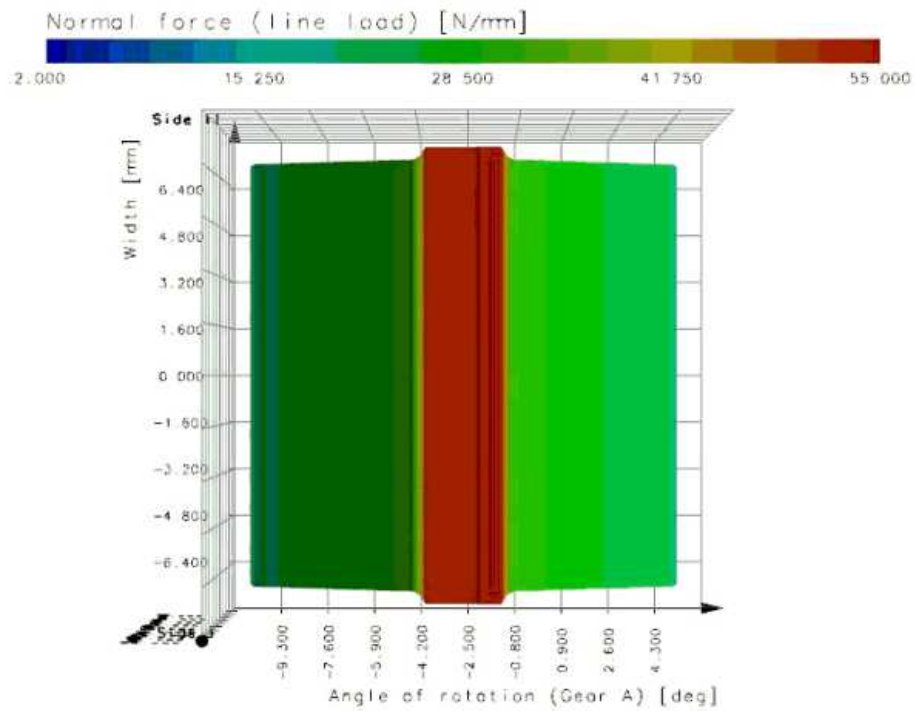


Figure 104: Model I - Engagement field plot from KISSsoft

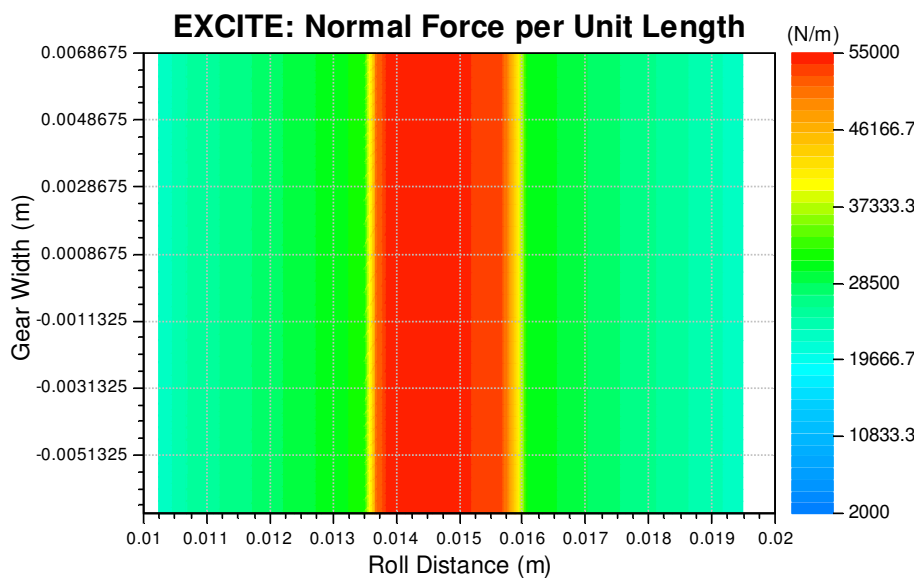


Figure 105: : Model I - Engagement field plot from EXCITE

### 7.6.10 Model J

The intentionally low load torque of 2 Nm has a significant impact on the result during the change of the number of flanks in contact as it can be seen by a comparison between the results of this model and the previous (figure 101, figure 102, figure 106 and figure 107).

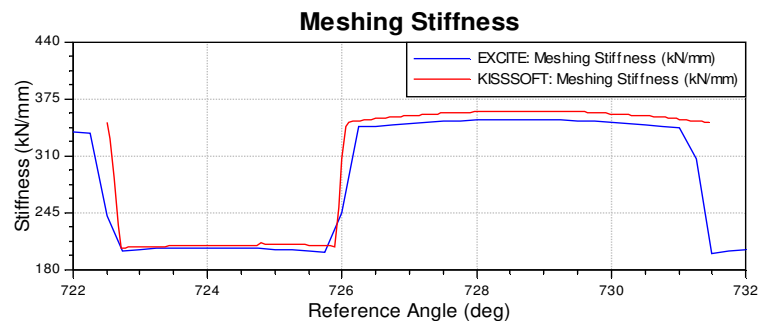


Figure 106: Model J - Meshing stiffness

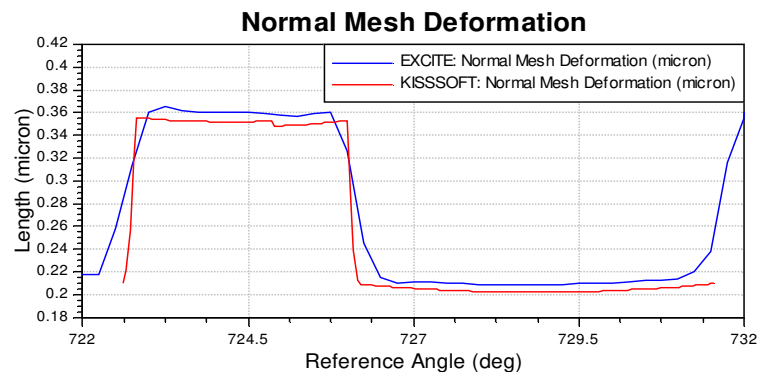


Figure 107: Model J - Normal mesh deformation

By the decreased torque the gradient of the curve between the change of the flank pairs in contact increased (figure 108).

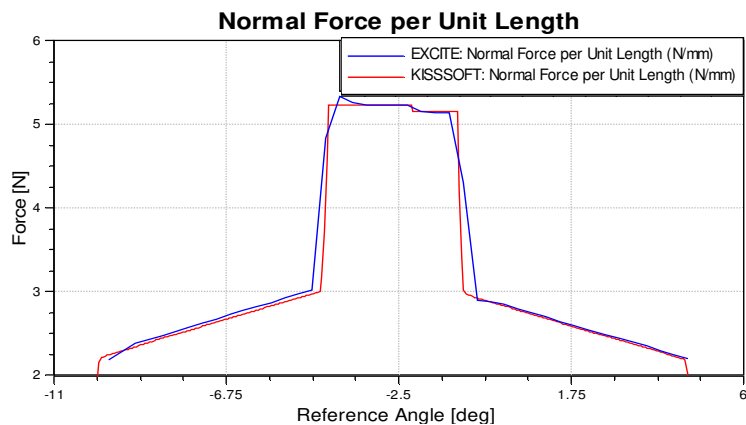


Figure 108: Model J - Normal force per unit length

The engagement field plots are consistent (Figure 109 and Figure 110).

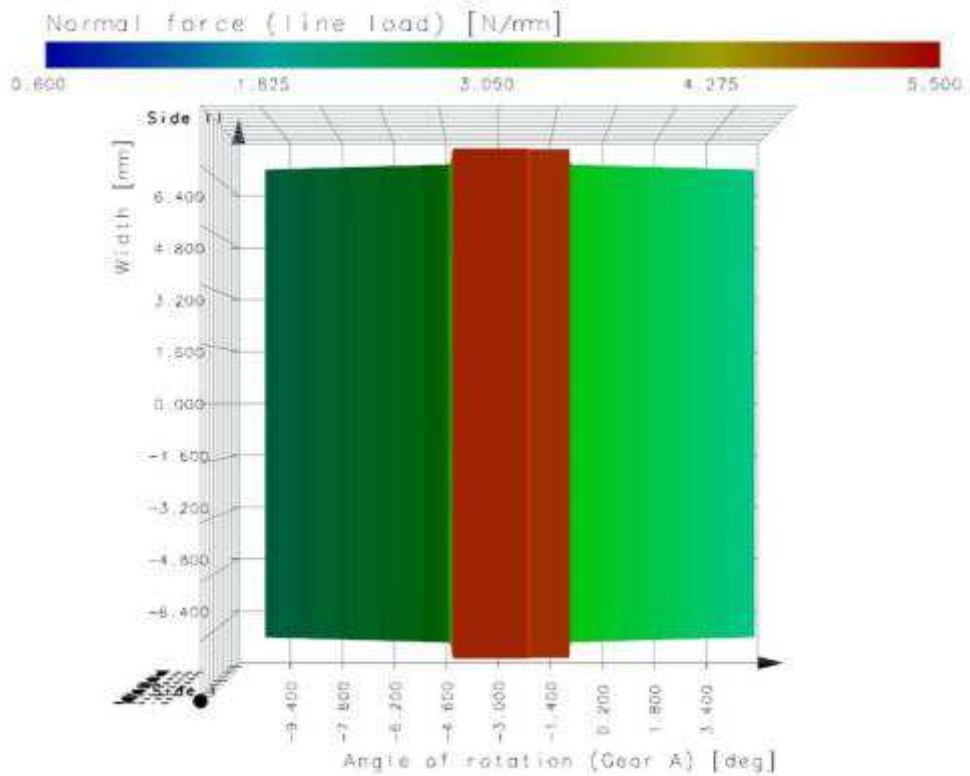


Figure 109: Model J - Engagement field plot from KISSsoft

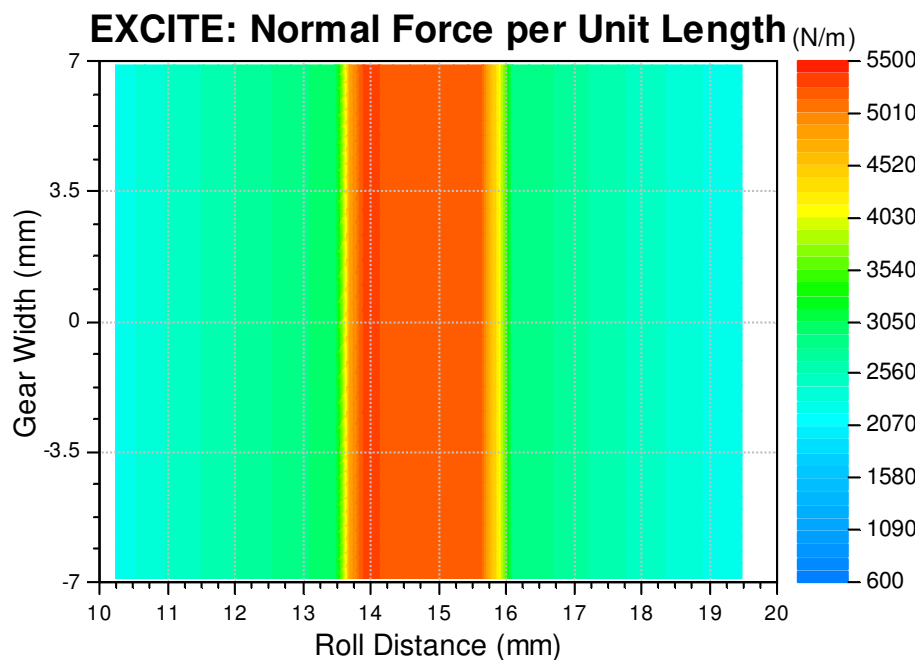


Figure 110: : Model J - Engagement field plot from EXCITE

## 7.7 Influence of the elastic mesh deformation on the path of contact and the contact ratio

The elastic deformation of the teeth enables a contact of the flank surfaces out of the regular path of contact. Such out of plane of action effects typically happen at the engagement and disengagement of the teeth and are characterised by the contact of pinion/gear tip circles with the opposing involutes. This results in an increase of the length of the path of contact, as shown in the figure 111. With the background of computational performance EXCITE is limiting the contact search to the involute parts of the flank. Consequently, effects like pre-engagement and post-disengagement (both occurring outside the plane of action) are not considered in EXCITE but regarded in KISSsoft. Since pre-engagement and post-disengagement basically scale with the extent of the meshing force, three models with varying torques (2.5 Nm, 25 Nm and 250 Nm) are compared. The simplified spur model with a linear stiffness is used for the evaluation. By doing so the load dependant Hertzian contact stiffness can be intentionally disregarded.

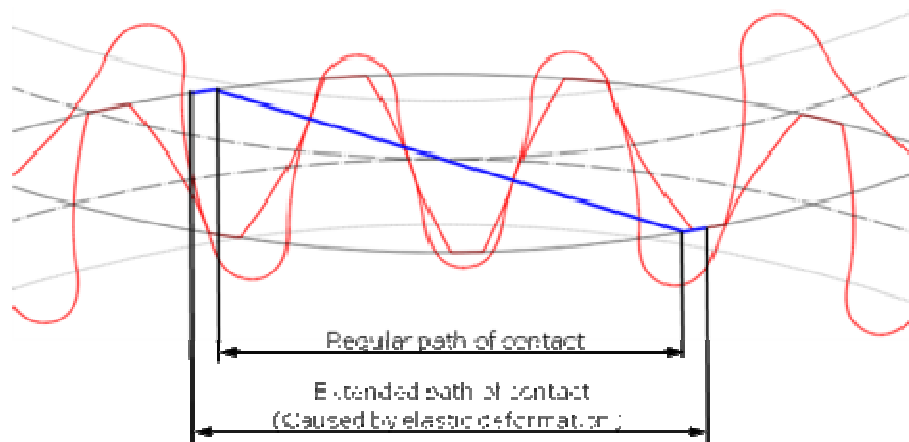


Figure 111: Influence of the elastic mesh deformation on the path of contact

- Meshing stiffness

The variation of the torques has no impact on the computed stiffness in EXCITE as it is shown by figure 112. The fluctuations are triggered numerically and by the output resolution of the result storage.

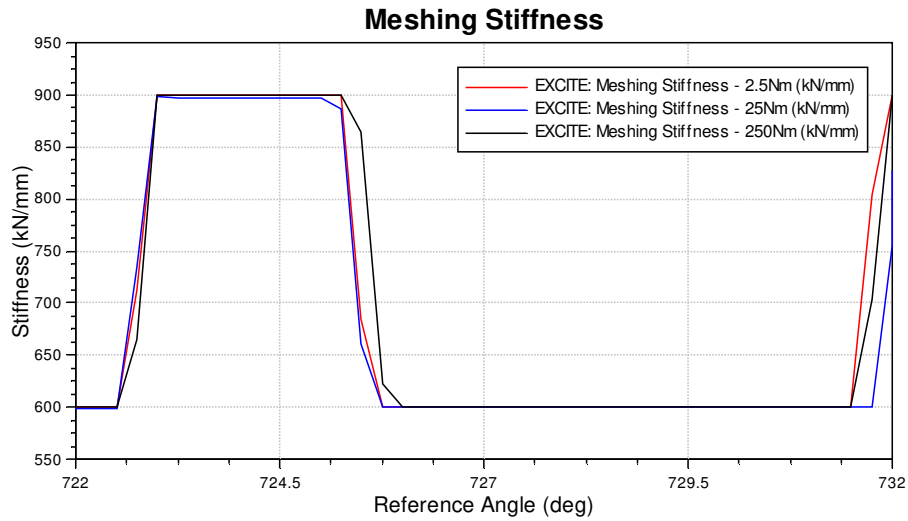


Figure 112: Impact of the variation of the torque on the EXCITE meshing stiffness

The lower the torque, the higher the gradient of the meshing stiffness is in KISSsoft during the change of the number of flank pairs in action (figure 113).

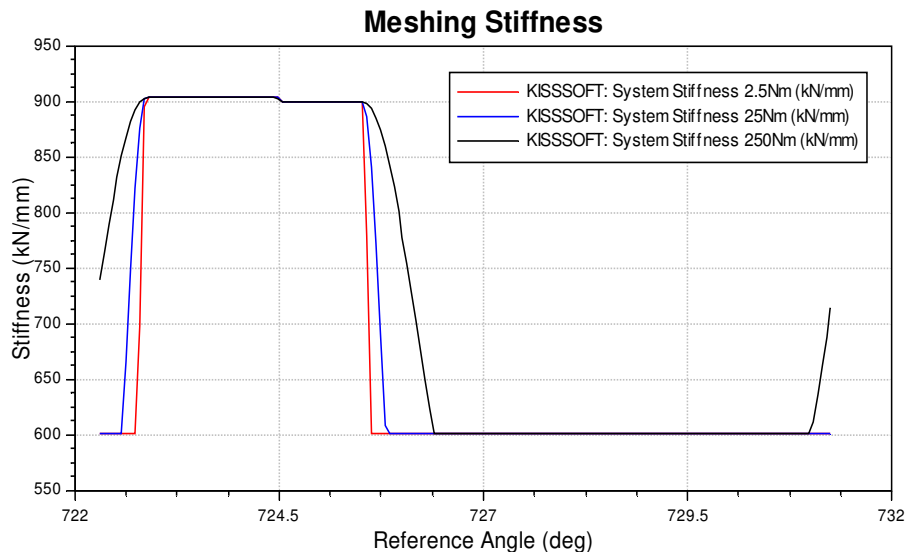


Figure 113: Impact of the variation of the torque on the KISSsoft meshing stiffness

With a decreasing torque the KISSsoft result approaches the result of EXCITE (figure 114).

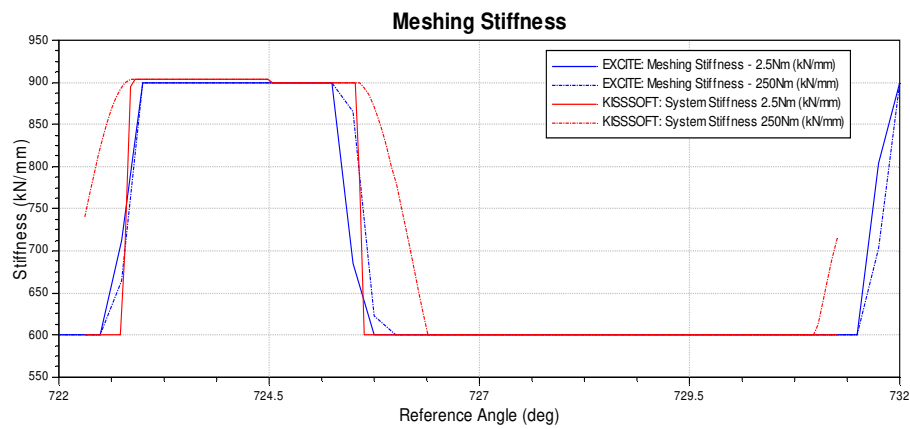


Figure 114: Comparison of the impact of variation of the torque on the EXCITE and KISSsoft meshing stiffness

- Normal mesh deformation

The normal mesh deformation is compared by a diagram with a logarithmic ordinate. Just as for the meshing stiffness the difference of the results decreases with lower torques.

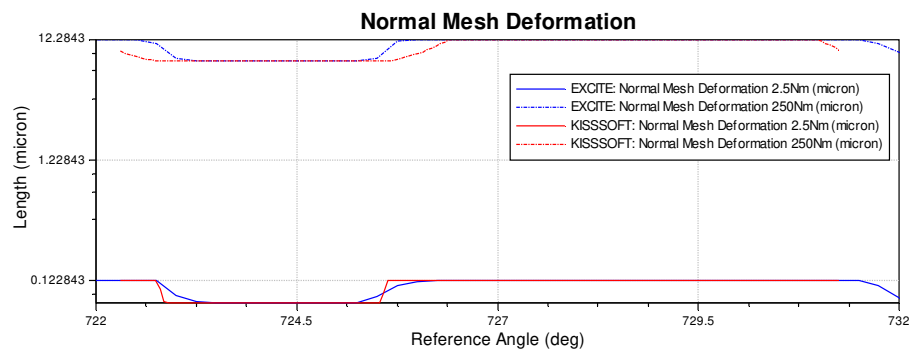


Figure 115: Comparison of the impact of variation of the torque on the EXCITE and KISSsoft normal mesh deformation

- Normal force per unit length

The change of the torque also effects the normal force per unit length (figure 116). To enable a comparison of the results, the normal force per unit length of the model with the torque of 2.5 Nm is multiplied by 100.

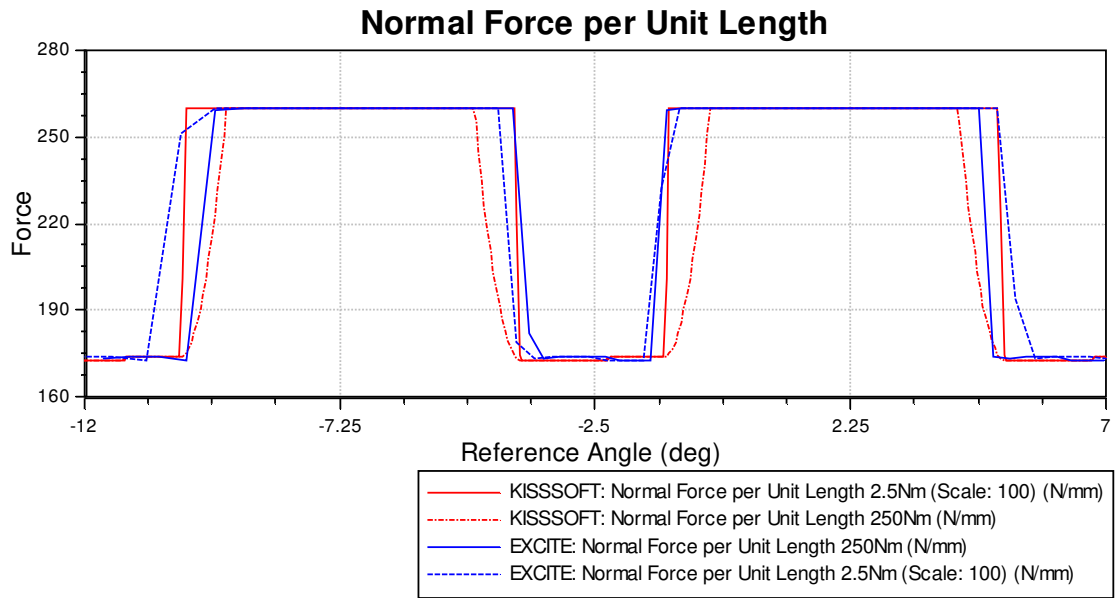


Figure 116: Comparison of the impact of variation of the torque on the EXCITE and KISSsoft normal force per unit length

- Engagement field plot

The figure 117 and figure 118 show the impact of the reduced torque on the engagement field plot in KISSsoft.

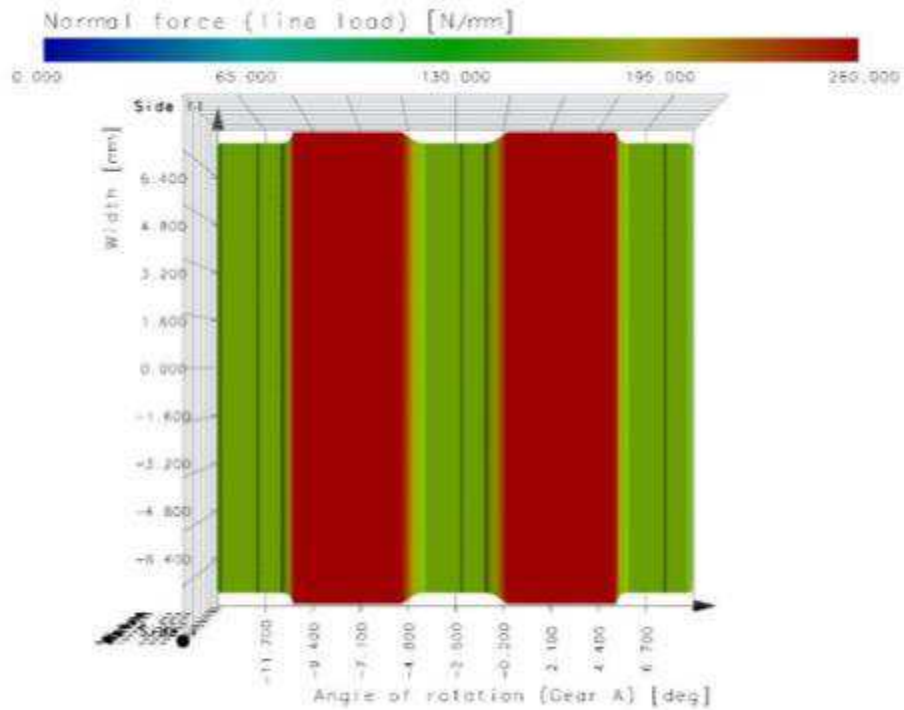


Figure 117: Engagement field plot of a spur model (torque 250 Nm)

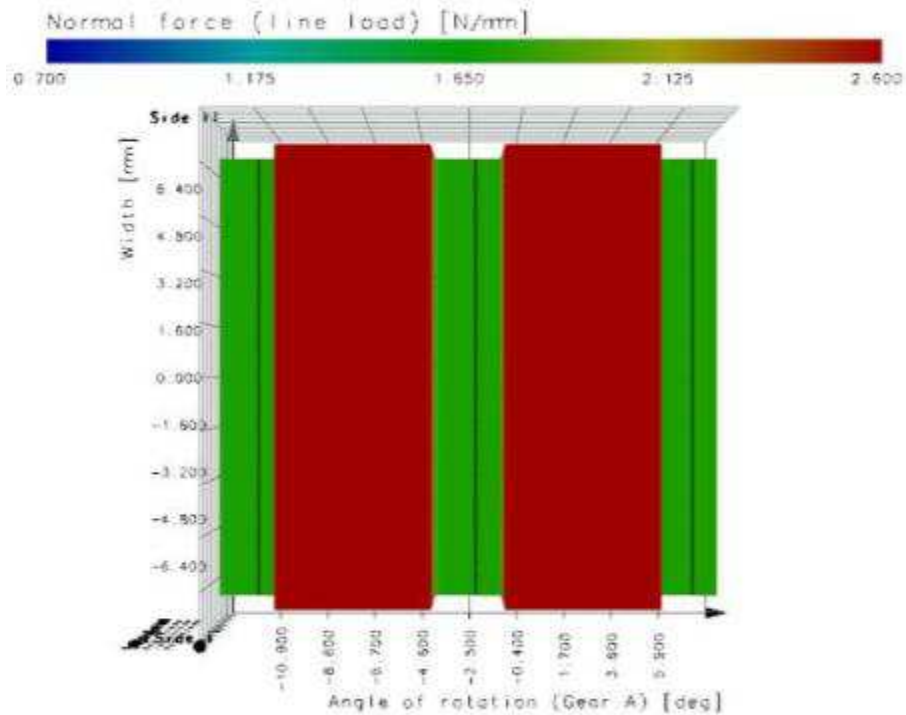


Figure 118: Engagement field plot of a spur model (torque 2.5 Nm)

## 7.8 Evaluation of the Petersen modified Hertz contact approach

The comparison of the implemented approaches with accordance to the Petersen modified Hertz contact between KISSsoft and EXCITE is based on three models. The first model is the simplified model. Then the simplified model is modified in a way to get models with a higher and a lower curvature of the involute.

In EXCITE it is possible to activate the three parts of the deformation separately and so it is also possible to only activate the contact stiffness only. This means that the meshing stiffness result matches the Petersen / Hertz contact stiffness and can be used for the comparison. In KISSsoft this option is not available but a separate result of the contact stiffness for one flank pair can be computed. To compare this result with EXCITE it has to be multiplied with the current number of flank pairs in contact.

### 7.8.1 Simplified model

The figure 119 shows the tooth form of the mating gears and the path of contact of the simplified model.

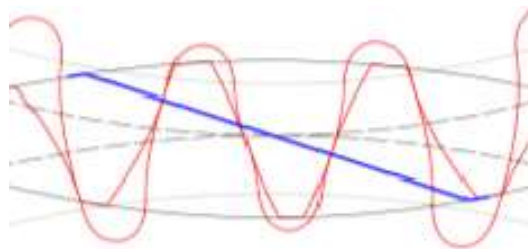


Figure 119: Gear mesh of the simplified model

The comparison shows that the results are consistent for two flank pairs in action, as shown in figure 120. For three flank pairs, the curve of the last flank pair in KISSsoft falls off, where the same value as for the other two flank pairs is expected. Besides the numerical fluctuation, EXCITE delivers a constant result for two and three flank pairs in action.

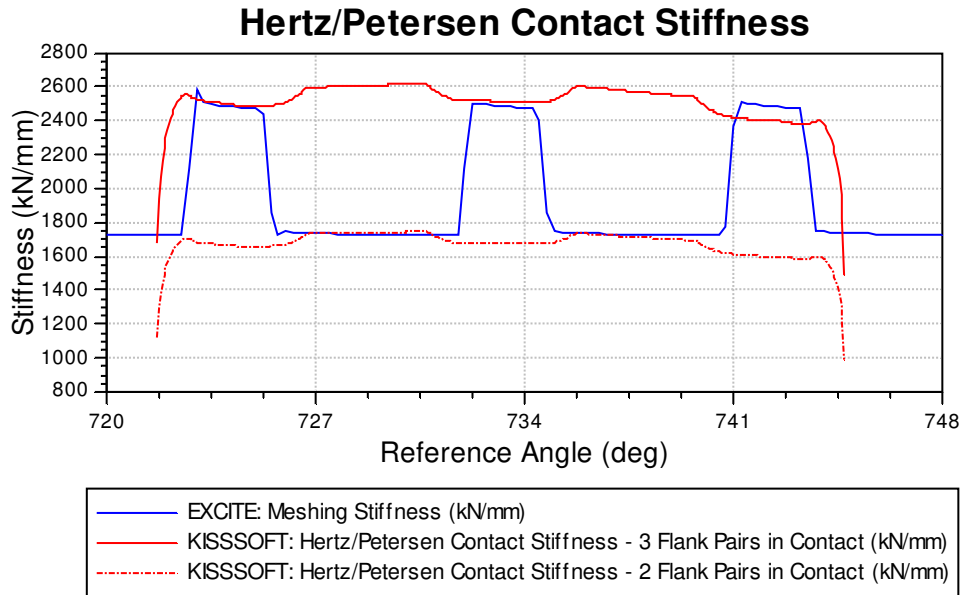


Figure 120: Hertz/Petersen contact stiffness of the simplified model

### 7.8.2 Model with a increases curvature of the involute

The increase of the involute curvature is obtained by a reduction of the number of teeth to ten. The resulting tooth form and the path of contact can be seen in figure 121.

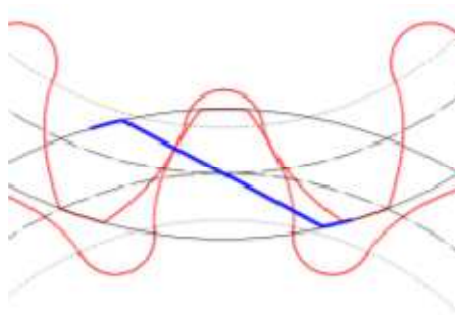


Figure 121: Gear mesh (ten teeth per gear)

As a result of the lower number of teeth, the contact ratio decreases from 2.30 to 1.04. During one tooth is in contact the result matches, as shown in figure 122. When the number of flank pairs changes from one to two, the result is no longer comparable because of the dynamic effects additionally considered in EXCITE.

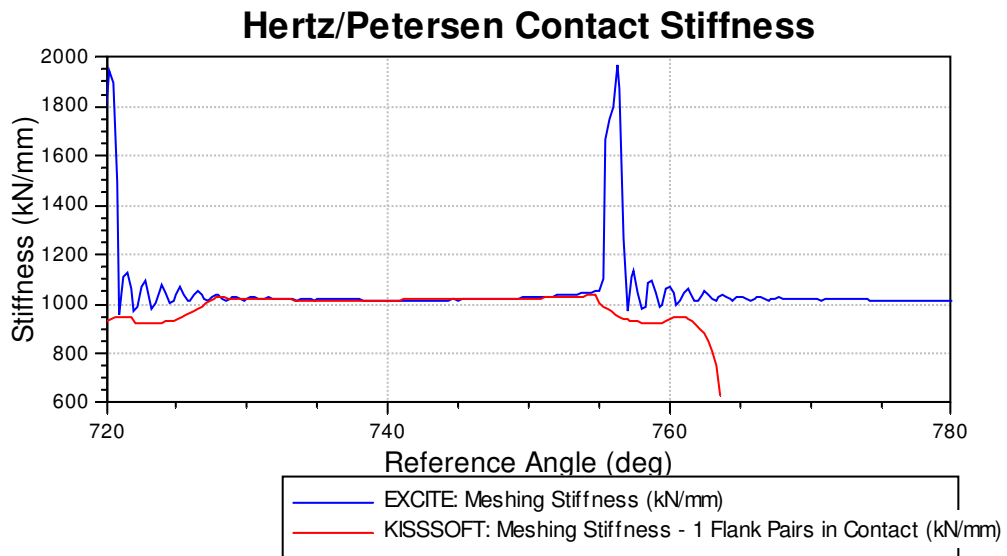


Figure 122: Hertz/Petersen contact stiffness (ten teeth per gear)

A more detailed plot (figure 123) shows the impact of the change in curvature along the contact, which decreases from the base circle diameter to the tip circle diameter on the level of stiffness.

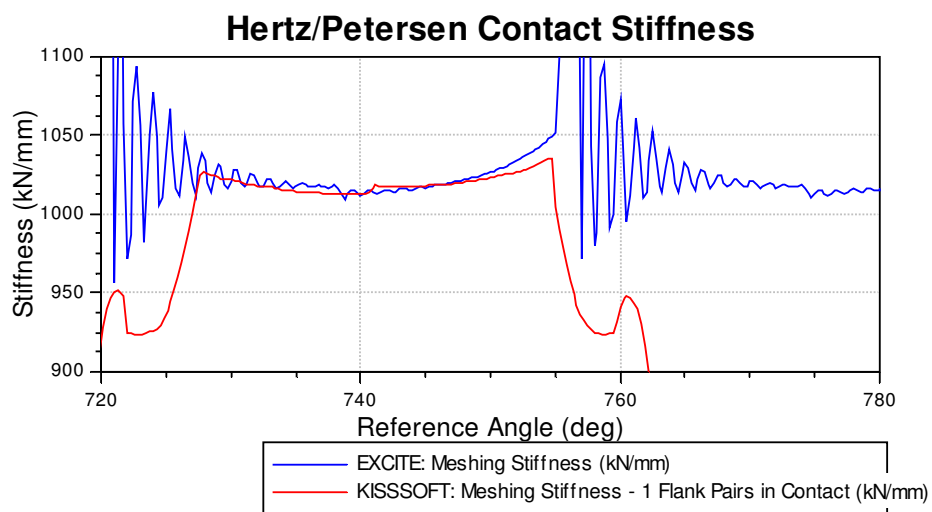


Figure 123: Hertz/Petersen contact stiffness in detail (ten teeth per gear)

### 7.8.3 Model with a decreased curvature of the involute

Due to the increase of the number of teeth to 100, the curvature of the flank surface decreased, as it can be seen in figure 124.

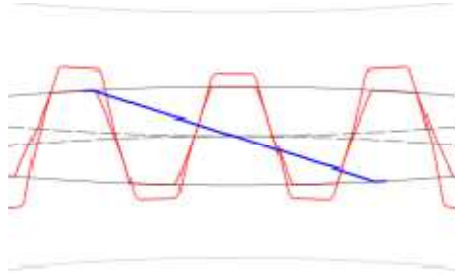


Figure 124: Gear mesh (100 teeth per gear)

The comparison of EXCITE and KISSsoft indicates a deviation about three percent for this model (Figure 125).

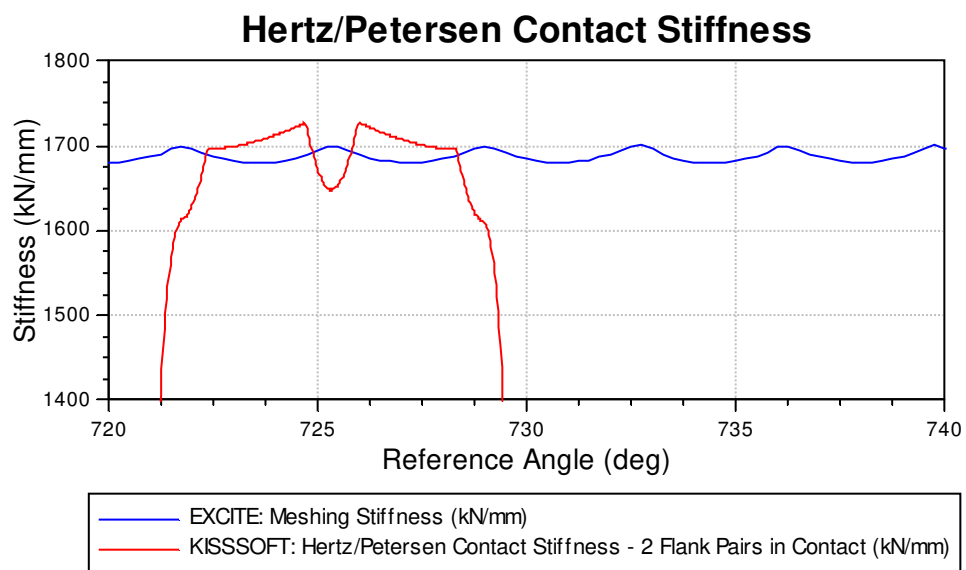


Figure 125: Hertz/Petersen contact stiffness (100 teeth per gear)

## 8. Summary and outlook

In all models, EXCITE deviates from KISSsoft during the transition of the number of flank pairs in action. This deviation decreases with by reducing the acting torque as the comparison of the models I and J shows. The observed differences can be traced back to the fact that EXCITE is not accounting for out of plane of action contacts.

Beside this effect, the spur model without spatial angular misalignment fits between EXCITE and KISSsoft. The helical model without angular misalignment differs, even after the slice motion is corrected form normal to face cut, within eight percent in the meshing stiffness and seven percent in the normal mesh deformation.

The applied skew misalignment shows consistency for all compared results. Even by raising the amount skew misalignment to 50 micron, where only 61 percent of the gear width is holding a load, the results show adequate consistency.

The applied slope misalignment on the spur and helical model leads to an overcompensation of the spatial misalignment. All results differ significantly between EXCITE and KISSsoft. As consequence, the superposition of slope and skew misalignment results into an overcompensation too.

The comparison of the applied deformation approach according to Weber/Banaschek shows a deviation of 15 percent of EXCITE. As the model I proves, the results coincide when the root circle diameter matches the root circle diameter. This confirms the assumption that the quadratic approximation of the flank surface leads to a higher meshing stiffness as outlined in chapter 3.5. By additionally reducing the acting torque to 2 Nm, all compared results of this model show reasonable agreement between EXCITE and KISSsoft.

The variation of the acting torque shows a significant impact on the engagement length and therefore on all results in KISSsoft. In EXCITE the contacts out of the plane of action are not regarded, which means that the variation of the torque has no impact on the engagement length. As result, all compared quantities differ between EXCITE and KISSsoft during the transition of the number of flank pairs in action.

The applied Hertzian contact stiffness approaches in EXCITE and KISSsoft are consistent for the simplified model. Further, they react in the same way on a increased curvature of the involute. The model with the decreased curvature of the involute leads to a deviation of three percent. In summary the applied Hertz/Petersen contact stiffness approach in EXCITE shows for all investigated model a sufficient coherence with KISSsoft.

## **8.1 Geometrical verification**

The validation shows a divergence among the results for models with slope misalignments. Therefore, it is investigated if the basic assumptions of the ACYG gear contact model is leading to geometrical errors, which further result into an overcompensation of slope misalignments. Moreover, it is investigated if the computations carried in the ACYG-joint can be improved such that the behaviour conforms with KISSsoft.

### *8.1.1 Geometrical verification of the slice equivalent deformation by mean of CAD software*

As outlined in chapter 3.5, the calculation of the forces by the ACYG joint is based on the penetration area, which is constituted by the penetration at the beginning, the middle and at the end of each slice, as outlined in chapter 3.3. Since all three values undergo the same computation procedure and the slope misalignment is per definition a linear function, the middle value is congruent with the averaged value of the slice, is only slope is applied. Further, due the linear function of the slope misalignment, the slice equivalent deformation of only one slice has to be compared to verify the computation algorithm. Hence, the computed deformation of a representative slice is compared with the geometrical overlap in the CAD software.

The verification is based on the simplified model with a constant stiffness, without backlash and a slope misalignment of 38.5 micron. Since the model has no backlash applied in the ACYG joint, the slope misalignment results into clamping of the gears and therefore, both flank sides (right and left flank pairs) are in contact and deliver a deformation result. The difference of the deformation for the right and left flank pair is caused by the torque. Finally, the averaged quantity is just triggered by the clamping and therefore conforms to the measured overlap in CAD as the CAD software CATIA V5R17 is used. The accuracy of a generated geometry in CATIA is 0.001 mm. The geometry of one tooth is imported from EXCITE as scatter plot which is then converted into a solid. This solid, in the shape of one tooth, is then used to generate the whole gear.

Due of the linear function of the slope misalignment the first slice of the model has the greatest overlap and is therefore chosen for the geometrical verification. As measurement plane, the XY-plane of the joint coordinate system is used and it is located at the mid axial position of the first slice, as shown in figure 126. The same axial position is utilized in CAD to measure the geometrical overlap. The intersection of the measurement plane and the plane of action gives the direction and location of the measurement.

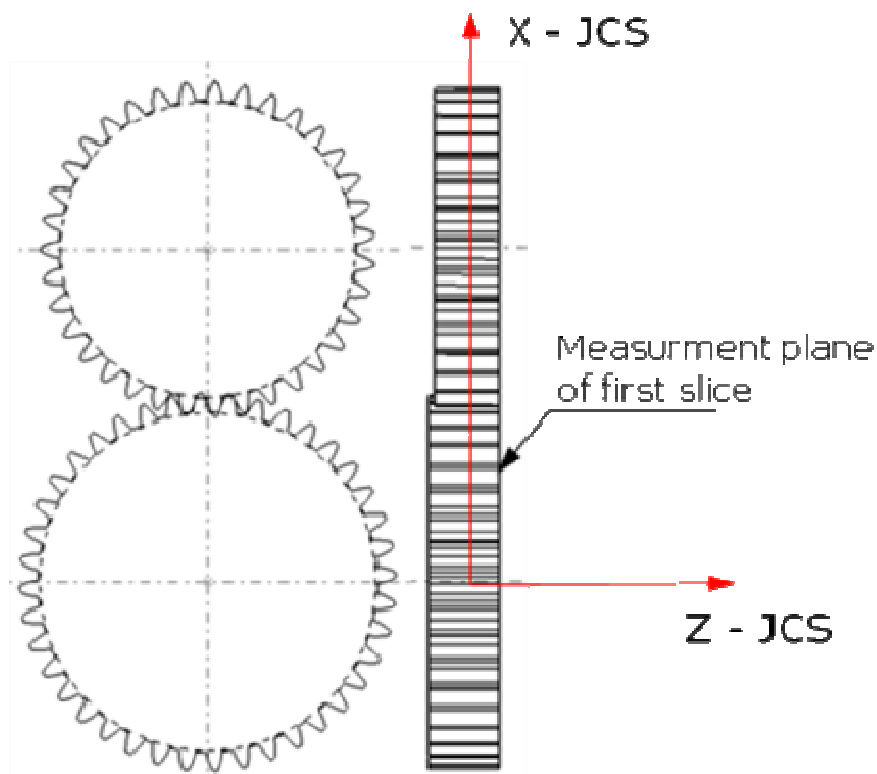


Figure 126: Measurement plane for geometrical verification

Figure 127 shows the slice equivalent deformation for both flank sides and the averaged value, as computed by EXCITE. The averaged slice equivalent deformation is 60.25 micron and the measured overlap in CAD, which is shown in the detail A in figure 128, is 5.36 micron. The difference of 54.89, where these two values should be identical, deduces on a significant deviation caused by the implemented algorithm.

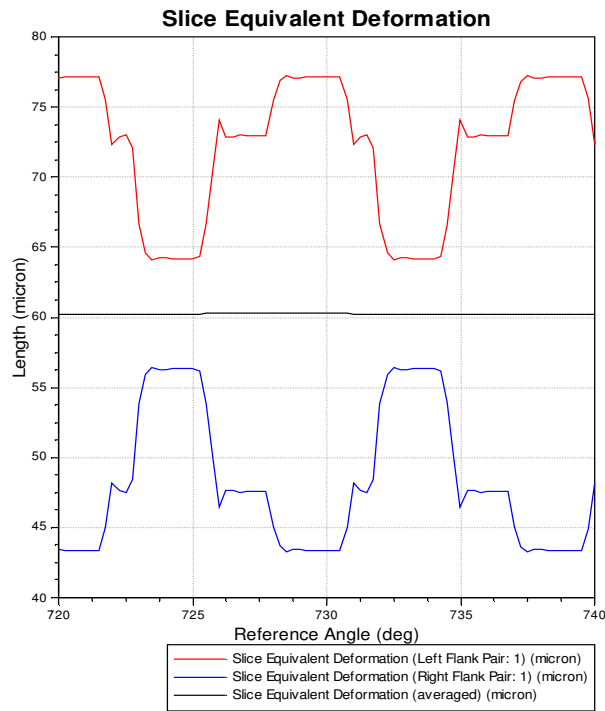


Figure 127: Slice equivalent deformation

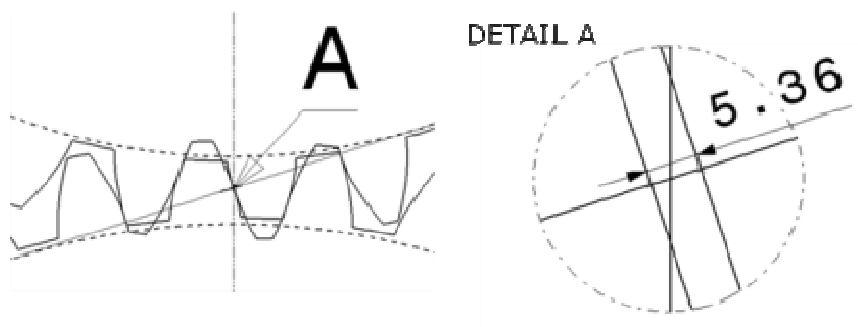


Figure 128: Geometrical overlap in CAD

Since the constitution of the deformation field is based on the detection of the contact points (see chapter 3.3 and 0), which are calculated for ideal aligned axes, the impact of the slope misalignment on the computed position of the contact points have to be examined.

### 8.1.2 Geometrical verification of the slice contact points

The contact points computed by the ACYG joint are compared with the contact points in CAD. The same model as in the chapter 8.1 is used. To enable the comparison of the position of the contact points, which are static coordinates in CAD, the degrees of freedom of the pinion body in the model are switched off, which means that the body remains, after the equilibrium of the forces was found, in a static position. To ensure the correct position of the bodies and therefore of the flank surfaces, the angular positions of the bodies in EXCITE are used as angular offset of the parts in CAD. The coordinates of the contact points are measured based on the joint coordinate system.

Due to the slope misalignment, the center distance of the current slice is reduced from the nominal value of 77 mm to 76.981 mm. Figure 129 shows the contact points (represented by red circles) and their deviation from CAD in micron. The deviation is measured in direction of the X-axis of the joint coordinate system. A positive deviation means the contact point in EXCITE has a higher X-coordinate. For all contact points, EXCITE differs from CAD.

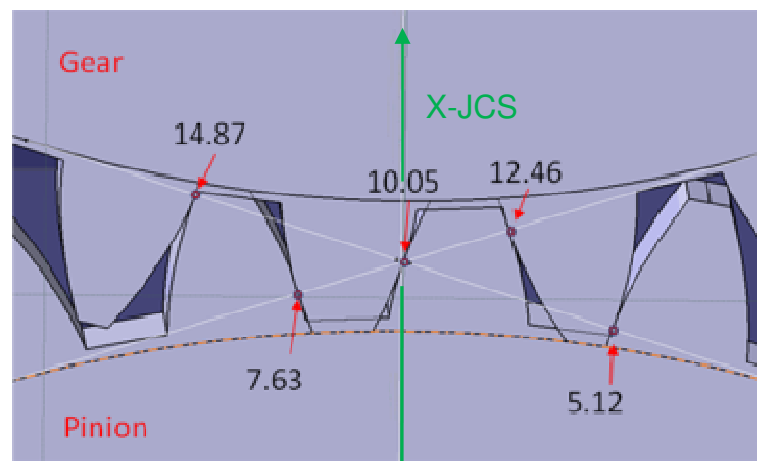


Figure 129: Vertical offset of the contact points between the ACYG joint and CAD (micron)

In order to correct the divergence of the contact points, which is caused by assumptions in the ACYG joints, an algorithm to correct the position of the contact points has to be developed and implemented.

## 8.2 Development of an algorithm to correct the position of the contact points with respect to slope misalignment

The observed deviation of the slice contact points can be traced back to EXCITE's assumption that contact lines holding the points are computed for the ideal non-misaligned state. This simplification is basically motivated by reasons of computational performance, since the intersection of ideal involutes can be carried out with moderate effort. To correct the computation of the contact points in order to account for angular misalignments more precisely there are two possibilities. The first possibility is to modify the detection of the contact as outlined in chapter 3.3 and the second one is to correct the position of the contact points afterwards based on the ideal values.

Generally, the computation of the ACYG joint is divided into several source code files, where only the necessary quantities are available in each file. The computation of the contact detection is based on axes without angular misalignment. To calculate the correct position of the contact points, the information about the angular position of the axes, for example, would be necessary. But due to the structural circumstances of the ACYG-code, it is not possible making this information easily available in the relevant code parts without a general redesign of the ACYG source code arrangement. Therefore, the contact points are modified in the source code part, where the discretization into slices is applied and all necessary information of each slice is available.

In order to develop the algorithm, the dependency of the position of the contact points on the change of the slice center distance is used. On average the deviation of the contact points, as measured in chapter 8.1.2, is 10.026 micron for the used model. The difference of the slice center distance and the nominal center distance is 19 micron. The average deviation, as negative value, can be assumed by multiplying the difference of the slice and nominal center distance with 0.5, which leads to

$$\Delta_{X-JCS} = 0.5(\text{SliceCenterDistance} - \text{NominalCenterDistance})$$

*Equation 14: Slice contact point correction value*

The deviation between the calculated correction value and the averaged measured values is 0.526 micron. However, since it is smaller than the accuracy of the geometry in CAD, it is negligible. In order to describe the position of the new contact point on the involute, the relation between the involute creation angle  $\alpha$  and the radius of the contact point is used as outlined in equation 15.

$$\alpha = \arccos\left(\frac{r_b}{r}\right)$$

*Equation 15: Involute creation angle  $\alpha$*

To correct the position of the old and new contact point, the delta between these two points is used. It is computed by

$$\Delta\alpha = \arccos\left(\frac{r_b}{r_{new}}\right) - \arccos\left(\frac{r_b}{r_{old}}\right).$$

*Equation 16: Involute creation angle correction value*

The ACYG joint uses a parametric representation to describe the contact points on the flank surface (see chapter 3.3), where the T2 parameter describe the position of the contact point in the direction of the height of the tooth (means along the involute) and the parameter T1 in the direction of the width. Therefore, to modify the position of the contact point on the involute, the correction has to expressed as T2 parameter. In order to meet the parameterization of the T2 parameter, the involute creation angle correction value must be divided by the involute creation angle of the tip diameter of the tooth as outlined in equation 17. A T2 value of one means the contact point is at the top of the involute (at the tip circle radius) and zero at the bottom (at the root circle radius).

$$\Delta T2 = \frac{\Delta\alpha}{\alpha_{d_a}}$$

*Equation 17: Parametrization of the involute creation angle correction value*

Since the slope misalignment per definition causes an angular misalignment of the axes, the deviations in the direction of the axis follow a linear behaviour. With this relationship, the necessary correction only has to be computed at the start and at the end of each contact line. With this two correction values a linear equation is found and used to determine the correction for each slice.

### 8.2.1 Validation of the modified ACYG code

To validate the modified ACYG source code, the model D from chapter 7.6.4 and the model G from chapter 7.6.7 are used. A slope misalignment is applied to both models.

- Model D

Due to the modification of the ACYG code, the comparison of the meshing stiffness, between the previous (figure 130) and the new result (figure 131) shows a significant improvement.

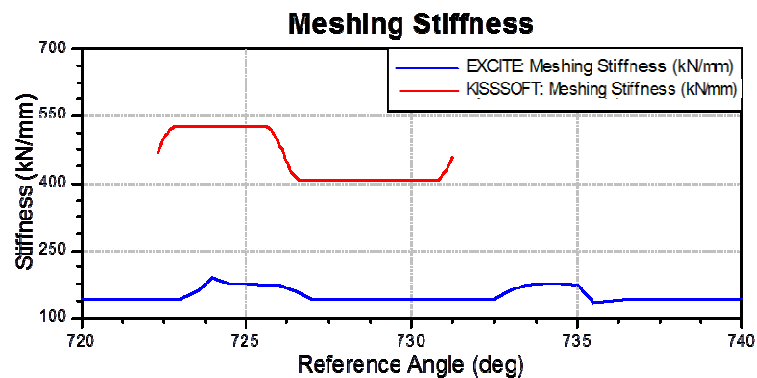


Figure 130: Model D - Meshing Stiffness

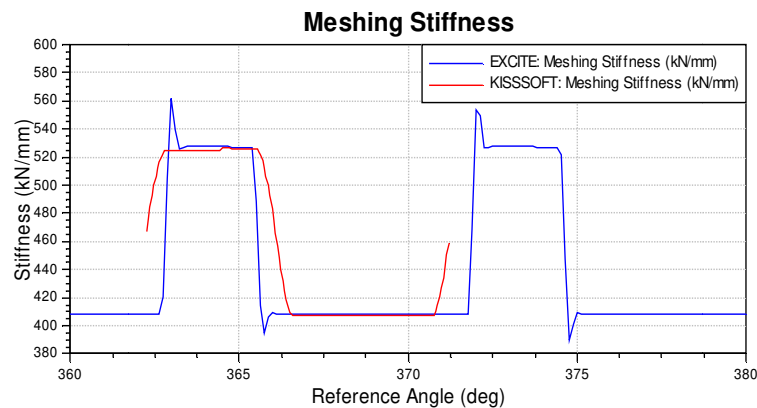


Figure 131: Model D - Meshing stiffness (computed with modified ACYG code)

Beside a deviation lower than one micron in the area of a constant number of flank pairs in action, the normal mesh deformation now fits between EXCITE and KISSsoft, as it can be seen in figure 132 and figure 133.

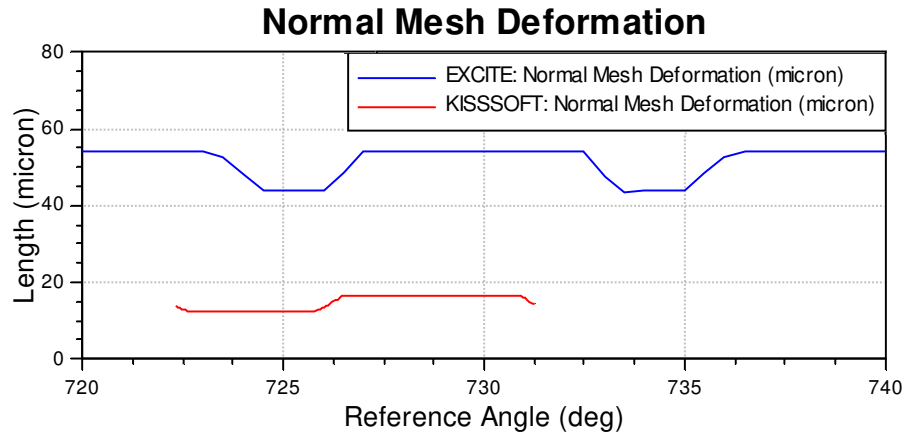


Figure 132: Model D - Normal mesh deformation

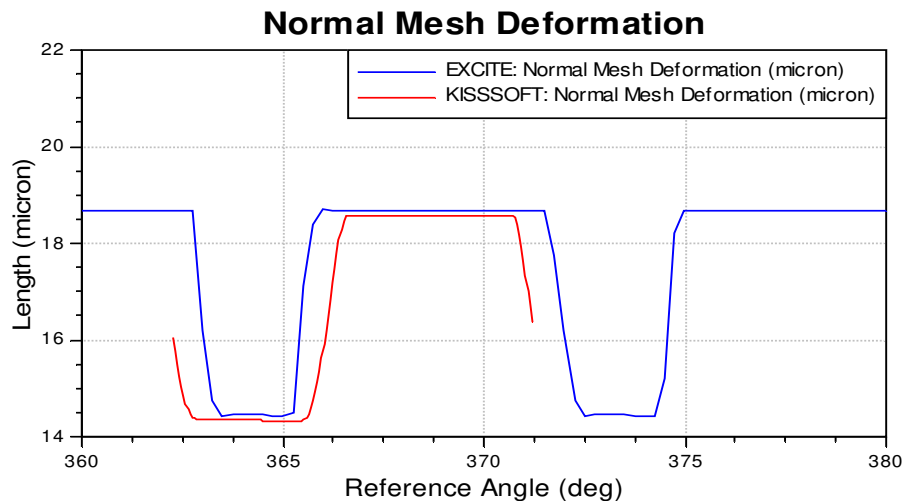


Figure 133: Model D - Normal mesh deformation (computed with modified ACYG code)

The normal force per unit length in EXCITE equals the result computed by KISSsoft in the area of a constant number of flank pairs in action (see figure 134 and figure 135).

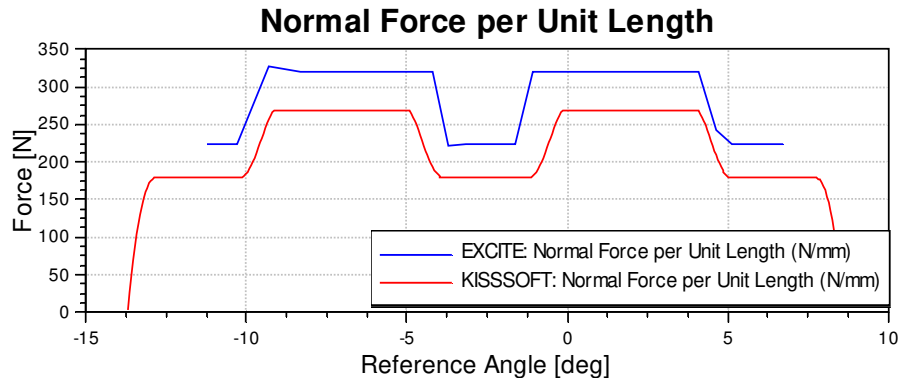


Figure 134: Model D - Normal force per unit length

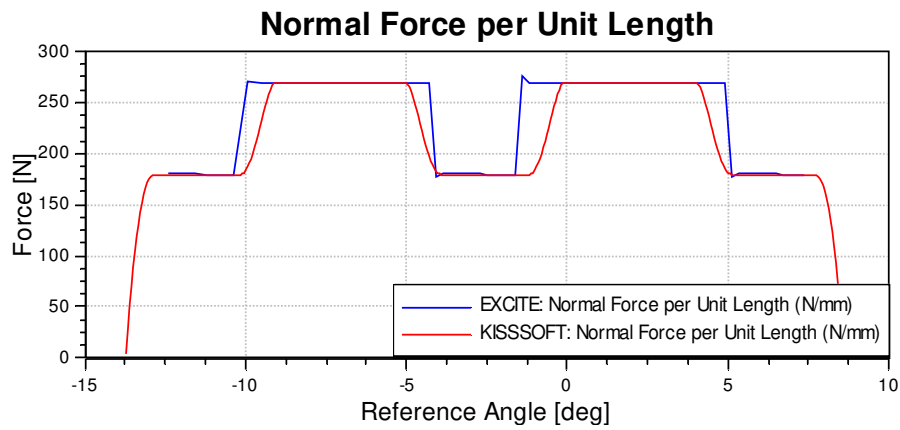


Figure 135: Model D - Normal force per unit length (computed with modified ACYG code)

The engagement field plot shows the impact of the modification of the ACYG code on the entire engagement and is quantitatively coherent between EXCITE (figure 136) and KISSsoft (figure 137).

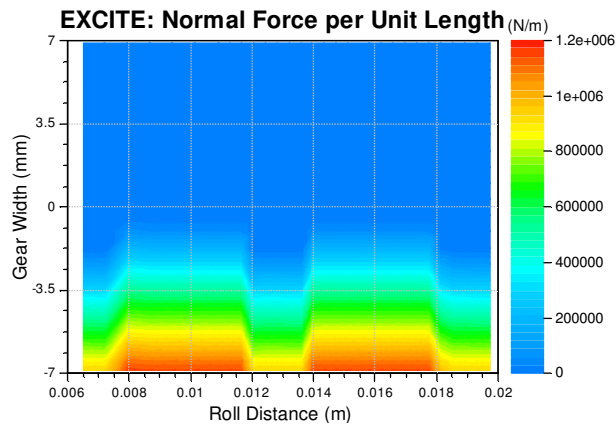


Figure 136: Model D - Engagement field plot from EXCITE

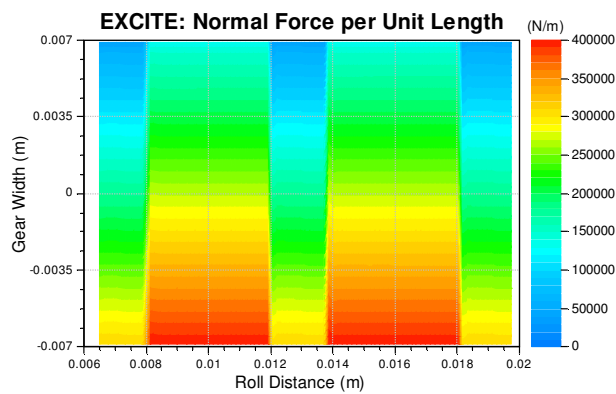


Figure 137: Model D - Engagement field plot from EXCITE (computed with modified ACYG code)

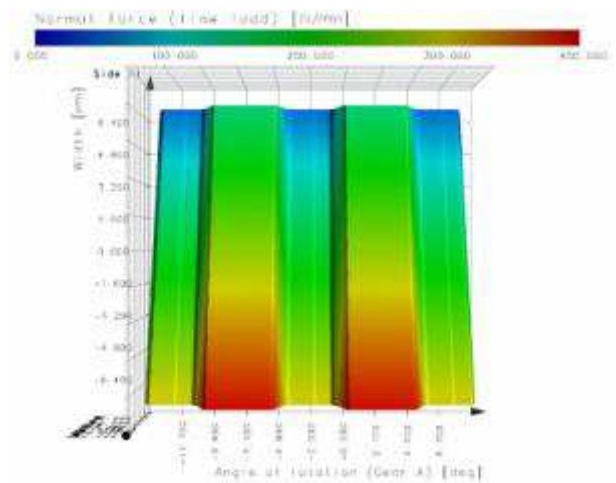


Figure 138: Model D - Engagement field plot from KISSsoft

- Model G

Deviation of the meshing stiffness of the helical model decreased between EXCITE and KISSsoft as it can be seen by comparison of figure 139 and figure 140.

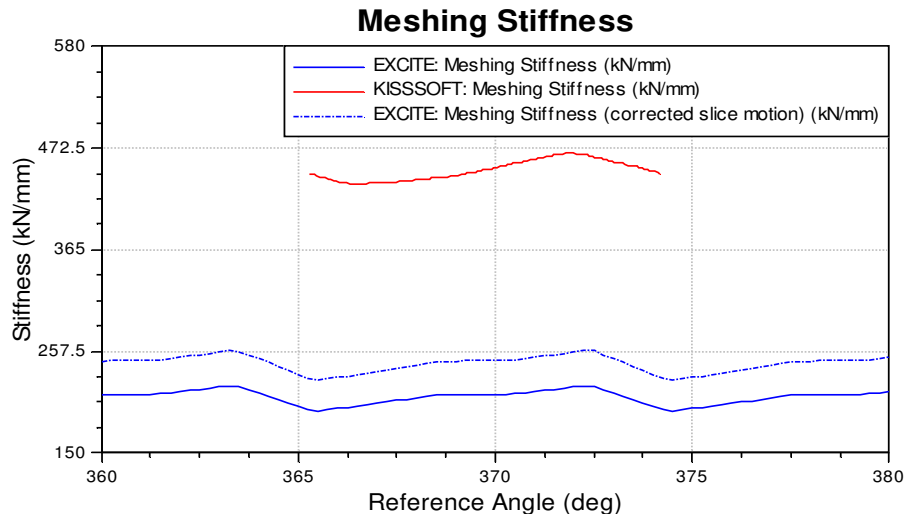


Figure 139: Model D - Meshing stiffness

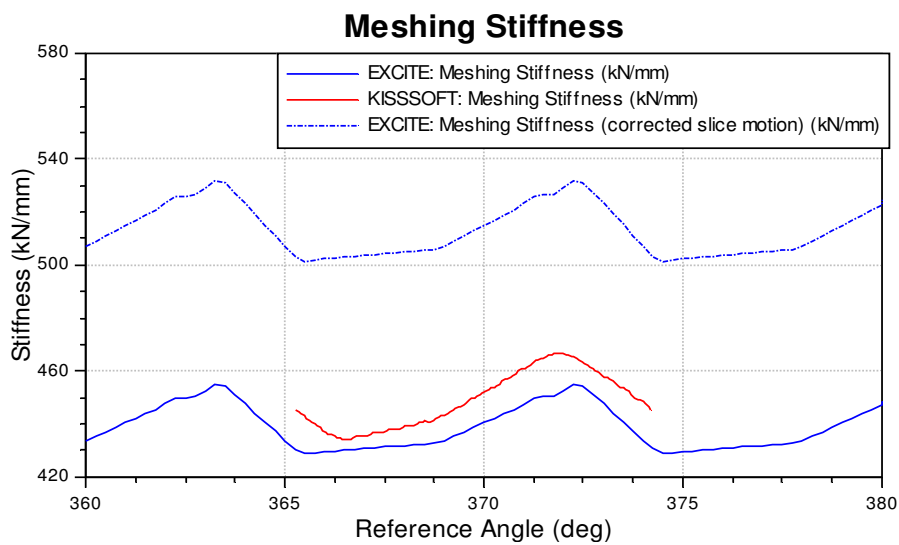


Figure 140: Model G - Meshing stiffness (computed with modified ACYG code)

Likewise the normal mesh deformation deviation improved (figure 141 and figure 142).

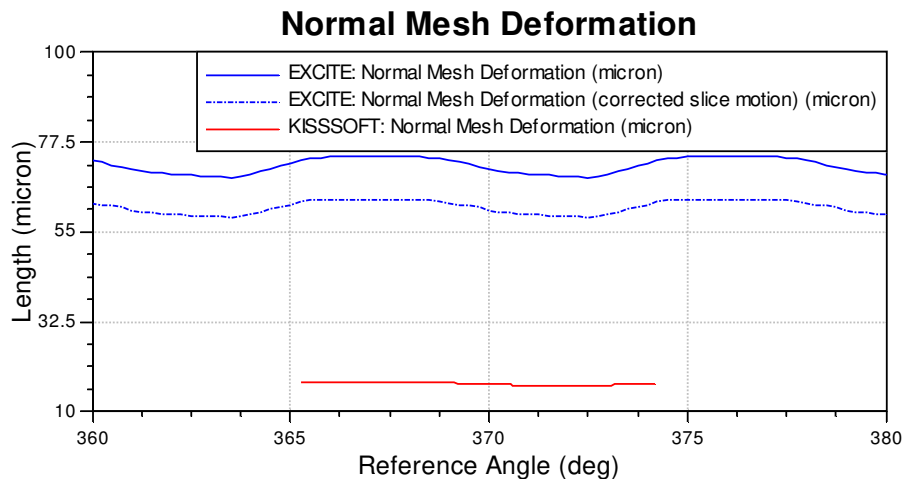


Figure 141: Model G - Normal mesh deformation

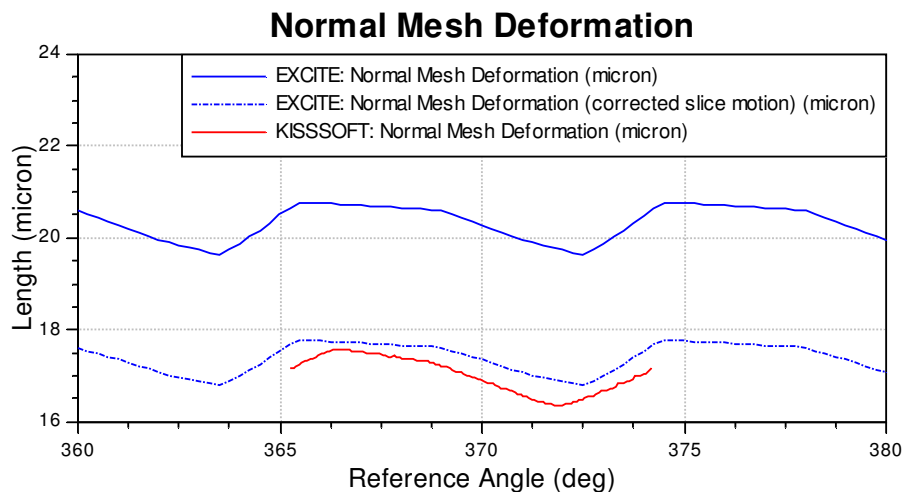


Figure 142: Model G - Normal mesh deformation (computed with modified ACYG code)

As already outlined, the normal force per unit length cannot be used to evaluate helical gears but nevertheless the results have become more similar.

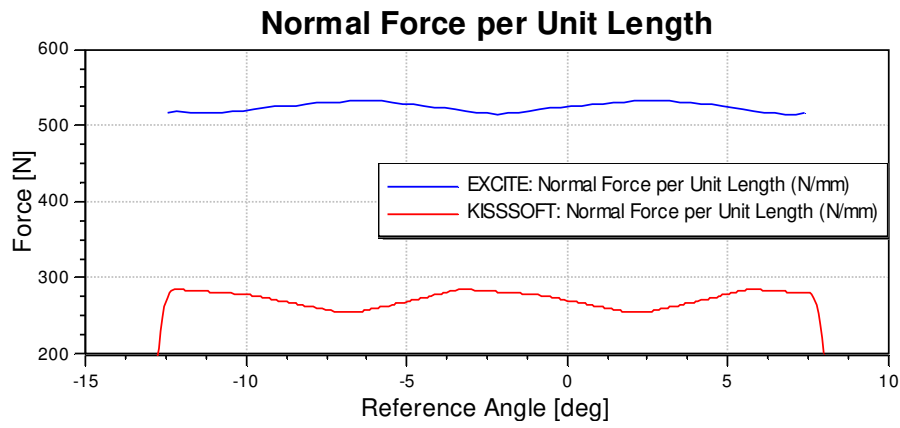


Figure 143: Model G - Normal force per unit length

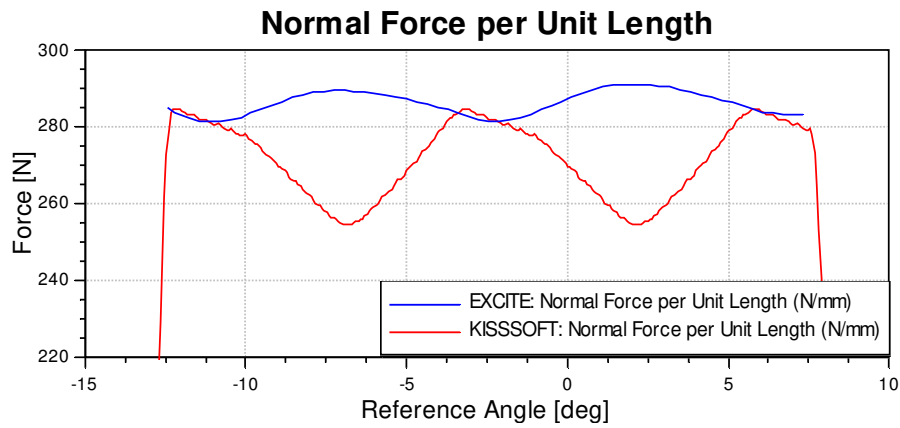


Figure 144: Model G - Normal force per unit length (computed with modified ACYG code)

After the ACYG source modification the engagement field is optically identical, as it can be seen in figure 146 and figure 147.

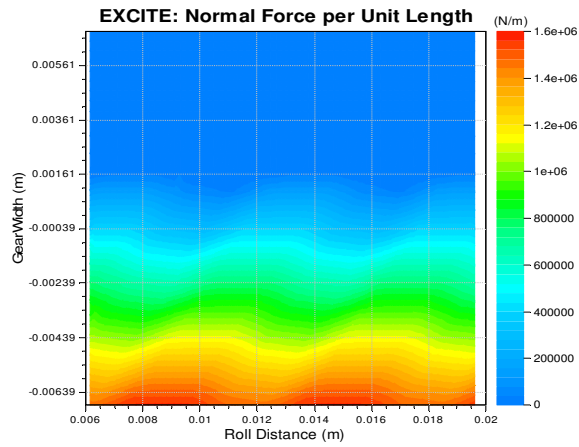


Figure 145: Model G - Engagement field plot from EXCITE (computed with modified ACYG code)

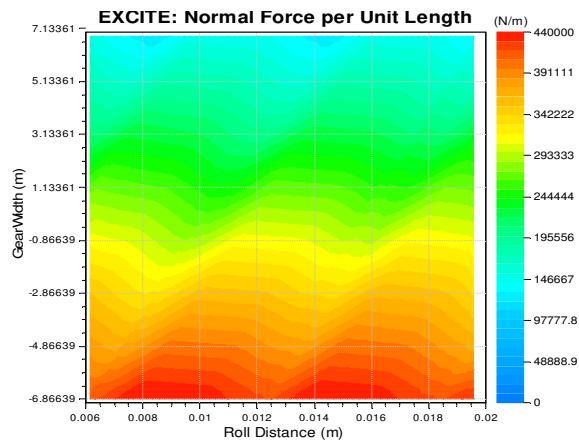


Figure 146: Model G - Engagement field plot from EXCITE (computed with modified ACYG code)

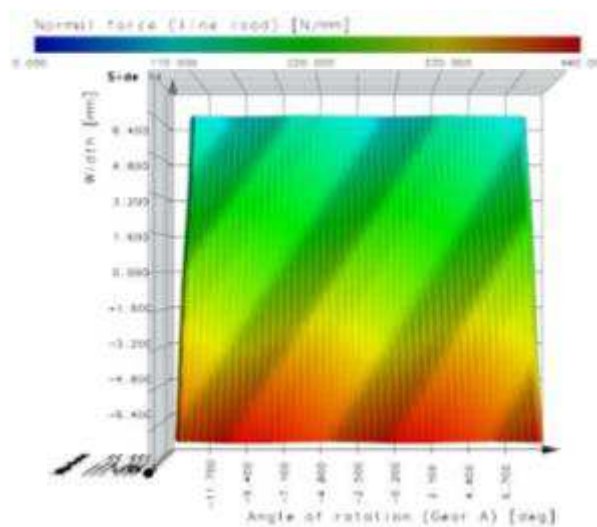


Figure 147: Model G - Engagement field plot from EXCITE Possible enhancements of the ACYG joint

### **8.3 Proposal of possible enhancements of the ACYG joint**

Based on the examinations performed within these, the following possible enhancements of the ACYG joint, which would increase the resolution of the gear contact further, are discussed.

#### *8.3.1 Modifying the existent ACYG source code*

Limitations of the ACYG joint, which are made to improve the performance of the source code, cause a limited resolution of the contact. In the next two points, possible modifications of the ACYG source code are outlined,

- Detection of contact out of the plane of action

Neglecting contacts arising out of the plane of action leads to deviations of the results, in particular during the transition of the number of flank pairs in action, as shown in chapter 7.7. Since the appearance of these contacts is depending on the load at the teeth, an additional non-linear effect would be added to the ACYG joint, which would increase the simulation time. Moreover, the detection of contact has to consider additional flank pairs in addition to those relevant for the plane of action, which would increase the simulation time further more.

- Approximation of involute in the stiffness approach according to Weber/Banaschek

Within the computation of the tooth bending according to Weber/Banaschek, the section modulus is computed by the integration of a quadratic approximation of the involute, as outlined in chapter 3.6.2. The results show that this quadratic approximation only delivers usable stiffness and deformation results if the base circle diameter fits to the root circle diameter, while the root area cannot be approximated reasonably (see Model J in chapter 7.6.10). In order to ensure a correct computation of these quantities the integration of the real geometry of the teeth, including the root area, is necessary.

This can be done by computing the section modulus at certain positions of force application points on the tooth with the real geometry, prior to the actual dynamic simulation. During the simulation the section modulus is then obtained by interpolating between the two adjacent values. This algorithm would deliver exact results of the section modulus and further, the simulation time would not be affected.

### *8.3.2 The use of empirical factors*

In comparison with the ACYG joint in EXCITE, KISSsoft uses additional empirical factors to compute the mating process between two gears, as outlined in chapter 5.3. Since the discretization into slices is similar between EXCITE and KISSsoft, it is possible to enable the use of these factors in the ACYG joint too. In the following, the feasibility of implementing and the impact on the simulation time of these factors are discussed.

- Slice linking factor

Especially for helical gears the slice linking factor plays an eminent role with regard to meshing stiffness and therefore on the computation of the forces. Generally, in EXCITE the equilibrium of the forces for example, is computed for each slice separately. Due to the linking of the slices, it would be necessary to compute the neighbouring slices again, what would increase the necessary number of iteration of the solver dramatically. Nevertheless, the force distribution over the gear width would be more accurate.

- Border weakening factor

The computation of the border weakening factor, as outlined in chapter 5.3.2, is only affected by the geometry of the neighbouring teeth and it has theoretically only to be calculated once at the beginning of the simulation. Therefore, the implementation of this empirical factor would not affect the simulation time and enable the simulation of tooth thickness at the edges of the gear width.

- Hertzian correction factor according to Winter/Podlesnik

Modifying the Hertzian contact according to Winter/Podlesnik [18], as it is implemented in KISSsoft, would affect the resulting Hertzian stiffness if the curvature of the involute is smaller than 1.01 times the normal module (outlined in chapter 5.3.3). The computation is only depending on the curvature of the involute and therefore it has only to be done once. As result the computed Hertzian contact stiffness would be more accurate without effecting the simulation time.

### *8.3.3 Alternative ways to compute the meshing stiffness*

The meshing stiffness computation according to Weber/Banaschek is till nowadays frequently used in common software tool as shown in chapter 4. In comparison to other pure analytical approaches it is the most accurate for outer gears and delivers an algorithm with a low computational expense [24]. Nevertheless, instead of computing the stiffness via analytical approaches, the accuracy can be improved by applying numerical or FE based methods. For instance, the shear over the gear width can be displayed. In the following alternate ways to compute the stiffness, respectively the deformation of a tooth, are proposed.

- Characterization of the meshing stiffness

The part which takes most of the simulation time during the computation of an ACYG joint is the calculation of the meshing stiffness, respectively the deformation. An opportunity to improve the performance is to precalculate the stiffness characterization of on tooth similar to the software tool STIRAK (see chapter 4.3). This stiffness characterization could be represented by an approximation curve or by a data grid which holds the stiffness result at certain operating points. Consequently, the stiffness of each flank pair can be computed during the simulation by the approximation curve or by interpolating between the relevant operation points. Furthermore, simulation time intensive approaches could be used, such as finite elements, to calculate the stiffness of the teeth.

- Using the kinetic energy to compute the meshing stiffness

The ACYG joint uses a simple penetration-force relation, as outlined in chapter 3.5. By assuming the tooth as clamped cantilever beam as in EXCITE, it is also possible to use the total elastic potential energy  $U$  to compute the meshing stiffness  $c$  as outlined in [25]. Equation 18 shows the relation between the potential energy  $U$  and the meshing stiffness  $c$ .

$$c = \frac{F^2}{U}$$

*Equation 18: Meshing stiffness computed by the kinetic energy  $U$  (source: [25])*

It is based on the assumption that the load distribution in the plane of action provides a minimum elastic potential energy. Therefore, the result is found by minimizing the total elastic potential energy  $U$ , which consists of the bending energy  $U_x$ , the compressive energy  $U_n$  and the shear elastic energy  $U_s$ :

$$U = U_x + U_n + U_s$$

*Equation 19: Total elastic potential energy (source: [25])*

Each part can be computed by equations of the theory of elasticity. Finally, the stiffness computation corresponds to the Timoshenko beam theory. Nevertheless, the elastic energy has to be computed for example with a 2D FE analysis. As result a quadratic approximation formula of the stiffness behaviour can be found which could be used in EXCITE. (See [26])

- The Rayleigh-Ritz approach to modelling bending and shear deflections of a gear teeth

The stiffness computation according to Weber/Banaschek does not consider shear of the teeth along the gear width, which plays especially in lightweight design, an essential role. A possibility to consider shear deformation is the Rayleigh-Ritz approach as outlined in [27]. It uses a tapered plate for modelling of the gear tooth as shown in figure 148.

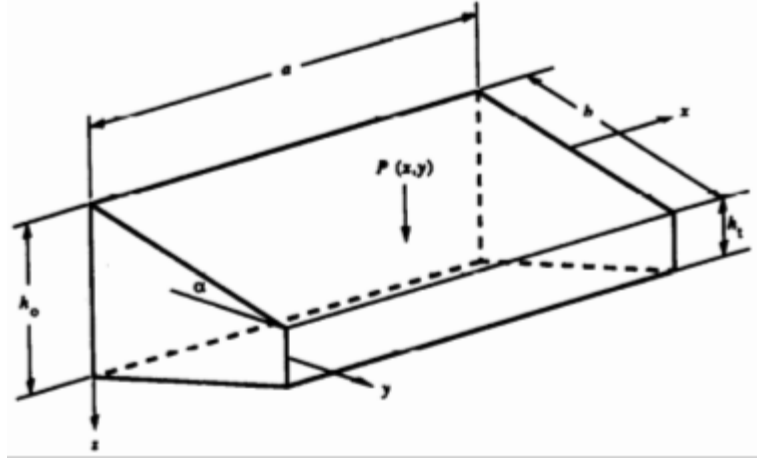


Figure 148: Shear tapered plate model with a concentrated load,  $P(x, y)$  (source: [27])

The idea is to determine the deflections of the tooth by minimizing the total strain energy of the model, which is given by

$$\begin{aligned}
 U = & \frac{D_0}{2} \iint \left( 1 - \frac{2y \tan(\alpha)}{h_0} \right)^3 \left\{ \left( \frac{\partial \psi_x}{\partial x} \right)^2 + 2r \left( \frac{\partial \psi_x}{\partial x} \right) \left( \frac{\partial \psi_y}{\partial y} \right) + \left( \frac{\partial \psi_y}{\partial y} \right)^2 \right. \\
 & \left. + \frac{1-r}{2} \left( \frac{\partial \psi_x}{\partial y} + \frac{\partial \psi_y}{\partial x} \right)^2 \right\} dx dy \\
 & + \frac{3D_0 K(1-r)}{h_0^2} \iint \left( 1 - \frac{2y \tan(\alpha)}{h_0} \right) \\
 & \times \left\{ \psi_x^2 + z \psi_x \frac{\partial \omega}{\partial x} + \left( \frac{\partial \omega}{\partial x} \right)^2 + \psi_y^2 + z \psi_y \frac{\partial \omega}{\partial y} + \left( \frac{\partial \omega}{\partial y} \right)^2 \right\} dx dy,
 \end{aligned}$$

Equation 20: Total strain energy (source: [27])

where  $D_0$  is the flexural rigidity of the plate at the supported edge,  $\omega$  the transverse displacement and  $\psi_x$  and  $\psi_y$  are the rotations about x and y axes.

Finally, the Gauss-Legendre technique is used to solve the integral and delivers a global stiffness matrix  $[S']_{total}$  of the tapered plate as outlined in Equation 21.

$$[S']_{local} = \begin{bmatrix} [S'_{11}]^{11} & [S'_{11}]^{12} & [S'_{11}]^{13} & \dots & [S'_{11}]^{mn} \\ [S'_{12}]^{11} & [S'_{12}]^{12} & [S'_{12}]^{13} & \dots & [S'_{12}]^{mn} \\ \vdots & & & & \\ [S'_{ij}]^{11} & [S'_{ij}]^{12} & [S'_{ij}]^{13} & \dots & [S'_{ij}]^{mn} \end{bmatrix}.$$

Equation 21: Global stiffness matrix of the tapered plate (source: [27])

The comparison with theoretical and experimental results, show reasonable conformity of the computed stiffness values by the Rayleigh-Ritz approach. Moreover, the differences between the Rayleigh-Ritz and a finite-element model results are negligible with a simultaneous shorter calculation time.

#### 8.3.4 Automated modification of the micro geometry

Currently in EXCITE, the profile and lead modification of the micro geometry have to be adjusted by user. Nevertheless, these modifications can be predicted by analytical methods from the results, like it is implemented in the software tool Romax (see chapter 4.4). For example, the helix angle correction  $f_{\beta}$  can be computed directly from the slope and skew misalignments using the equation 22.

$$f_{\beta} = Skew \cdot \cos(\alpha) + Slope \cdot \sin(\alpha)$$

Equation 22: Helix angle correction computation by skew and slope misalignments (source: [7])

Furthermore, the profile and lead modification can be manipulated in a way to lead to a specific behaviour of the gear mesh. For example, the noise and vibration are strongly depending on the stiffness behaviour of the gear mesh and therefore, on the modification of the micro geometry. The possibility to automatically optimizing the micro geometry of the gear mesh based on noise and vibration is outlined in [28].

## 8.4 Conclusion

The investigations conducted within this master thesis show that the contact model approach implemented for the Advanced Cylindrical Gear Joint (ACYG) in the multi-body dynamics software AVL EXCITE Power Unit deviates from results obtained by the tooth contact analysis software KISSsoft. The observed deviations are particularly with respect to slope-type angular misalignments. In order to ensure the correct representation of slope misalignments, geometrical verification (by analytical geometry relations as well as CAD) of the slice equivalent deformation and the position of contact points is carried out. Based on that findings a corrective computational algorithm is derived and implemented in the ACYG source code. The algorithm make sure that contact point locations computed under the idealized assumption of non-misaligned ideal involute flank shapes corrected based on the apparent slope misalignment. At the face load distribution, the results agree between EXCITE and KISSsoft with respect to spatial misalignments of the connected gears.

After applying the correction algorithm, all of the investigated spur gear reference models with a linear meshing stiffness conform to KISSsoft. The results of helical models differ about eight percent in the meshing stiffness and the normal mesh deformation result respectively. Recommendations to overcome this deviation are suggested for future research activities.

Neglecting contacts arising out of the plane of action (e.g. pre engagement due to tip circle contact) leads to divergent results, especially during the transition of the flank pairs in action. Nevertheless, the impact on the simulation time by consideration of these contacts is unknown and has to be investigated in order to assess a possible consideration of these effects.

The implemented stiffness, respectively deformation approaches applied in the ACYG joint as well as those of commercially established contact simulation tools are discussed and compared. The stiffness approach according to Weber/Banaschek is still used throughout many contact simulation tools and deliver feasible results. Moreover the method is computational more efficient as other analytical approaches or FE based methods. The applied computation of the Hertzian contact stiffness according to Petersen deliver similar results between EXCITE and KISSsoft.

Finally, based on the results of this theses, possible enhancements of the ACYG joint are proposed and alternative approaches to compute the meshing stiffness of the gear mesh are outlined.

## 9. LIST OF FIGURES

Figure 1: Engagement line model (GEAR/GGEA) (source:[5], chapter 4.16.2.4.)	5
Figure 2: 2D representation of the ACYG joint and the connected bodies in EXCITE (source [5], chapter 4.17.1)	6
Figure 3: The joint coordinate system of the ACYG joint (source: [5], chapter 4.17.1)	7
Figure 4: The discretization into slices of the ACYG joint (source:[3], chapter 2.2.5.3.)	9
Figure 5: Contact lines in the plane of action of a helical gear (source: [3], chapter 2.2.5.4.2.)	10
Figure 6: Internal description of the contact points via parameter $t_1$ and $t_2$ (sourc:[7])	11
Figure 7: Determination of the penetration area for a slice $i$ (source: [3], chapter 2.2.5.4.3.)	12
Figure 8: Deformation field (source: [3], chapter 2.2.5.4.3.)	13
Figure 9: Contact pressure distribution of a roller contact based on hydrodynamic, elastohydrodynamic and Hertzian theory (source: [6])	13
Figure 10: Petersen modified Hertz Penetration (source: [7])	15
Figure 11: Tooth bending according to Weber/Banaschek (source:[7])	16
Figure 12: Tooth tilting according to Weber/Banaschek (source:[7])	18
Figure 13: Stiffness model in RIKOR for four flank pairs and four slices (source: [11])	20
Figure 14: Discretization of the common gear width into slices in KISSsoft (source: [17], page 416)	24
Figure 15: Coupling of the slices in KISSsoft (source: [17])	26
Figure 16: Contact pattern of a helical gear mesh with applied slice coupling	27
Figure 17: Reduced tooth thickness of a helical gear (source: [17])	27
Figure 18: Contact pattern of a helical gear mesh with applied slice coupling	28
Figure 19: DiaFactor depeneding on the current diameter (source: [17])	29
Figure 20: Various possible errors which affect mesh mesh misalignments (source[19])	30
Figure 21: Gear fracture as result of angular misalignments (source [20])	31
Figure 22: Engagement field plot of a gear mesh without any misalignments	32
Figure 23: Profile deviations in the face cut (source: [6])	33
Figure 24: Flank line deviations (source: [6])	33
Figure 25: Run out error (source: [6])	34
Figure 26: Single pitch deviation (source: [6])	34
Figure 27: Total radial composite deviation (source: [6])	34
Figure 28: Engagement field plot of a gear mesh with a parallel misalignment	35
Figure 29: Definition of skew misalignment (source: [7])	36
Figure 30: Determination of skew misalignment (source: [7])	36
Figure 31: Engagement field plot of a gear mesh affected by skew misalignments	37
Figure 32: Definition of slope misalignment (source: [7])	38
Figure 33: Determination of slope misalignment (source: [7])	38
Figure 34: Engagement field plot of a gear mesh affected by slope misalignments	39
Figure 35: Possible modifications of the flank surface (source [6])	40

Figure 36: Pre- and disengagement impact (source: [23], page 98) .....	40
Figure 37: Tip relief (source: [5], chapter 4.17.5.4.1.).....	41
Figure 38: Root relief (source: [5], chapter 4.17.5.4.1.) .....	41
Figure 39: Srowning (Barreling) (source: [5], chapter 4.17.5.4.1.).....	42
Figure 40: Pressure angle correction (source: [5], chapter 4.17.5.4.1.) .....	42
Figure 41: End relief (source: [5], chapter 4.17.5.4.2.) .....	43
Figure 42: Crowning (source: [5], chapter 4.17.5.4.2.) .....	44
Figure 43: Helix angle correction (source: [5], chapter 4.17.5.4.2.).....	44
Figure 44: 3D representation of the reference model in EXCITE .....	45
Figure 45: 2D view of the reference model in EXCITE .....	46
Figure 46: Angular displacement of each gear .....	48
Figure 47: Simplified model.....	49
Figure 48: Gear data of the reference and the simplified model.....	49
Figure 49: Spur gear data of reference and simplified model.....	50
Figure 50: Positioning of the ACYG joint based on the global coordinate system .....	51
Figure 51: Point and direction of the measurement of meshing stiffness and deformation.....	52
Figure 52: Result quantity: Meshing stiffness .....	52
Figure 53: Result quantity: Normal mesh deformation.....	53
Figure 54: Result quantity: Normal force per unit length.....	54
Figure 55: Result quantity: Engagement field plot (3D) in KISSsoft .....	55
Figure 56: Result quantity: Engagement field plot (2D) in EXCITE .....	55
Figure 57: Result quantity: Engagement field plot (2D) in KISSsoft .....	55
Figure 58: Normal force per unit length ( $2.88 \cdot 10 - 2 \text{ kgm}^2$ ) .....	56
Figure 59: Normal force per unit length ( $2.88 \cdot 10 - 6 \text{ kgm}^2$ ).....	56
Figure 60: Model A - Meshing stiffness.....	59
Figure 61: Model A - Normal mesh deformation .....	59
Figure 62: Model A - Normal force per unit length .....	60
Figure 63: Model A - Engagement field plot from KISSsoft .....	60
Figure 64: Model A - Engagement field plot from EXCITE .....	60
Figure 65: Model B - Meshing stiffness.....	61
Figure 66: Model B - Normal mesh deformation .....	61
Figure 67: Model B - Normal force per unit length .....	62
Figure 68: Model B - Engagement field plot from KISSsoft .....	62
Figure 69: Model B - Engagement field plot from EXCITE .....	62
Figure 70: Model C - Meshing stiffness.....	63
Figure 71: Model C - Normal mesh deformation.....	63
Figure 72: Model C - Normal force per unit length.....	63
Figure 73: Model C - Engagement field plot from KISSsoft .....	64
Figure 74: : Model C - Engagement field plot from EXCITE .....	64
Figure 75: Model D - Meshing stiffness.....	65

<i>Figure 76: Model D - Normal mesh deformation</i> .....	65
<i>Figure 77: Model D - Normal force per unit length</i> .....	65
<i>Figure 78: Model D - Engagement field plot from KISSsoft</i> .....	66
<i>Figure 79: Model D - Engagement field plot from EXCITE</i> .....	66
<i>Figure 80: Model E - Meshing stiffness</i> .....	67
<i>Figure 81: Model E - Normal mesh deformation</i> .....	67
<i>Figure 82: Model E - Normal force per unit length</i> .....	67
<i>Figure 83: Model E - Engagement field plot from KISSsoft</i> .....	68
<i>Figure 84: Model E - Engagement field plot from EXCITE</i> .....	68
<i>Figure 85: Model F - Meshing stiffness</i> .....	69
<i>Figure 86: Model F - Normal mesh deformation</i> .....	69
<i>Figure 87: Model F - Normal force per unit length</i> .....	70
<i>Figure 88: Model F - Engagement field plot from KISSsoft</i> .....	70
<i>Figure 89: Model F - Engagement field plot from EXCITE</i> .....	70
<i>Figure 90: Model G - Meshing stiffness</i> .....	71
<i>Figure 91: Model G - Normal mesh deformation</i> .....	71
<i>Figure 92: Model G - Normal force per unit length</i> .....	71
<i>Figure 93: Model G - Engagement field plot from KISSsoft</i> .....	72
<i>Figure 94: : Model G - Engagement field plot from EXCITE</i> .....	72
<i>Figure 95: Model H - Meshing stiffness</i> .....	73
<i>Figure 96: Model H - Normal mesh deformation</i> .....	74
<i>Figure 97: Model H - Normal force per unit length</i> .....	74
<i>Figure 98: Model I - Engagement field plot from KISSsoft</i> .....	75
<i>Figure 99: Model H - Engagement field plot from EXCITE</i> .....	75
<i>Figure 100: Beam length in EXCITE and KISSsoft (source: [7])</i> .....	76
<i>Figure 101: Model I - Meshing stiffness</i> .....	77
<i>Figure 102: Model I - Normal mesh deformation</i> .....	77
<i>Figure 103: Model I - Normal force per unit length</i> .....	77
<i>Figure 104: Model I - Engagement field plot from KISSsoft</i> .....	78
<i>Figure 105: : Model I - Engagement field plot from EXCITE</i> .....	78
<i>Figure 106: Model J - Meshing stiffness</i> .....	79
<i>Figure 107: Model J - Normal mesh deformation</i> .....	79
<i>Figure 108: Model J - Normal force per unit length</i> .....	79
<i>Figure 109: Model J - Engagement field plot from KISSsoft</i> .....	80
<i>Figure 110: : Model J - Engagement field plot from EXCITE</i> .....	80
<i>Figure 111: Influence of the elastic mesh deformation on the path of contact</i> .....	81
<i>Figure 112: Impact of the variation of the torque on the EXCITE meshing stiffness</i> .....	82
<i>Figure 113: Impact of the variation of the torque on the KISSsoft meshing stiffness</i> .....	82
<i>Figure 114: Comparison of the impact of variation of the torque on the EXCITE and KISSsoft meshing stiffness</i> .....	83

<i>Figure 115: Comparison of the impact of variation of the torque on the EXCITE and KISSsoft normal mesh deformation</i> .....	83
<i>Figure 116: Comparison of the impact of variation of the torque on the EXCITE and KISSsoft normal force per unit length</i> .....	84
<i>Figure 117: Engagement field plot of a spur model (torque 250 Nm)</i> .....	85
<i>Figure 118: Engagement field plot of a spur model (torque 2.5 Nm)</i> .....	85
<i>Figure 119: Gear mesh of the simplified model</i> .....	86
<i>Figure 120: Hertz/Petersen contact stiffness of the simplified model</i> .....	87
<i>Figure 121: Gear mesh (ten teeth per gear)</i> .....	87
<i>Figure 122: Hertz/Petersen contact stiffness (ten teeth per gear)</i> .....	88
<i>Figure 123: Hertz/Petersen contact stiffness in detail (ten teeth per gear)</i> .....	88
<i>Figure 124: Gear mesh (100 teeth per gear)</i> .....	89
<i>Figure 125: Hertz/Petersen contact stiffness (100 teeth per gear)</i> .....	89
<i>Figure 126: Measurement plane for geometrical verification</i> .....	93
<i>Figure 127: Slice equivalent deformation</i> .....	94
<i>Figure 128: Geometrical overlap in CAD</i> .....	94
<i>Figure 129: Vertical offset of the contact points between the ACYG joint and CAD (micron)</i> ....	95
<i>Figure 130: Model D - Meshing Stiffness</i> .....	98
<i>Figure 131: Model D - Meshing stiffness (computed with modified ACYG code)</i> .....	98
<i>Figure 132: Model D - Normal mesh deformation</i> .....	99
<i>Figure 133: Model D - Normal mesh deformation (computed with modified ACYG code)</i> .....	99
<i>Figure 134: Model D - Normal force per unit length</i> .....	100
<i>Figure 135: Model D - Normal force per unit length (computed with modified ACYG code)</i> ....	100
<i>Figure 136: Model D - Engagement field plot from EXCITE</i> .....	101
<i>Figure 137: Model D - Engagement field plot from EXCITE (computed with modified ACYG code)</i> .....	101
<i>Figure 138: Model D - Engagement field plot from KISSsoft</i> .....	101
<i>Figure 139: Model D - Meshing stiffness</i> .....	102
<i>Figure 140: Model G - Meshing stiffness (computed with modified ACYG code)</i> .....	102
<i>Figure 141: Model G - Normal mesh deformation</i> .....	103
<i>Figure 142: Model G - Normal mesh deformation (computed with modified ACYG code)</i> .....	103
<i>Figure 143: Model G - Normal force per unit length</i> .....	104
<i>Figure 144: Model G - Normal force per unit length (computed with modified ACYG code)</i> ....	104
<i>Figure 145: Model G - Engagement field plot from EXCITE (computed with modified ACYG code)</i> .....	105
<i>Figure 146: Model G - Engagement field plot from EXCITE (computed with modified ACYG code)</i> .....	105
<i>Figure 147: Model G - Engagement field plot from EXCITE Possible enhancements of the ACYG joint</i> .....	105
<i>Figure 148: Shear tapered plate model with a concentrated load, <math>P(x, y)</math> (source: [27])</i> .....	110

## 10. LIST OF EQUATIONS

<i>Equation 1: Penetration area of the slice <math>i</math> (source: [3], chapter 2.2.5.4.3.)</i>	12
<i>Equation 2: Total penetration (source: [6])</i>	14
<i>Equation 3: Flank contact penetration by Petersen modified Hertz theory (source: [6])</i>	14
<i>Equation 4: Contact length of Hertz contact computed via ideal geometry (source: [6])</i>	15
<i>Equation 5: Contact length of Hertz contact (source: [6])</i>	15
<i>Equation 6: Bending of the tooth according to Weber/Banaschek (source: [6])</i>	16
<i>Equation 7: Tooth tilting according to Weber/Banaschek (source: [6])</i>	17
<i>Equation 8: Coupling stiffness as implemented in KISSsoft (source: [16])</i>	26
<i>Equation 9: Border weakening factor as implemented in KISSsoft (source: [16])</i>	27
<i>Equation 10: Smoothed curvature according to Winter/Podlesnik (source: [16])</i>	29
<i>Equation 11: Total skew amount determined from pinion and gear</i>	37
<i>Equation 12: Total slope amount determined from pinion and gear</i>	39
<i>Equation 13: Deflection of a cantilever beam</i>	73
<i>Equation 14: Slice contact point correction value</i>	96
<i>Equation 15: Involute creation angle <math>\alpha</math></i>	97
<i>Equation 16: Involute creation angle correction value</i>	97
<i>Equation 17: Parametrization of the involute creation angle correction value</i>	97
<i>Equation 18: Meshing stiffness computed by the kinetic energy <math>U</math> (source: [23])</i>	109
<i>Equation 19: Total elastic potential energy (source: [23])</i>	109
<i>Equation 20: Total strain energy (source: [25])</i>	110
<i>Equation 21: Global stiffness matrix of the tapered plate (source: [25])</i>	111
<i>Equation 22: Helix angle correction computation by skew and slope misalignments (source: [6])</i>	111

## 11. LIST OF REFERENCES

- [1] AVL List GmbH, EXCITE Power Unit, Graz, 2017.
- [2] KISSsoft AG, KISSsoft, Bubikon, 2017.
- [3] AVL List GmbH, EXCITE Power Unit Theory, Graz, 2017.
- [4] G. Ofner, Modelling of condensed flexible bodies considering non-linear inertia effects resulting from gross motions, Graz, 2011.
- [5] AVL List GmbH, EXCITE Power Unit Users Guide ACYG - Advanced Cylindrical Gear Joint, Graz, 2017.
- [6] B. Schlecht, Maschinenelemente Band II, Pearson, 2010.
- [7] AVL List GmbH, EXCITE Power Unit ACYG Internal Documentation, Graz, 2017.
- [8] D. Petersen, Auswirkung der Lastverteilung auf die Zahnfußstragfähigkeit von hochüberdeckenden Stirnradpaarungen, Fakultät Maschinenbau TU-Braunschweig, 1989.
- [9] C. Weber and K. Banaschek, Elastische Formänderung der Zähne und der anschließenden Teile der Radkörper von Zahnradgetrieben, FVA Bericht 129 und 134, FVA 1955.
- [10] Vexlex and P. Sainsot, Contribution of Gear Body to Tooth Deflections - A New Bi-dimensional Analytical Formula, Journal of Mechanical Design, Vol. 126, 2004.
- [11] B. Mahr, Comparison between different commercial gear tooth contact analysis software packages, KISSsoft AG, 2014.
- [12] M. Zeyed Sfar, Bestimmung von Verzahnungskorrekturen und Lagerkräften in Planetengetrieben für Lastkollektive, Schriftenreihe Heft 11.7 .

- [13] B. Schlecht and T. Schulze ,Design and optimization of planetary gears under consideration of all relevant influences, Dresden, 2010.
- [14] FVA GmbH, FVA Gear Designer, 2017.
- [15] FVA GmbH, Information zur FVA-Workbench Version 3.7, Frankfurt am Main, 2017.
- [16] Romax Technology Centre, University of Nottingham Innovation Park. Transmission Magazine Issue 3, Nottingham, 2017.
- [17] KISSsoft AG, KISSsoft User Manual Release 03/2017, 2017.
- [18] H. Winter and B. Podlesnik, Zahnfedersteifigkeit von Stirnradgetrieben Parts 1 to 3, Antriebstechnik 22, 1983.
- [19] H. Linke, Stirnradverzahnung, München, Hanser-Verlag, 2010.
- [20]. Neale Consulting Engineers, 2016,  
<http://www.tribology.co.uk/services/failure-analysis/how-to-diagnose-gear-failures/> [Cited: 04 09 2017].
- [21] Hanjun Jiang and Yimin Shao, The influence of mesh misalignment on the dynamic characteristics of helical gears including sliding friction, Canada, Springer Verlag, 2015.
- [22] Houser and R. Donald, Gear Mesh Misalign, 2006.
- [23] G. Niemann and H. Winter, Maschinenelemente Band II, Berlin, Springer-Verlag, 1989.
- [24] C. Spura, Berechnung der Verformungen und Steifigkeiten evolventischer Verzahnungen von Zahnkupplungen, 2015.
- [25] J.I. Pedrero, M. Pleguezuelos, M. Artés, J.A. Antona, Load distribution model along the line of contact for involute external gears, Eslevier publisher, 2010.

- [26] N. Pedersen and, M. Jørgensen, On gear tooth stiffness evaluation, Elsevier publisher, 2014.
- [27] E. YAU, H. BUSBYI, D. HOUSER, A Rayleigh-Ritz approach to modelling bending and shear deflections of gear teeth, Elsevier publishee, 1994.
- [28] S. Ghosh and G. Chakraborty, On optimal tooth profile modification for reduction of vibration and noise in spur gear pairs, Elsevier publisher, 2016.
- [29] LeCain and Nicholas, Tutorial of Hertzian Contact Stress Analysis, 2011.